

2010

## Building and testing a high spatial resolution nulling microellipsometer using rotational polarization symmetry

Alain Ngoy Tschimwang  
*University of Dayton*

Follow this and additional works at: [https://ecommons.udayton.edu/graduate\\_theses](https://ecommons.udayton.edu/graduate_theses)

---

### Recommended Citation

Tschimwang, Alain Ngoy, "Building and testing a high spatial resolution nulling microellipsometer using rotational polarization symmetry" (2010). *Graduate Theses and Dissertations*. 6041.  
[https://ecommons.udayton.edu/graduate\\_theses/6041](https://ecommons.udayton.edu/graduate_theses/6041)

This Dissertation is brought to you for free and open access by the Theses and Dissertations at eCommons. It has been accepted for inclusion in Graduate Theses and Dissertations by an authorized administrator of eCommons. For more information, please contact [mschlange1@udayton.edu](mailto:mschlange1@udayton.edu), [ecommons@udayton.edu](mailto:ecommons@udayton.edu).

**BUILDING AND TESTING A HIGH SPATIAL RESOLUTION NULLING  
MICROELLIPSOMETER USING ROTATIONAL POLARIZATION  
SYMMETRY**

Dissertation

Submitted to

The School of Engineering of the

UNIVERSITY OF DAYTON

In Partial Fulfillment of the Requirements for

The Degree of

Doctor of Philosophy in Electro-optics

By

Alain N. Tschimwang, M.S.

UNIVERSITY OF DAYTON

Dayton, Ohio

May, 2010

*Original*

**BUILDING AND TESTING A HIGH SPATIAL RESOLUTION NULLING  
MICROELLIPSOMETER USING ROTATIONAL POLARIZATION  
SYMMETRY**

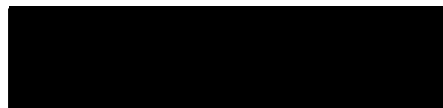
APPROVED BY:



Qiwen Zhan, Ph.D.

Advisory Committee Chairman

Associate Professor, Electro-optics  
and Electrical Engineering



Joseph Haus, Ph.D.

Electro-optics Department Chair

Professor, Electro-optics



John Loomis, Ph.D.

Committee Member

Professor, Electro-optics and  
Electrical Engineering



Andrew Ewvaraye, Ph.D.

Committee Member

Professor, Physics



Malcolm W. Daniels, Ph.D.

Associate Dean

School of Engineering



Tony E. Saliba, Ph.D.

Dean, School of Engineering

## **ABSTRACT**

### **BUILDING AND TESTING A HIGH SPATIAL RESOLUTION NULLING MICROELLIPSOMETER USING ROTATIONAL POLARIZATION SYMMETRY**

Name: Tschimwang, Alain Ngoy

University of Dayton

Advisor: Dr. Qiwen Zhan

Ellipsometry is a powerful optical metrology technique that uses light's amplitude and phase changes that occur on reflection in order to measure several properties of a thin film sample such as thickness, roughness, refractive index, etc., in a non-destructive way. Current ellipsometers capabilities have spatial resolution and signal-to-noise ratio (SNR) limitations. The size of microstructure-based devices is rapidly shrinking (according to Moore's law) and their characterization becomes a big challenge as far as ellipsometry is concerned. The limitation in spatial resolution is a major obstacle in current generation ellipsometers, in addition to the low pixel-size-dependent SNR performance.

In this research, I present the design, implementation, and testing of a high spatial resolution nulling microellipsometer. In order to improve the SNR while still maintaining high ellipsometric sensitivity and high spatial resolution, the microellipsometer has been designed based on the principle of rotational polarization symmetry. A rotationally symmetric polarization signal is achieved using the combination of a circularly polarized

uniform illumination, a polarization rotator, and a radial analyzer. An annular aperture is used to perform back focal plane spatial filtering by selecting the signal generated from a narrow annular cone of illumination for high ellipsometric sensitivity. The SNR is improved by collecting high angle ellipsometric signals within an entire annular region in the back focal plane, instead of a single azimuthal position. The combination of high numerical aperture ( $NA = 0.9$ ) focusing and back focal plane polarization analysis yields a high spatial resolution of  $0.48\text{ }\mu\text{m}$  at  $632.8\text{ nm}$  and an increased accuracy for performing spatially resolved ellipsometric measurements.

The instrument has been tested on several flat (uniform thickness) Silicon-dioxide ( $\text{SiO}_2$ ) thin film samples deposited on Silicon (Si) substrates, and the measured thickness and refractive indices values are in close agreement with the measurements taken using a commercial spectroscopic ellipsometer. The thickness profile of a sample, consisting of a photoresist microprism fabricated on a Silicon substrate, has been measured to test the profiling capability of our microellipsometer. The measured thickness profiles, compared to the profile measurement taken with an atomic force microscope (AFM), have shown close agreement, repeatability, and accuracy.

To my dear family in the Democratic Republic of Congo: my father, the Rev. pastor Bruno Tschimwang Muzangish, my mother, Angelique Ngoy wa Ngombe, and my beloved brothers Guy, Didier, Enock, Paul de Tarse, Simon, Ezekiel and my sisters, Bienvenue, Naomie, Ruth, Charlotte, and my dearest Kabey Norris ; to you all, in the name of Jesus Christ our Lord and Savior, I dedicate this work.

## **ACKNOWLEDGEMENTS**

First, glory be to you, Jesus Christ, my Lord and Savior for the innumerable blessings and for your protection and guidance during the period of this academic endeavor. Also, I would like to thank my family for their unconditional love and support during my graduate studies.

I would like to thank Dr. Qiwen Zhan, my advisor and mentor, for his unyielding support, help, and guidance he provided inside and outside the laboratory. You are an inspiration to me.

This work would not have been possible without Dr. Joseph Haus' help. I cannot thank you enough for providing the necessary financial and academic support that made this work possible. In this regard, I also would like to thank Drs. John Loomis and Andrew Ewwaraye, all members of my dissertation committee, for their advice and suggestions.

Finally, I would like to thank all the institutions that supported, directly or indirectly, through various forms of financial support: Applied Materials, Inc., University of Dayton graduate school, DAGSI (Dayton Area Graduate Studies Institute).

## TABLE OF CONTENTS

ABSTRACT .....	iii
DEDICATION .....	v
ACKNOWLEDGMENTS .....	vi
LIST OF FIGURES .....	x
LIST OF TABLES .....	xv
I. INTRODUCTION .....	1
A. The Basics of Reflection and Transmission of Polarized Light .....	1
B. Ellipsometric Definitions .....	8
C. Representation of Polarization by Ellipsometric Angles .....	10
D. Fitting Models to Data .....	15
D1. Figures of Merit .....	17
D2. Convergence Routines .....	18
II. THE BASIC FOUNDATIONS OF ELLIPSOMETRY .....	24



A. Brief History of Ellipsometry .....	24
B. Basic Optical Elements Used in Ellipsometry .....	25
C. Common Ellipsometer Configurations .....	27
C1. Nulling Ellipsometer: PCSA Configuration .....	28
C2. Rotating Elements Ellipsometer .....	30
C3. A Nulling Ellipsometer with PSRA Configuration .....	33
D. Photometric Ellipsometry .....	35
III. NEW SOLUTIONS TO NEW CHALLENGES IN ELLIPSOMETRY .....	38
IV. DESIGNING AND TESTING A HIGH SPATIAL RESOLUTION NULLING MICROELLIPSOMETER .....	45
A. Design Principles .....	45
B. Mathematical Derivation of the Signal and the Nulling Detection Scheme .....	51
C. Instrumentation .....	57
C1. Circular Polarization Generation .....	60
C2. Polarization Rotator Alignment and Calibration .....	61
D. Signal Testing .....	64
V. EXPERIMENTAL MEASUREMENTS .....	68

A. Results .....	68
B. Remarks .....	78
VI. CHARACTERIZATION OF ISOLATE SUBWAVELENGTH LINE STRUCTURES USING POLARIZATION AND PHASE SIGNATURES .....	80
A. Introduction .....	80
B. Focal Fields .....	81
C. Reflected Fields in Conical Diffraction Mounting .....	84
D. Numerical Simulation Results .....	90
VII. CONCLUSIONS .....	104
VIII. APPENDIX .....	107
IX. BIBLIOGRAPHY .....	109

## LIST OF FIGURES

1. Reflection and transmission of a plane wave at a planar interface .....	2
2. Reflections at multiple interfaces: ambient-film-substrate system .....	7
3. Real and imaginary parts of the amplitude reflection coefficients for s- and p-polarizations .....	7
4. Characterization of the ellipse of polarization .....	10
5. Psi and Del values for 63° incidence angle and film thickness values from 0 – 290 nm .....	14
6. Execution flow diagram of the Levenberg-Marquardt algorithm .....	21
7. A conceptual nulling ellipsometer arrangement: The PCSA configuration .....	28
8. A conceptual nulling arrangement with the QWP inserted before the sample .....	30
9. Intensity vs. polarizer's angle near the null .....	30
10. A rotating polarizer null ellipsometer arrangement .....	31
11. Rotating null ellipsometer (figure published in ref. 15) .....	32
12. The Monin-Boutry Ellipsometer (PSRA configuration) .....	34

13. (a) Ray picture of reflections in normal illumination configuration. (b) Polarizations of reflected rays in the back focal plane (reproduced from ref. 29) .....	40
14. Simplified diagram of the ellipsometer for signal derivation (reproduced from reference 29) .....	41
15. Experimental setup of the ellipsometer (reproduced from ref. 29) .....	43
16. (a) A conventional ellipsometer. (b) A single ray forms a single channel, equivalent to a conventional ellipsometer, by inserting a high NA lens in the path of the ray in (a). (c) Top view of the aperture plan showing a single channel, and multiple channels after replication .....	46
17. Conceptual diagram of radially symmetric microellipsometer design .....	47
18. Diagram of the polarization rotator (PR) .....	49
19. Coordinate system in the back focal plane of the objective .....	52
20. Simulation of the dc signal amplitude vs. bias voltage-induced retardation phase under different polarizations .....	55
21. First harmonic signal for (a) a circularly polarized beam, (b) a quasi-circularly polarized beam .....	56
First harmonic signal for (c) a linearly polarized beam, (d) an elliptically polarized beam .....	56
22. Complete laboratory setup of the microellipsometer .....	58

23. Alignment diagram for circular polarization generation .....	60
24. Polarization rotator alignment and calibration diagram .....	62
25. Polarization rotator calibration curve for a bias range of $\pm 700$ volts .....	63
26. (top) ac modulation voltage signal (1 KHz), (bottom) detected second harmonic signal (2 KHz) under linear polarization illumination .....	64
27. Detected first harmonic (1 KHz, top) and second harmonic (2 KHz, bottom) signals under circular polarization illumination .....	65
28. First harmonic signal (a) and dc signal (b) vs. dc bias voltage .....	66
29. Spatial evolution of minima in the first harmonic signal for testing signal stability and validity before any measurements are taken. (b) Repeatability test .....	69
30. Fitting results for (a) $\Psi$ and (b) $\Delta$ .....	70
31. Fitting result: experimental and analytical rotation voltages for 5 SiO <sub>2</sub> /Si samples .....	72
32. Refractive indices measurements of SiO <sub>2</sub> samples .....	72
33. AFM scan of micro prisms that form the grating sample .....	74
34. Rotation voltage fitting result (a), with the second measurement as repeatability test. The corresponding thickness profile is shown in (b) .....	75
35. dc (a) and first harmonic (b) signals resulting from the first of the two 13 $\mu$ m long scans of the micro prism .....	76

36. Fitting of micro prism experimental data to micro prism optical model: $\psi$ (a) and $\Delta$ (b) .....	77
37. Microellipsometer thickness profile measurements compared to the AFM profile measurement .....	78
38. Focusing of a linearly polarized beam .....	81
39. Intensities of field components in the focal plane: x-component (a), y-component (b), z-component (c), total intensity (d) .....	83
40. Geometry for the conical diffraction mounting (figure from ref. 53) .....	84
41. Schematic of a high NA objective lens as an aplanatic system consisting of an entrance and an exit pupil .....	85
42. k-space grid model used in the calculation of the diffracted fields in the exit pupil plane .....	86
43. Mirror symmetry between incident and reflected p-polarizations in the plane of incidence .....	88
44. Coherent addition of diffracted fields on the grid .....	90
45. Pupil plane intensity distributions (a) and (c), and phases (b) and (d) from reflected x- and y- field amplitudes, respectively .....	92
46. An isolated ridge with vertical sidewalls .....	94

47. Diffracted field's x- component intensities ((a) and (b)) and phases ((c) and (d)). (b) and (d) are zoomed views showing the separation of curves in (a) and (c), respectively. (e) is the phase of the diffracted field's y-component and (f) is the zoomed view of (e) ..... 95
48. An isolated subwavelength line with negative (a) and positive (b) side wall angles ..... 98
49. x-component's intensities (a) and phases (b) for and isolated line with varying side wall angles. Fig. 49(c) shows a zoomed view of Fig. 49(b). Figs. 49(d) and 49(e) show the y-component's phases and the zoomed view, respectively. Fig. 49(f) shows a side-by-side comparison of phase change with respect to the side wall angle at the ( $k_x=3.2 \mu\text{m}^{-1}$ ,  $k_y=0 \mu\text{m}^{-1}$ ) location in the pupil plane ..... 98

## LIST OF TABLES

1. Thicknesses and refractive indices (at  $\lambda=6333$  nm) of five SiO<sub>2</sub>/Si samples measured with a spectroscopic ellipsometer (Angstrom PHE 102) ..... 70
2. Phase differences between consecutive phase curves shown in Figs. 49(b) and 49(d), corresponding to both x- and y- field components ..... 102



## CHAPTER I

### INTRODUCTION

#### A. The Basics of Reflection and Transmission of Polarized Light

Polarization is one of the most important properties of light. When light propagates in a medium it induces a vibration motion of the electric charges of electrons and nuclei, generating macroscopic electric currents. This vibration is effected mostly in the direction of vibration of the electric field component of the wave, the magnetic moments of electrons and nuclei being too slow to follow the incident field's oscillations. Thus, the most important quantity describing the light wave is the vector of its electric field,  $\vec{E}$ . When a wave propagates in a medium the electric field has some preferential directions in which it exerts an action on the electric charges in the matter, and these preferential directions are directly tied to polarization.<sup>1</sup> The spatial and temporal dependence of the electric field  $\vec{E}(r,t)$  in a uniform, isotropic medium with complex permittivity  $\epsilon$ , is described by the wave equation<sup>1</sup>

$$\nabla^2 - \frac{1}{c^2} \frac{\partial^2}{\partial t^2} = 0, \quad (1a)$$

where

$$\bar{D} = \int \epsilon(t-t') \bar{E}(t') dt', \quad (1b)$$

$\omega$  the angular frequency of the light wave, and  $c$  the speed of light in vacuum. Solutions to the wave equation in the reflection and transmission cases (see Fig. 1) are monochromatic plane waves propagating along the x- and the z- axes of an orthogonal coordinate system, and are of the form,

$$\vec{E}(r, t) = \vec{E} \exp[j(k_x x + k_z z - \omega t)] \quad (2)$$

Here  $k_x$  and  $k_z$  are the propagation vectors in the x- and z- directions, respectively, since the plan of incidence lies in the x-z plan ( $k_y = 0$ ) as shown in Fig.1. The plane waves of Eq. (2) solve the wave equation for

$$k_x^2 + k_z^2 = \frac{\omega^2}{c^2} \epsilon(\omega). \quad (3)$$

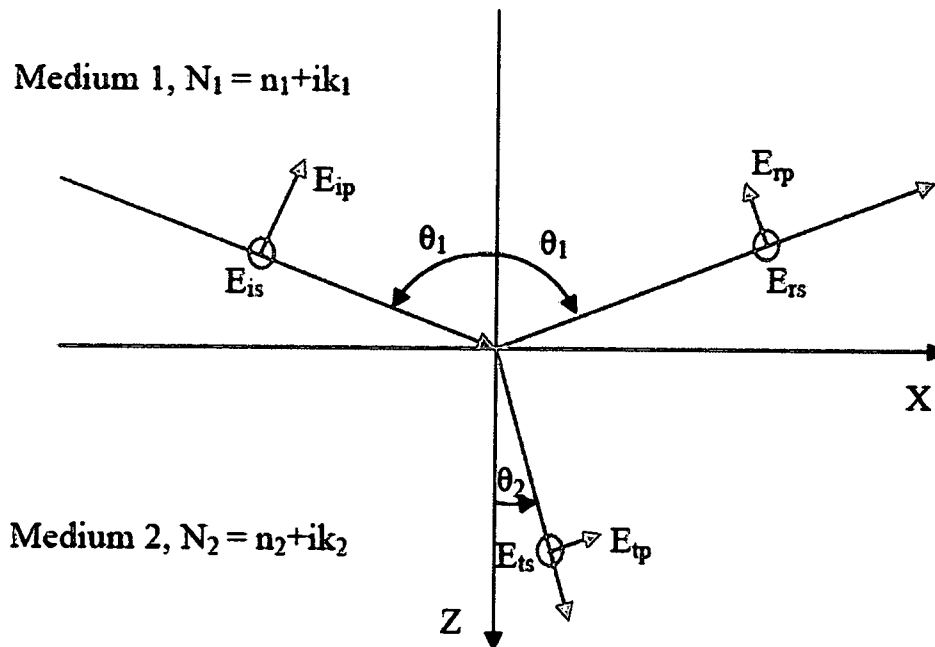


Fig. 1: Reflection and transmission of a plane wave at a planar interface.

The total field in medium 1 is the superposition of the incident and the reflected plane waves

$$\begin{aligned}\vec{E}_i(r, t) &= \vec{E}_i \exp[j(k_{xi}x + k_{zi}z - \omega t)] \\ \vec{E}_r(r, t) &= \vec{E}_r \exp[j(k_{xr}x + k_{zr}z - \omega t)] \quad z < 0,\end{aligned}\tag{4}$$

and the transmitted wave in medium 2 is

$$\vec{E}_t(r, t) = \vec{E}_t \exp[j(k_{xt}x + k_{zt}z - \omega t)] \quad z > 0.\tag{5}$$

The propagation vectors in the x- and z- directions are defined as

$$k_{xi} = \frac{\omega}{c} N_1 \sin \theta_1, \quad k_{zi} = \frac{\omega}{c} N_1 \cos \theta_1.\tag{6}$$

Here, it is important to note that  $\sin \theta$  and  $\cos \theta$  can be complex, although still satisfying  $\sin^2 \theta + \cos^2 \theta = 1$  as required by Eq. (3). For the plane waves propagating with a wave vector  $\vec{k}$ , the tangential (i.e., X – Y) components of  $\vec{E}$  and  $\vec{H}$  at the interface are related by  $\vec{H} = (\vec{k} \times \vec{E})/(\omega\mu_0)$ ,  $\vec{E} = -(\vec{k} \times \vec{H})/(\omega\epsilon\epsilon_0)$ . The Cartesian components are found to be

$$H_x = -\frac{k_z E_y}{\omega\mu_0}, \quad H_y = \frac{-k_x E_z + k_z E_x}{\omega\mu_0}, \quad H_z = \frac{k_x E_y}{\omega\mu_0},\tag{7}$$

$$E_x = \frac{k_z H_y}{\omega_0}, \quad E_y = \frac{k_z H_x - k_x E_z}{\omega_0}, \quad H_z = -\frac{k_x H_y}{\omega_0},\tag{8}$$

since  $k_y = 0$ . For the waves that are linearly polarized perpendicular to the plane of incident (i.e.,  $E_x = E_y = 0$ ), there are three nonvanishing field components,  $E_x$ ,  $H_x$ , and

$H_z$ . This case is called s-polarization, from the German word *Senkrecht*, meaning perpendicular. When the plane waves are polarized parallel to the plane of incident, i.e.,  $E_y = 0$ , the only nonvanishing components are  $E_x$ ,  $E_z$ ,  $H_y$ . This case is called p-polarization. The superposition of s- and p- polarizations gives a general case of polarization.

Ellipsometry is mostly interested in the polarization change that occurs on reflection and transmission of the plane waves in Eqs. (4) and (5). The reflection coefficients are the ratios of the amplitudes of the reflected and the incident waves. The transmission coefficients are the ratios of the amplitudes of the transmitted and the incident waves. Let us denote by  $E_{is}$ ,  $E_{rs}$ , and  $E_{ts}$  the amplitudes of the incident, reflected, and transmitted waves, respectively. They represent the Y- components of the vectors  $\vec{E}_i$ ,  $\vec{E}_r$ ,  $\vec{E}_t$  of Eqs. (4) and (5). The continuity of fields at the interface ( $Z=0$ ) requires that

$$E_{is} + E_{rs} = E_{ts}. \quad (9)$$

From Eqs. (7), the tangential (X) component of the magnetic field intensity vector of the incident wave has the amplitude  $k_{zi}E_{is}/(\omega\mu_0)$ . Similarly, the amplitudes of the X components of the reflected and the transmitted waves are  $k_{zr}E_{rs}/(\omega\mu_0)$  and  $k_{zt}E_{it}/(\omega\mu_0)$ , respectively. Using the fact that

$$\begin{aligned} k_{xi} &= k_{xr} = k_{zt}, \\ k_{xr} &= \frac{\omega}{c} N_1 \sin \theta_1, \quad k_{zr} = \frac{\omega}{c} N_1 \cos \theta_1, \\ k_{xt} &= \frac{\omega}{c} N_2 \sin \theta_2, \quad k_{zt} = \frac{\omega}{c} N_2 \cos \theta_2, \end{aligned} \quad (10)$$

the condition of matching the tangential components of the magnetic field strength at the interface  $Z=0$  can be expressed in terms of the electric field strengths as<sup>1</sup>

$$N_1 \cos \theta_1 (E_{is} - E_{rs}) = N_2 \cos \theta_2 E_{ts}. \quad (11)$$

Combining Eqs. (9), (10), and (11) leads to the resulting Fresnel reflection and transmission coefficients, which are given by<sup>1</sup>

$$\begin{aligned} r_s &= \frac{N_1 \cos \theta_1 - N_2 \cos \theta_2}{N_1 \cos \theta_1 + N_2 \cos \theta_2}, \\ t_s &= \frac{2N_1 \cos \theta_1}{N_1 \cos \theta_1 + N_2 \cos \theta_2}. \end{aligned} \quad (12)$$

A similar mathematical operation can be carried out to find the Fresnel coefficients for the p-polarization, which are given by<sup>1</sup>

$$\begin{aligned} r_p &= \frac{N_1 \cos \theta_2 - N_2 \cos \theta_1}{N_1 \cos \theta_2 + N_2 \cos \theta_1}, \\ t_p &= \frac{2N_1 \cos \theta_2}{N_1 \cos \theta_2 + N_2 \cos \theta_1}. \end{aligned} \quad (13)$$

Note that at normal incidence (i.e.  $\theta_1 = 0$ ) the reflection and transmission coefficients for both s- and p- polarizations becomes equal and are given by<sup>1</sup>

$$\begin{aligned} r_s = r_p &= \frac{N_1 - N_2}{N_1 + N_2}, \\ t_s = t_p &= \frac{2N_1}{N_1 + N_2}. \end{aligned} \quad (14)$$

In the case of a single interface as shown in Fig. 1, the Fresnel coefficients are real. When there is more than one interface these coefficients are generally complex. For the

case of a thin film deposited on a substrate (see Fig. 2), as it may be the case in ellipsometry, there are two interfaces. The first interface is between the ambient medium and the film, and the second interface is between the film and the substrate. It is obvious that this case involves multiple reflections and transmissions generated at both interfaces. To calculate the Fresnel coefficient of such as system one needs to treat one interface at a time as explained above, and combine them to find the total reflection and transmission coefficients. The Fresnel reflection coefficients for the s- and p- polarization at the first (air-film or  $af$ ) and second (film-substrate or  $fs$ ) interfaces for a film-substrate system in air are given by<sup>2</sup>

$$r_{af}^s = \frac{N_a \cos \theta_f - N_a \cos \theta_f}{N_a \cos \theta_f + N_a \cos \theta_f}, r_{af}^p = \frac{N_f \cos \theta_a - N_a \cos \theta_f}{N_f \cos \theta_a + N_a \cos \theta_f}, \quad (15)$$

$$r_{fs}^s = \frac{N_f \cos \theta_s - N_f \cos \theta_s}{N_f \cos \theta_s + N_f \cos \theta_s}, r_{fs}^p = \frac{N_s \cos \theta_f - N_f \cos \theta_s}{N_s \cos \theta_f + N_f \cos \theta_s}, \quad (16)$$

respectively. The total reflection for the entire system is given by<sup>2</sup>

$$r_s = \frac{r_{af}^s + r_{fs}^s \exp(-j2\beta)}{1 + r_{af}^s r_{fs}^s \exp(-j2\beta)}, r_p = \frac{r_{af}^p + r_{fs}^p \exp(-j2\beta)}{1 + r_{af}^p r_{fs}^p \exp(-j2\beta)}, \quad (17)$$

where  $\beta$  is the total accumulated phase defined as

$$\beta = 2\pi \frac{d}{\lambda_0} n_2 \cos \theta_f. \quad (18)$$

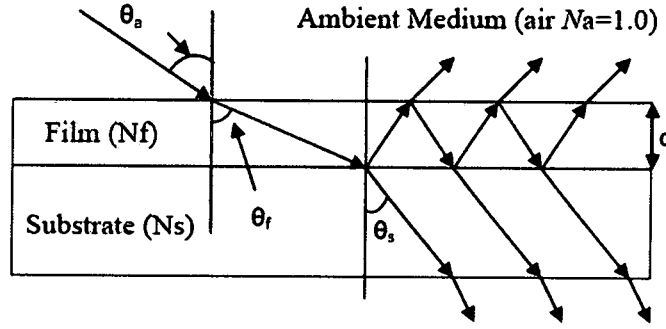


Fig. 2: Reflections at multiple interfaces: ambient-film-substrate system.

The amplitude and power reflection coefficients with their associated phases are shown in Fig. 3, for both s- and p- polarizations, as functions of the incident angle. Note that the p-polarization reflectivity goes to zero at the Brewster's angle where only the s-polarization

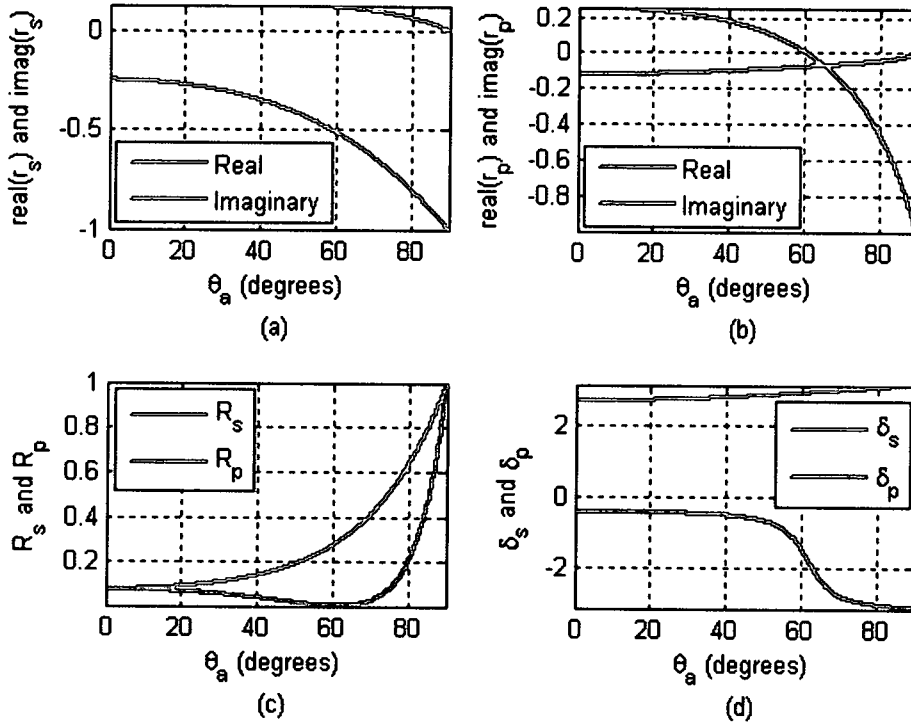


Fig. 3: Real and imaginary parts of the amplitude reflection coefficients for s- and p- polarizations (a), (b). Power reflection coefficients for s- and p- polarization (c). Phases of reflected amplitudes for s- p- polarizations (d). The indices of refraction for the ambient medium, film, and substrate are 1.0, 1.5, 2.0, respectively, the film thickness is 40 nm, the incident angle is  $70^\circ$ , and the wavelength is 633 nm.

is reflected. This angle is sometimes referred to as the “polarizing angle”. Also, at very low angles of incidence the power reflection coefficients and the phases are almost equal, as expected for both s- and p- polarizations. The actual amplitudes of the reflected polarization components will be equal to those of the incident polarization components weighed by their respective reflection coefficients.

## **B. Ellipsometric Definitions**

Ellipsometry usually works in reflection mode rather than in transmission mode. From here on forward when ellipsometry is mentioned reflection ellipsometry will be assumed. Referring to Fig. 1, the phase difference between the incoming beam’s s- and p- polarizations is defined as  $\delta_1$ , and that between the reflected beam’s s- and p- polarizations as  $\delta_2$ . From the two phase differences, a parameter  $\Delta$  is defined as<sup>2</sup>

$$\Delta = \delta_1 - \delta_2. \quad (19)$$

As defined,  $\Delta$  is angle that is equal to the change in phase difference, between s- and p- polarizations, that occurs upon reflection on the sample and its value varies from  $0^\circ$  to  $360^\circ$ . It is necessary to keep in mind that the amplitudes of both s- and p- polarizations may change upon reflection, without regard to the phase. Once the quantities  $r_s$  and  $r_p$  are known a quantity  $\Psi$  can be defined as follows<sup>2</sup>

$$\tan \Psi = \frac{|r_p|}{|r_s|}. \quad (20)$$

The quantity  $\Psi$  is an angle that varies from  $0^\circ$  to  $360^\circ$  and whose tangent is the ratio of the magnitudes of the total s- and p- reflection coefficients given in Eq. (17).



Furthermore, a complex quantity  $\rho$  is defined as the ratio of the total reflection coefficients

$$\rho = \frac{r_p}{r_s}. \quad (21)$$

Eqs. (19) and (20) help define the fundamental equation of ellipsometry given by<sup>2</sup> the form given

$$\rho = \frac{r_p}{r_s} = \tan \Psi \exp(j\Delta). \quad (22)$$

This equation forms the essence of ellipsometry in that the dynamics of polarization change on reflection are fully described and accounted for by its parameters.<sup>2</sup>

An ellipsometer measures the quantities  $\Psi$  and  $\Delta$ . To be able to deduce the thickness and the refractive index of a sample one needs to construct an optical model of the sample. The model generated  $(\Psi_m, \Delta_m)$  data and the experimentally measured  $(\Psi_{\text{exp}}, \Delta_{\text{exp}})$  data can be utilized in a regression algorithm to calculate the properties of the sample being analyzed. The idea in the regression algorithm is to minimize the error between the theoretical and the experimental data, using a merit function, until a convergence condition (an acceptable error) is met. Whether convergence is quickly reached depends mainly on whether the optical model is correct, although the type of regression algorithm used does influence the convergence time to some extent.

### C. Representation of Polarization by Ellipsometric Angles

Elliptical polarization is the most general state of polarization with linear and circular polarizations being its two special cases. Referring to Fig. 4, let assume a monochromatic light wave traveling along the positive  $z$  axis and having components along the  $x$  and  $y$  axes,

$$\begin{aligned} E_x(t) &= X \cos(-\omega t + \delta_x), \\ E_y(t) &= Y \cos(-\omega t + \delta_y), \end{aligned} \quad (23)$$

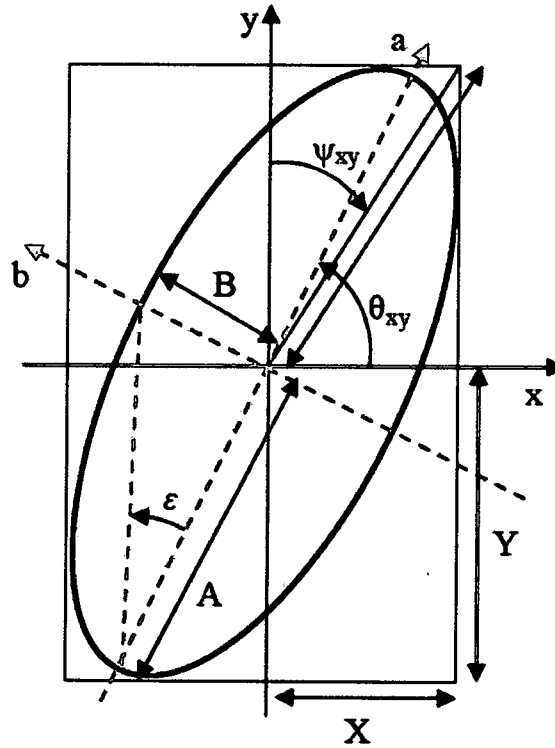


Fig. 4: Characterization of the ellipse of polarization

where  $\omega$  is the angular frequency,  $X$  and  $Y$  are the amplitudes of the  $x$  and  $y$  components of the wave,  $\delta_x$  and  $\delta_y$  are their absolute phases at the initial time  $t = 0$ . If the vector field were frozen in time its endpoint would perform a fast motion along an elliptic trajectory limited to the intervals  $\pm|X|$  and  $\pm|Y|$  in the  $x$  and  $y$  directions, respectively. The equation

describing the elliptical trajectory of the endpoint of the vector field results from Eq. (22) by getting rid of the time dependence as follows,<sup>3,4</sup>

$$\begin{aligned} YE_x \sin \delta_y - XE_y \sin \delta_x &= -XY \cos(\omega t) \sin(\delta_x - \delta_y), \\ YE_x \cos \delta_y - XE_y \cos \delta_x &= XY \sin(\omega t) \sin(\delta_x - \delta_y). \end{aligned} \quad (24)$$

Squaring and adding Eqs. (24) gives the equation of the ellipse,

$$Y^2 E_x^2 + X^2 E_y^2 - 2XY E_x E_y \cos(\delta_x - \delta_y) = X^2 Y^2 \sin^2(\delta_x - \delta_y). \quad (25)$$

The elliptic vibration is completely described by four real parameters,  $X$ ,  $Y$ ,  $\delta_x$ , and  $\delta_y$ , but the sum  $X^2 + Y^2$  is proportional to the intensity of the wave and therefore does not describe the polarization.  $\delta_x$  and  $\delta_y$  are phases and are not observable ellipsometric parameters due to the very short period of oscillation,  $2\pi/\omega$ .

Let's assume that  $X = E_0 \sin \Psi_{xy}$  and  $Y = E_0 \cos \Psi_{xy}$  with  $E_0 > 0$  and the angle  $\Psi_{xy}$  restricted to the first quadrant. With these assumptions in place,  $\tan \Psi_{xy}$  is the amplitude of the vibrations along the x axis measured relative to the amplitude along the y-axis, and carries the same meaning as in Eq. (20). There is also a relative phase shift of the vibrations along the x-axis with respect to the y-axis, called  $\Delta_{xy}$  and carries the same meaning as in Eq. (19). So, the two angles describing the ellipse of polarization in the xyz coordinate system are<sup>3-5</sup>

$$\tan \Psi_{xy} = X/Y, \Psi_{xy} \in [0, \pi/2], \Delta_{xy} = \delta_x - \delta_y, \Delta_{xy} \in [-\pi, \pi]. \quad (26)$$

Using the two angles and the amplitude  $E_0$ , the polarization ellipse of Eq. (25) becomes,

$$\frac{E_x^2}{E_0^2} + \tan^2 \Psi_{xy} \frac{E_y^2}{E_0^2} - 2 \tan \Psi_{xy} \frac{E_x}{E_0} \frac{E_y}{E_0} \cos \Delta_{xy} = \sin^2 \Psi_{xy} \sin^2 \Delta_{xy} . \quad (27)$$

As mentioned earlier, the pair of angles  $(\Psi, \Delta)$  are very useful in the treatment of polarized light. However, it is important to note that these angles depend on the chosen coordinate system in the plane of polarization. This fact is emphasized by the  $xy$  subscripts in the symbols used to designate the angles. When looking against the direction of propagation, the vibration motion is in the clockwise direction when  $\Delta_{xy} > 0$ , and the polarization is then said to be right-handed elliptical polarization.<sup>5</sup> The motion is in the counter-clockwise direction when  $\Delta_{xy} < 0$ , and the polarization is said to be left-handed elliptical polarization.

The  $xyz$  coordinate system corresponds to the observation coordinate system in the laboratory. But, there is a simpler way of characterizing the polarization ellipse in its local coordinate, i.e. the coordinate whose axes are parallel to the major and minor axes of the ellipse. Referring again to Fig. 4, let  $a$  be the coordinate along the ellipse's major axis of the length  $2A$ , and  $b$  the coordinate along the ellipse's minor axis of length  $2B$ , with  $0 \leq B \leq A \leq E_0$ . In the  $a$ - $b$  coordinate system the components of the electric field vector are<sup>3</sup>

$$\begin{aligned} E_a &= E_x \cos \theta_{xy} + E_y \sin \theta_{xy}, \\ E_b &= -E_x \sin \theta_{xy} + E_y \cos \theta_{xy}, \end{aligned} \quad (28)$$

where the angle  $\theta_{xy}$  between the positive directions of the  $x$  and  $a$  axes is called *azimuth*.

It defines the orientation of the ellipse and can be confined to the interval  $[-\pi/2, \pi/2]$ .

Using Eqs. (28) the ellipse equation in the  $a$ - $b$  coordinate system is<sup>3</sup>

$$B^2 E_a^2 + A^2 E_b^2 = A^2 B^2. \quad (29)$$

The second angle in the a-b coordinate system is given by the ratio B/A, which is independent of the coordinate system. The geometry of the system shows that

$$\tan \varepsilon = \pm \frac{B}{A}, \varepsilon \in [-\pi/4, \pi/4], \quad (30)$$

assuming positive and negative values of  $\varepsilon$  for right-handed and left-handed polarizations, respectively. The dimensionless value of  $\tan \varepsilon$ , designated by  $e$ , is called *ellipticity* and varies within the interval  $[-1, 1]$ . So, the pair  $(\Psi, \Delta)$  is equivalent to the pair  $(\varepsilon, \theta)$ .

Finally, a comparison of the equations of the polarization ellipse, i.e. Eq. (27) and Eq. (29), in both coordinate systems leads to the following relations<sup>3</sup>

$$\begin{aligned} X^2 &= A^2 \cos^2 \theta_{xy} + B^2 \sin^2 \theta_{xy}, \quad Y^2 = A^2 \sin^2 \theta_{xy} + B^2 \cos^2 \theta_{xy}, \\ X^2 + Y^2 &= A^2 + B^2 = E_0^2, \quad X^2 - Y^2 = (A^2 - B^2) \cos 2\theta_{xy}, \\ XY |\sin \Delta_{xy}| &= AB, \quad 2XY \cos \Delta_{xy} = (A^2 - B^2) \cos 2\theta_{xy}. \end{aligned} \quad (31)$$

The lengths of the major and minor axes are

$$\begin{aligned} A &= E_0 \sqrt{\frac{1 + \sqrt{1 - \sin^2 2\Psi_{xy} \sin^2 \Delta_{xy}}}{2}}, \\ B &= E_0 \sqrt{\frac{1 - \sqrt{1 - \sin^2 2\Psi_{xy} \sin^2 \Delta_{xy}}}{2}}. \end{aligned} \quad (32)$$

From Eqs. (30) and (31) the following conversions between the ellipsometric angles are obtained<sup>3</sup>

$$\tan 2\theta_{xy} = -\tan 2\Psi_{xy} \cos \Delta_{xy}, \quad \sin 2\varepsilon = \sin 2\Psi_{xy} \sin \Delta_{xy}. \quad (33)$$

Conversely,

$$\cos 2\Psi_{xy} = -\cos 2\varepsilon \cos 2\theta_{xy}, \quad \tan \Delta_{xy} = \frac{\tan 2\varepsilon}{\sin 2\theta_{xy}}. \quad (34)$$

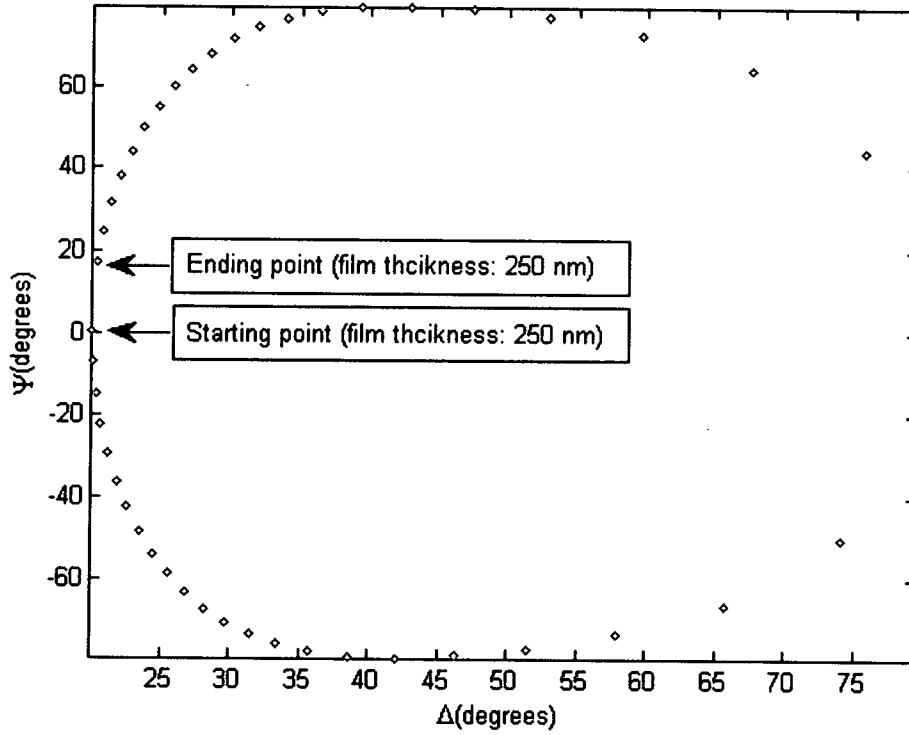


Fig. 5:  $\Psi$  and  $\Delta$  values for  $70^\circ$  incidence angle and film thickness values from 0 – 250 nm. The refractive indices of the ambient, film, and substrate are 1.0, 1.5, 3.87, respectively.

For an illumination wavelength of 633 nm, an angle of incidence of  $70^\circ$ , and a range of film thicknesses [0 nm, - 250nm], Fig. 5 shows that the angle  $\Psi$  and  $\Delta$  describes a trajectory that closes on itself as the thickness of the film ( $\text{SiO}_2/\text{Si}$ ) increases. The starting point of the trajectory corresponds to zero thickness and the closing point (thickness) is given by<sup>2</sup>

$$d = \frac{\lambda}{2\sqrt{n_f^2 - \sin^2 \theta_i}}, \quad (35)$$

where  $\lambda$  is the illumination wavelength,  $n_f$  the refractive index(  $n_f=1.5$  in Fig. 5) of the film, and  $\theta_i$  the angle of incidence. Depending on the refractive index or whether a film is absorbing the  $\Psi$  and  $\Delta$  trajectory may not be a closed path.

#### **D. Fitting Models to Data**

After the data has been collected, fitting the experimental data to a model is a difficult task. A good set of data does not guarantee the right result if, for example, the data is fit to a wrong model, the figure of merit is an incorrect error estimator, or if the regression algorithm used for fitting is not robust enough to handle noise in the data, etc. Clearly, the fitting process is critical to getting to getting useful results. Even the most accurate and reproducible experiments can be rendered useless by inappropriate modeling.

The task of fitting data to a model consists mainly of three major tasks:

1. Selecting a model.

The number of layers is set, and the basic structure concerning the contents of each layer is defined. At this stage one decides if there is an anisotropic layer, and whether or not interface layers are modeled as a single effective medium approximation, or if a more complicated graded interface is to be used.

2. Assign optical functions to each layer.

Here, the decision must be made to use existing values of optical functions or some sort of parameterization. For example, if the sample consists of thin-film

SiO<sub>2</sub> grown on silicon, it is very likely that the optical function of the substrate layer will be very close to the reference values of crystalline silicon. The film might be modeled with three layers and a substrate: surface roughness / amorphous SiO<sub>2</sub> / substrate-film interface / crystalline silicon. The surface roughness (the top layer) may be best modeled as a Bruggeman effective medium consisting of 50% air and 50% SiO<sub>2</sub>, while the middle layer might be best modeled using a single Lorentz oscillator.<sup>6</sup> The interface layer might again be modeled using a 2-medium Bruggeman effective medium, consisting of a 50% layer 2 and 50% silicon. The initial values for all parameters and film thicknesses must be assigned, and the floating parameters (variable parameters in the model) selected.

### 3. Fit the data.

The last step is the fitting process itself. This step requires that the metric be chosen that will decide between good and bad fits to the data. Moreover, this metric must be able to tell us, at the least in a qualitative sense, whether or not the model actually fits the data, given the error limits of the data. The error in the data is calculated using a figure of merit which is a statistical error function.<sup>6</sup> If the figure of merit is inappropriate, it may be that one accepts a wrong model, or unnecessarily complicates an otherwise reasonably valid model. It is also in this step that the choice of the numerical analysis optimization algorithm must be made.



### D1. Figures of Merit

The most critical choice in any numerical fitting procedure is the figure of merit, which tells the user how well the model, with the present set of parameters, actually fits the data.<sup>7</sup> There are two common choices used as figure of merit for ellipsometry data analysis. The oldest, called either the unbiased estimator or the mean squared error (MSE), is given by

$$MSE = \sum_{i=1}^N [\Psi_{\text{exp}}^i(\lambda) - \Psi_{\text{calc}}^i(\lambda, Z)]^2 + [\Delta_{\text{exp}}^i(\lambda) - \Delta_{\text{calc}}^i(\lambda, Z)]^2. \quad (36)$$

The other is the reduced  $\chi^2$  (chi squared), which is given by<sup>6</sup>

$$\chi^2 = \sum_{i=1}^N \left[ \frac{\Psi_{\text{exp}}^i(\lambda) - \Psi_{\text{calc}}^i(\lambda, Z)}{\sigma_{\Psi}^i(\lambda)} \right]^2 + \left[ \frac{\Delta_{\text{exp}}^i(\lambda) - \Delta_{\text{calc}}^i(\lambda, Z)}{\sigma_{\Delta}^i(\lambda)} \right]^2. \quad (37)$$

In both Eqs. (36) and (37),  $N$  is the total number of data points taken,  $(\Psi_{\text{exp}}(\lambda), \Delta_{\text{exp}}(\lambda))$  are the data pairs of the experimental angles,  $(\Psi_{\text{calc}}(\lambda, Z), \Delta_{\text{calc}}(\lambda, Z))$  are the data pairs of calculated ellipsometric angles for a particular set of the variable parameters indicated by  $Z$  (thickness, refractive index, etc.), and  $\lambda$  is the illumination wavelength. The only difference between Eq. (36) and Eq. (37) is the experimental errors  $\sigma_{\Psi}(\lambda)$  and  $\sigma_{\Delta}(\lambda)$  in the denominator of Eq. (37). From a mathematical point of view, this is a big difference and has far-reaching consequences concerning the conclusion that can be drawn from an ellipsometric data fit.

When Eq. (36) is used as a figure of merit function, it is assumed that all experimental errors are unmeasurable and that they are the same for each data point.<sup>6</sup> Error limits on

the fit are often quoted *assuming* that the selected model is the right model, but this is the very thing that is to be determined from ellipsometry experiments. Moreover, the actual value of the MSE has the dimensions of the chosen parameterization of the experimental data, and is therefore meaningless; one never knows when a good fit is actually obtained. Therefore, this figure of merit is used to analyze ellipsometric data when there is no possible way of obtaining an estimate of the errors in the experimental data.

The a priori assumption on the model and the errors in the data, the reduce  $\chi^2$  is often used as the figure of merit (there are several other merit functions available for special types fitting models). The reduced  $\chi^2$  is unitless, and is in fact a measure of the goodness of fit. If  $\chi^2 \approx 1$ , then the model fits the data, but if  $\chi^2 \gg 1$ , then the model does not fit the data. Furthermore, the results of the fitting procedure are independent of the representation of the data, if the errors are propagated into the data into the data representation used in the fitting procedure.<sup>6</sup>

The determination of proper error limits from the results of the fit is very important in the fitting experimental data. If the MSE is used as the figure of merit, then any error limits obtained are only relative and again assume that the model selected is the correct model. However, error limits obtained from a fitting procedure using  $\chi^2$  as the figure of merit can be statistically related (only approximately) to the actual error limits of the fitted parameters, and therefore have considerably more validity.<sup>7</sup>

## **D2. Convergence Routines**

There are many convergence routines (algorithms) used in data fitting procedure.<sup>8-14</sup> Based on performance, each algorithm is well suited for particular cases of data fitting.

We will briefly discuss the Levenberg-Marquardt algorithm<sup>6, 7</sup> since it is used in data fitting procedures in this work. Because of its robustness to noise and its simplicity and efficiency, the Levenberg-Marquardt algorithm is used for nonlinear data fitting. The algorithm is a combination of two different numerical analysis procedures: the inverse Hessian method and the steepest descent method.<sup>7</sup> The latter method is used far from the location of the minimum, switching continuously to the former as the minimum is approached. The merit function to be minimized is given by Eq. (37). Rewriting Eq. (37) to show the dependence of the parameter vector  $Z$ :

$$\chi^2(Z) = \sum_{i=1}^N \left[ \frac{\Psi_{\text{exp}}^i(\lambda) - \Psi_{\text{calc}}^i(\lambda, Z)}{\sigma_{\Psi}^i(\lambda)} \right]^2 + \left[ \frac{\Delta_{\text{exp}}^i(\lambda) - \Delta_{\text{calc}}^i(\lambda, Z)}{\sigma_{\Delta}^i(\lambda)} \right]^2. \quad (38)$$

The Levenberg-Marquardt algorithm needs the gradient and the second derivative of Eq. (38). At the minimum of  $\chi^2(Z)$  with respect to the parameters  $Z$ , the gradient will be zero.

In the neighborhood of the minimum, the gradient is given by

$$\begin{aligned} \frac{\partial \chi^2}{\partial Z_k} = & -2 \sum_{i=1}^N \left[ \frac{\Psi_{\text{exp}}^i(\lambda) - \Psi_{\text{calc}}^i(\lambda, Z)}{\sigma_{\Psi}^i(\lambda)^2} \right] \frac{\partial \Psi_{\text{calc}}^i(\lambda, Z)}{\partial Z_k} \\ & - \left[ \frac{\Delta_{\text{exp}}^i(\lambda) - \Delta_{\text{calc}}^i(\lambda, Z)}{\sigma_{\Delta}^i(\lambda)^2} \right] \frac{\partial \Delta_{\text{calc}}^i(\lambda, Z)}{\partial Z_k}. \end{aligned} \quad (39)$$

Taking another partial derivative gives

$$\begin{aligned} \frac{\partial^2 \chi^2}{\partial Z_k \partial Z_l} = & 2 \sum_{i=1}^N \left\{ \frac{1}{\sigma_{\Psi}^i(\lambda)^2} \frac{\partial \Psi_{\text{calc}}^i(\lambda, Z)}{\partial Z_k} \frac{\partial \Psi_{\text{calc}}^i(\lambda, Z)}{\partial Z_l} - \left[ \Psi_{\text{exp}}^i(\lambda) - \Psi_{\text{calc}}^i(\lambda, Z) \right] \frac{\partial^2 \Psi_{\text{calc}}^i(\lambda, Z)}{\partial Z_k \partial Z_l} \right\} \\ & + 2 \sum_{i=1}^N \left\{ \frac{1}{\sigma_{\Delta}^i(\lambda)^2} \frac{\partial \Delta_{\text{calc}}^i(\lambda, Z)}{\partial Z_k} \frac{\partial \Delta_{\text{calc}}^i(\lambda, Z)}{\partial Z_l} - \left[ \Delta_{\text{exp}}^i(\lambda) - \Delta_{\text{calc}}^i(\lambda, Z) \right] \frac{\partial^2 \Delta_{\text{calc}}^i(\lambda, Z)}{\partial Z_k \partial Z_l} \right\}. \end{aligned} \quad (40)$$

The second order terms in Eq. (40) can be omitted since they are usually small and can be the source of large errors when a model does not closely fit the data.<sup>7</sup> Eq. (40) then reduces to

$$\begin{aligned} \frac{\partial^2 \chi^2}{\partial Z_k \partial Z_l} = & 2 \sum_{i=1}^N \left\{ \frac{1}{\sigma_{\Psi}^i(\lambda)^2} \frac{\partial \Psi_{calc}^i(\lambda, Z)}{\partial Z_k} \frac{\partial \Psi_{calc}^i(\lambda, Z)}{\partial Z_l} \right\} \\ & + 2 \sum_{i=1}^N \left\{ \frac{1}{\sigma_{\Delta}^i(\lambda)^2} \frac{\partial \Delta_{calc}^i(\lambda, Z)}{\partial Z_k} \frac{\partial \Delta_{calc}^i(\lambda, Z)}{\partial Z_l} \right\}. \end{aligned} \quad (41)$$

Let's define

$$-\frac{1}{2} \frac{\partial \chi^2(Z)}{\partial Z_k} = \beta_k, \quad (42)$$

and

$$\frac{1}{2} \frac{\partial^2 \chi^2(Z)}{\partial Z_k \partial Z_l} = \alpha_{kl}. \quad (43)$$

The  $\alpha_{kl}$  matrix is usually called the curvature matrix, and is equal to  $\frac{1}{2}$  the equivalent of the Hessian matrix of least squares fitting procedures.

The Levenberg-Marquardt nonlinear fitting procedure requires that a third parameter  $\wp$ , a dumping factor, be defined (most textbooks refer to this as  $\lambda$ ) such that a new matrix  $\alpha'_{ii}$  is defined

$$\alpha'_i = \alpha_i(1 + \wp). \quad (44)$$

This dumping factor plays an important role in that it adaptively adjusts the size of the fitting parameter's incremental step necessary for the next iteration computations. With all the terms defined above, the Leven-Marquardt algorithm goes (graphically, see Fig. 6) as follows:

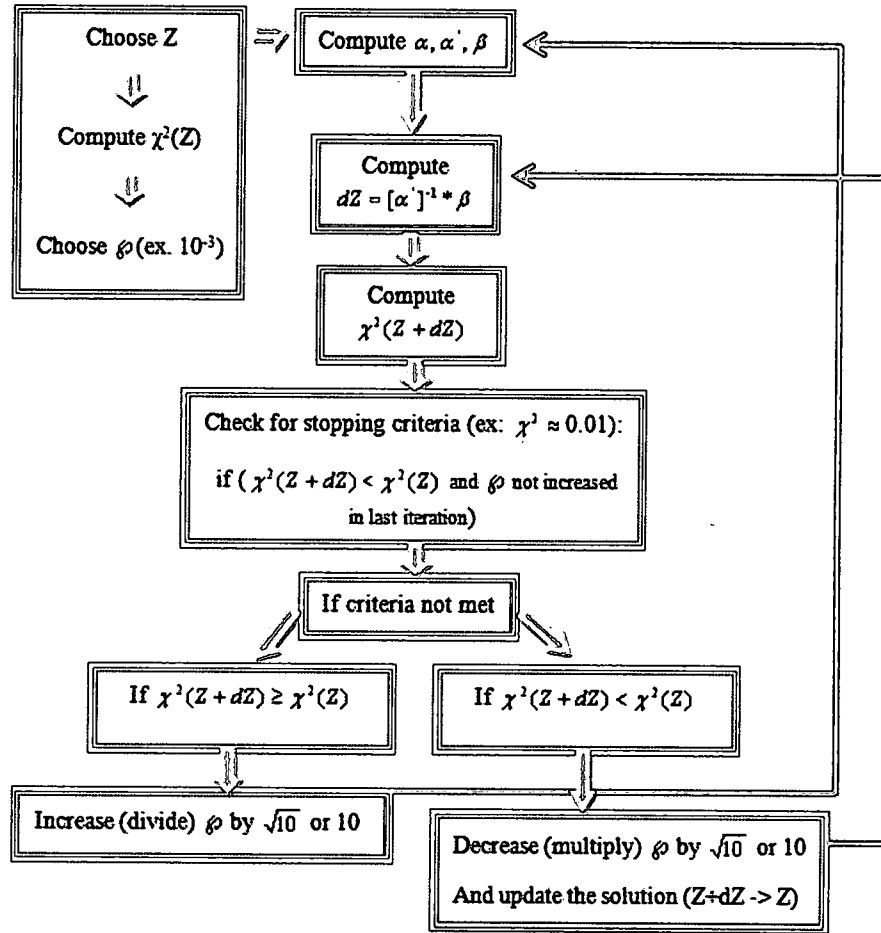


Fig. 6: Execution flow diagram of the Levenberg-Marquardt algorithm.

The execution steps illustrated in Fig. 6 are:

1. Make a reasonable estimation of the parameter vector  $Z$ .
2. Compute  $\chi^2(Z)$ .

3. Choose a reasonable initial value of  $\wp$  (usually  $\sim 0.001$ )
4. Calculate the  $\alpha$ ,  $\beta$ , and  $\alpha'$  matrices.
5. Calculate  $\delta Z = [\alpha']^{-1} \beta$  and evaluate  $\chi^2(Z + \delta Z)$ .
6. Check for stopping the iteration if  $\chi^2(Z + \delta Z) < \chi^2(Z)$  and if  $\wp$  was not increased for the last time.
7. If  $\chi^2(Z + \delta Z) \geq \chi^2(Z)$ , increase  $\wp$  by a large factor ( $\sqrt{10}$  or 10), and go back to 5.
8. If  $\chi^2(Z + \delta Z) < \chi^2(Z)$ , decrease  $\wp$  by a large factor ( $\sqrt{10}$  or 10), update the solution for the z-vector  $Z + \delta Z \rightarrow Z$ , and go back to 4.

Step (1) involves the initial guess for the parameter estimation. Given the nonlinearity of the data analysis problem, this is a critical step because it is very easy to have the algorithm converge to a local minimum and not the global minimum. For many problems this is not an issue, since the user knows the approximate position in parameter space where the solution lies. However, if the film structure is very complicated or the materials involved are unknown or complicated composites, one must, first, use other numerical techniques to find the initial estimate. One way to do this is to search over all possible parameter space using a grid search or a Monte Carlo search.<sup>6</sup> Another way is to manually change individual elements of the parameter vector  $Z$  until the fit looks realistic. In both cases, it is important to use both the merit function and the user's intuition as a guide to determine when a close solution is obtained.

Step (6) indicates that one must have one or more criteria for stopping the iteration. Generally, it is not a good idea to stop the iteration when  $\phi$  has been increased. Nor is it a good idea to continue the iteration process if each iteration is not decreasing  $\chi^2(Z)$  very much (usually 0.001). Once the solution vector  $Z$  has been found, the covariance matrix  $\alpha^{-1}$  can be calculated, as can approximate errors in the solution vector  $Z$ .<sup>7</sup> For the 95% confidence interval, the approximate correlated errors in the elements of the parameter vector are given by  $2\sqrt{\alpha_i^{-1}}$ , while the uncorrelated errors are given by  $2/\sqrt{\alpha_i^{-1}}$ . The cross-correlation coefficients are given approximately by the elements of the symmetric matrix  $\alpha^{-1}$ .<sup>7</sup>

## CHAPTER II

### The Basic Foundations of Ellipsometry

#### A. Brief History of Ellipsometry

The history of measuring polarization change upon reflection dates back in the late 1800s, although it was not referred to as “ellipsometry” then.<sup>14</sup> The technique of ellipsometry as such is conventionally attributed to Paul Drude who used it to determine the dielectric function of various metals and dielectrics. For 75 years following Drude's pioneering work, only a handful of ellipsometric studies were carried out. The name “ellipsometry” was introduced in 1945 in an article published in *Review of Scientific Instruments* by Alexander Rothen.<sup>2</sup> With the coming of the computer in the late 1960's ellipsometry has gone through a major revolution in that ellipsometric data collection and processing is no longer a daunting task it once was. Of particular interest is how the technique has become the standard in the semiconductor industry for characterization of thin-films and microchips in the visible, NIR, and UV regions.

Among many parameters that ellipsometry measures, the thickness and the refractive index of a sample are the most common. Existing ellipsometric techniques are capable of producing a sample's topographic image. Ellipsometry directly measures two parameters,  $\psi$  and  $\Delta$ , which are defined in Eqs. (19) and (20). Once the  $(\Psi, \Delta)$  pairs are measured, an optical model of the sample and the experimentally measured data can be used in a



regression algorithm to calculate the thickness and the refractive index among other characteristic properties of the sample under examination. Therefore a complete ellipsometric measurement process consists of two major steps: data collection (instrumentation and measurement), and data processing (computation).

## **B. Basic Optical Elements Used in Ellipsometry**

The basic instrumentation of ellipsometry usually requires the following optical elements:

- A light source: a monochromatic light source is usually used for fixed wavelength ellipsometry. A basic research ellipsometer can use a Helium-Neon laser with a wavelength of 633 nm for illumination. Spectroscopic ellipsometry requires the use of a source with a broad spectral band (typically 250 nm to 1200 nm).
- A linear polarizer (LP). This component produces light in a special state of polarization. A linear polarizer works by suppressing or redirecting one component of the incident polarization, thus allowing only the other component to pass through. By rotating such a polarizer, one may produce a beam of linearly polarized light from unpolarized incident light with the direction of polarization corresponding to the orientation of the transmission axis of the polarizer.
- An analyzer (this is usually another polarizer) to help determine the state of polarization of the reflected beam. Usually the incident beam is already polarized and the analyzer measures the ratio of the p- and the s- polarization components. A good analyzer would transmit light only along its transmission axes, thus allowing no light to leak that is polarized orthogonally with respect to the

transmission axis. Care must be taken to use polarizers and analyzers whose wavelength of operating spectral range is covered by the source's spectral band.

- A detector to measure the irradiance of the light being reflected from the sample. A detector with a wide active area is preferred in ellipsometry for an efficient collection of light. The source wavelength must always fall within the operating spectral range of the detector.
- A computation capability to process the data and interpret the results (this can be a computer that automates the entire system, i.e. controls various devices, collects the data and analyzes it).

Advanced ellipsometric configurations usually use other elements such as quarter-wave plates (QWP), half-wave plates (HWP), electro-optic modulators, and beam splitters to perform various tasks in the instrument. Quarter-wave and half-wave plates are generally referred to as *retarders* or *compensators* from the fact that they operate on the incident light by introducing phases of  $\pi/2$  and  $\pi$ , respectively, between the polarization components along their fast and slow axes. According to their designs certain ellipsometers may require that the beam in the illumination arm of the instrument be either circularly or elliptically polarized. In such a case one would need to generate the desired illumination polarization by combining a polarizer and a QWP aligning them properly. The polarizer-QWP combination can also be used to analyze an elliptical polarization. Half-wave plates can be used to manipulate the beam polarization before or after reflection on the sample. For example, two HWPs can act as a polarization rotator with the rotation angle being determined by the angle between their fast axes. Some ellipsometer designs incorporate a modulator of some kind to modulate the ellipsometric

signal at relatively high frequencies. The most widely used modulators in ellipsometers are Faraday modulators and photo-elastic modulators (PEM) since they can be modulated at a frequency as high as 100 KHz, which is fast enough by ellipsometric standards. Beam splitters are primarily used to steer the beam and can be used where appropriate.

### **C. Common Ellipsometer Configurations**

Nulling ellipsometry is the most widely used type and the research work presented in this thesis is based on implementing a variation of the nulling technique. Most arrangements discussed in this section are nulling ellipsometer arrangements, however a few other configurations will be discussed as well. These arrangements only represent the conceptual models since in practice modifications are always introduced to implement functional systems. The nulling technique advantage resides in its working principle, i.e. the determination of the reflected polarization by simply determining the angles of the polarizer, the analyzer, and the compensator when an intensity null (zero intensity) is detected. Photometric ellipsometry and interferometric ellipsometry, for example, rely on the intensity of light in order to determine the reflected polarization and therefore are subject to the signal-to-noise (SNR) ratio penalty caused by the intensity fluctuations. By simply detecting a null and then determining the reflected polarization using the angular position of the optical elements in the ellipsometer, the measurements are not, or only negligibly, affected by the fluctuations of the light intensity. This is a major advantage that the nulling technique offers. In addition, it is easier to accurately measure a null than it is to accurately measure a nonzero intensity. In this regard too, the nulling technique offers an advantage.

### C1. Nulling Ellipsometer: PCSA Configuration

The manual nulling scheme was the first method used to measure polarization change upon reflection. Few nulling ellipsometric setups are explored below in order to understand the basic functioning principle of a nulling instrument.

Conceptually a nulling ellipsometer is a simple system that uses a polarizer, an analyzer, a quarter-wave plate (QWP), and a detector (or screen) to detect the presence of a null (zero irradiance at the detector).<sup>2</sup> One conceptual ellipsometer is shown in Fig. 7. Unpolarized light from the source goes through the polarizer (P) and becomes linearly polarized in the direction of

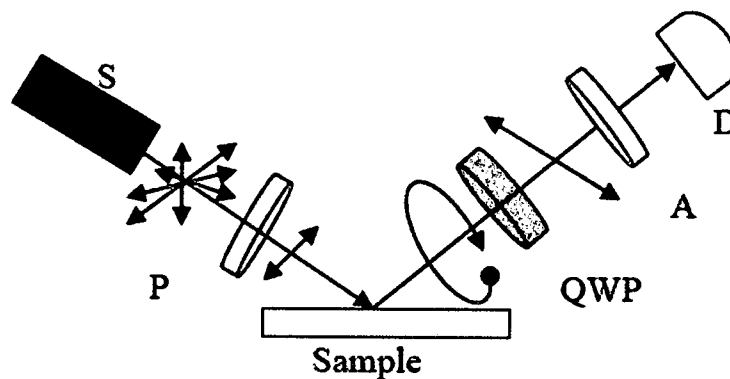


Fig. 7: A conceptual nulling ellipsometer arrangement: The PCSA configuration. S (source, i.e. laser), P (polarizer), A (analyzer), D (detector).

the polarizer's transmission axis. On the sample (S) the incident linear polarization picks up an amount of ellipticity and becomes elliptically polarized. This elliptical polarization is converted into linear polarization by properly adjusting the QWP angle. The linear polarization emerging from the plate can be easily nulled by adjusting the angle of the analyzer (A). Note that if the QWP angle is not properly adjusted, a minimum, not a null,

will be found. In practice, the QWP is usually placed right after the polarizer as shown in Fig. 8. Generally, the combination of a polarizer and a QWP behaves as an elliptical polarizer. The ellipticity can be adjusted by changing the angle between the transmission axes of the two elements so that the ellipticity is totally cancelled (compensated for by the QWP) upon reflection. When such a condition is reached, the reflected light is linearly polarized. In the setup illustrated in Fig. 7 the QWP is fixed at  $45^\circ$ . The null is found by iteratively adjusting the polarizer's and the analyzer's angles. Note that there will be several combinations of the analyzer-polarizer angles that will result in a null.

Usually all angles are considered positive in the counterclockwise direction when looking into the beam. If the polarizer's angle  $P$  and the analyzer's angle  $A$  are restricted to certain ranges to avoid redundant angles (angles  $180^\circ$  apart), then the various combinations of  $P$  and  $A$  that result in a null can be grouped into two zones<sup>2</sup>. For zone 2,

$$-45^\circ < P_2 < 135^\circ, \quad 0^\circ < A_2 < 90^\circ, \quad \text{QWP} = 45^\circ, \quad (45)$$

and zone 4,

$$-135^\circ < P_4 < 45^\circ, \quad -90^\circ < A_4 < 0^\circ, \quad \text{QWP} = 45^\circ. \quad (46)$$

The ellipsometric parameters  $\Delta$  and  $\psi$ , as defined earlier are related as follows:

$$\Delta_2 = 270^\circ - P_2, \quad \Psi_2 = A_2, \quad \Delta_4 = 90^\circ - 2P_4, \quad \Psi_4 = -A_4. \quad (47)$$

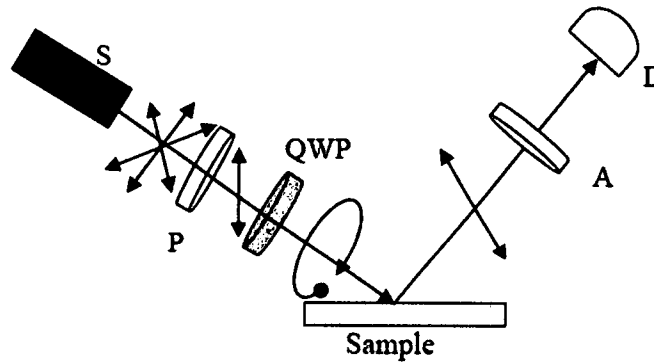


Fig. 8: A conceptual nulling arrangement with the QWP inserted before the sample.

Fig. 8 illustrates the detected intensity plot near a null. The change in intensity as a function of the polarizer's angle is very small near the null point. Since the intensity curve is symmetric (see Fig. 9) with respect to the null position, a better way of measuring the exact angular position of the null may be to measure two angular positions that give equal intensities (near the apparent null) one from each side of the curve and divide the sum of the angles by two.

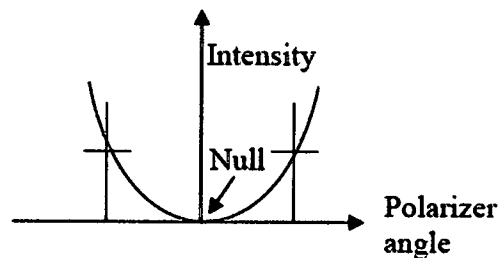


Fig. 9: Intensity vs. polarizer's angle near the null.

## C2. Rotating Elements Ellipsometer

A rotating ellipsometer automatically rotates its polarizer and analyzer to find a null position. Fig. 9 illustrates a setup of a rotating elements ellipsometer. Unlike in Fig. 8, the

polarizer in Fig. 10 is not fixed. It is rotated simultaneously with the analyzer. For a rotating elements ellipsometer the signal on the photodetector is a sinusoidal varying intensity.<sup>2</sup> Generally, the minima of this intensity do not correspond to the intensity extinction (null), i.e. the intensity does not go to zero. These minima deepen and eventually go to zero when the polarizer and the analyzer are alternatively adjusted to find a proper combination of their angular positions that leads to a null. With the advent of high precision electronics the search for these angles is often done by computer-controlled servomotors that control and encode the angular positions of the polarizer and the analyzer. The encoded angles corresponding to the null occurrences are used in Fourier-analyzed to calculate the values of  $\Psi$  and  $\Delta$ . The QWP is fixed with its fast axis perpendicular to the plane of incidence and can be placed in the beam or removed

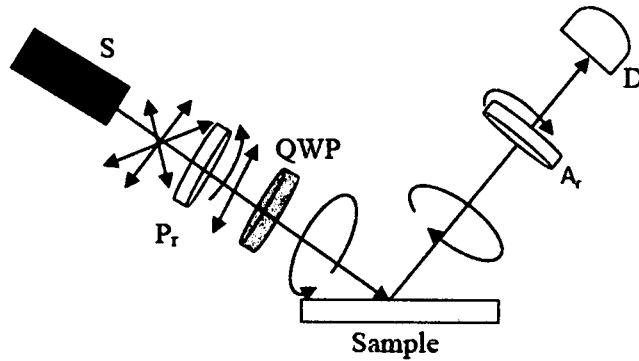


Fig. 10: A rotating polarizer null ellipsometer arrangement. The subscript "r" indicates a rotating element.

from it. With the polarizer fixed at an angle the arrangement becomes a photometric instrument instead of a null instrument. Its signal is sinusoidal and is given by<sup>2</sup>

$$I(t) = I_0 [1 + \alpha \cos 2A(t) + \beta \sin 2A(t)] \quad (48)$$

where

$$A(t) = 2\pi ft + A_c, \quad (49)$$

with  $A(t)$  being the time varying analyzer angle,  $f$  being the frequency of the rotation and  $A_c$  being a constant angle offset.  $I_0$  is the average intensity and  $\alpha$  and  $\beta$  are Fourier coefficients (to be calculated).  $\Psi$  and  $\Delta$  are found using the following relationships<sup>2</sup>

$$\begin{aligned} \cos \Delta &= \pm \sqrt{\frac{\beta^2}{1 - \alpha^2}}, \\ \tan \Psi &= \sqrt{\frac{1 + \alpha}{1 - \alpha}}. \end{aligned} \quad (50)$$

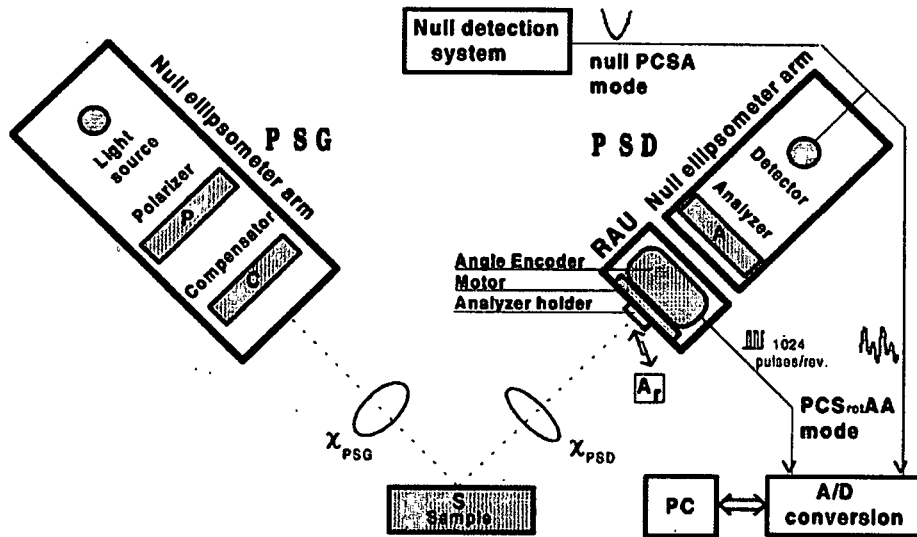


Fig. 11: Rotating null ellipsometer (figure published in ref. 15).  $P_r$ : rotating polarizer,  $A_r$ : rotating analyzer; A: non-rotating analyzer, PSG: polarization state generation, PSD: polarization state detection.

Rotating-elements configurations are widely used in the implementation of nulling ellipsometry. A more realistic rotating null ellipsometer setup can be seen in Fig. 11.<sup>15</sup> This configuration is more advanced and beyond a simple conceptual model. The first



arm contains a source, a polarizer, and a compensator while the second arm contains a motor that controls and encode the analyzer angle, the analyzer itself, and a detector. The system extends outside where signal amplification, conditioning, and processing are done using an analogue-to-digital (A/D) converter and a computer. Assuming that the second analyzer A (fixed) is removed, this arrangement becomes basically a variation of the rotating analyzer configuration already mentioned above. The basic optical elements are arranged from light source to detector as follows: polarizer – compensator – sample – analyzer. This arrangement order is often referred to as PCSA arrangement. The signal received at the detector, as shown in the diagram, shows that a null in the irradiance can be produced given an appropriate polarizer-compensator-analyzer angular combination when analyzer  $A_r$  is removed from the analyzer arm. The automation of this instrument increases the accuracy with which the measurements are taken, and allows a fast collection of data. On the other side, the different optical and electronic components involved may increase the complexity of the instrumentation and the calibration.

### **C3. A Nulling Ellipsometer with PSRA Configuration**

The acronym PSRA stands for Polarizer, Sample, Rotator, and Analyzer. It tells the order in which the elements appear in the setup from light source to detector. Figure 12 illustrates the configuration of this arrangement. This setup is also known as the “Monin-Boutry” ellipsometer.<sup>16</sup> The beam from the source is linearly polarized and directed toward the sample. After reflection on the sample the light picks up a phase and becomes elliptically polarize. The elliptically polarized light enters a polarization rotator (Faraday rotator) which is driven by an ac current of frequency  $\omega_0$  through a coil. A is a linear analyzer and D is a detector. This ellipsometer functioning principle is based on the fact

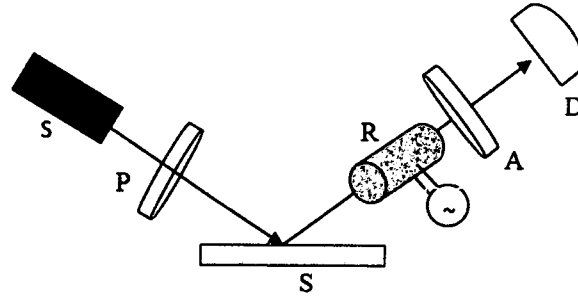


Fig. 12: The Monin-Boutry Ellipsometer (PSRA configuration).

that when the transmission axis of the linear analyzer is oriented parallel to either the major or the minor axis of the ellipse of polarization of the reflected light the detected signal will have a zero-amplitude harmonic at the modulation frequency. This means that with the polarizer set at a fixed azimuth the analyzer can be rotated until the signal component at  $\omega_0$  is nulled. The driving current in the coil generates a magnetic field given by

$$H(t) = H_m \cos \omega_0 t, \quad (51)$$

where  $H_m$  is the field amplitude and  $\omega_0$  is the frequency of the driving current. Using  $v$  as the Verdet constant,  $L$  as the length of the Faraday cell, and  $\omega$  as the driving current frequency the modulation function of the rotator can be written as<sup>16</sup>

$$\Phi = \Phi_m \cos \omega_0 t, \quad (52)$$

where

$$\Phi_m = v L H_m. \quad (53)$$

At the output of the modulator the electric field vibrations are<sup>16</sup>

$$\begin{aligned} E_x &= a \cos \omega_0 t \cos \Phi + b \sin \omega_0 t \sin \Phi, \\ E_y &= -a \cos \omega_0 t \sin \Phi + b \cos \omega_0 t \cos \Phi \end{aligned} \quad (54)$$

where  $a$  and  $b$  are the incident polarization ellipse major and minor axes, respectively. If the analyzer angle is  $\beta$  and the orientation of the ellipse is  $\theta_0$  then the general form of the signal<sup>16</sup> on the detector is given by

$$I = a^2 \cos^2(\Phi + \beta - \theta_0) + b^2 \sin^2(\alpha - \beta - \theta_0). \quad (55)$$

Assuming  $\Phi_m \ll 1$ , the signal can be expanded as a Taylor series. The first, second and third harmonic components that results from the expansion are, respectively, given as<sup>16</sup>,

$$\begin{aligned} I(0) &= \frac{b^2}{\varepsilon^2} \left[ \cos^2(\beta - \theta_0) + \frac{\Phi_m^2}{2} \cos^2 2(\beta - \theta_0) \right] \\ &+ a^2 \varepsilon^2 \left[ \sin^2(\beta - \theta_0) + \frac{\Phi_m^2}{2} \cos^2 2(\beta - \theta_0) \right], \end{aligned} \quad (56)$$

$$I(\omega_0) = K_1 a^2 (\varepsilon^2 - 1) \sin^2 2(\beta - \theta_0) \cos \omega_0 t, \quad (57)$$

$$I(2\omega_0) = K_2 a^2 (\varepsilon^2 - 1) \cos 2(\beta - \theta_0) \cos 2\omega_0 t. \quad (58)$$

The constants  $K_1$  and  $K_2$  are proportional to  $\Phi_m$ , and  $\varepsilon$  is the ellipticity angle of the polarization after reflection. Note that for  $\beta = \theta_0$  or  $\beta = \theta_0 \pm \pi/2$  the first harmonic disappears and a null occurs.

#### D. Photometric Ellipsometry

Besides the ellipsometers mentioned above there are types of ellipsometers that work based on measured intensities for a number of suitably chosen settings of the optical

components influencing the polarization state of light. These ellipsometers are referred to as photometric ellipsometers.<sup>2</sup> Unlike the nulling ellipsometers, photometric ellipsometers are well suited for use in spectroscopic ellipsometry with the consequence that the large amounts of information are collected and processed during an operation.<sup>17</sup> A very important issue in any photometric system is the sensitivity, linearity, response time, and polarization dependence of light detectors. A simple Polarizer – Sample – Analyzer (PSA) configuration provides the suitable apparatus for photometric measurements. The light intensities are measured for several properly chosen azimuths of the polarizer and analyzer. Since the analyzed state of polarization is independent of absolute intensities, one of the measured intensities can be used as a reference for the measurement of relative values. At least three independent intensity measurements are required to determine  $\psi$  and  $\Delta$ . The intensity transmitted by the analyzer is<sup>17</sup>

$$I(A) = I(P) \cos^2 P (\tan^2 \Psi \cos^2 A + \tan^2 P \sin^2 A + 2 \tan \Psi \cos \Delta \tan P \cos A \sin A). \quad (59)$$

If the intensity for  $A = \pi/2$  is taken as reference the ellipsometric angle  $\Psi$  is obtained from the relative intensity measured for  $A = 0$  as

$$\tan \Psi = \tan P \sqrt{I(0)/I(\pi/2)}. \quad (60)$$

The third intensity can be measured for  $A = \pi/4$  to obtain the ellipsometric angle  $\Delta$  through the expression<sup>17</sup>

$$\cos \Delta = \text{sgn}(P) [2I(\pi/4) - I(0) - I(\pi/2)] / [2\sqrt{I(0)I(\pi/2)}]. \quad (61)$$

From Eq. (61) one can see that it is impossible to distinguish the sign of  $\Delta$ , which is confined to an interval of the length of  $\pi$ . The values of  $P$  close to either zero or  $\pm\pi/2$  should be avoided, since they lead to a loss of sensitivity.

There are many variations of the configuration we have discussed so far. The interested reader can consult references (2) and (3) for more details.

## CHAPTER III

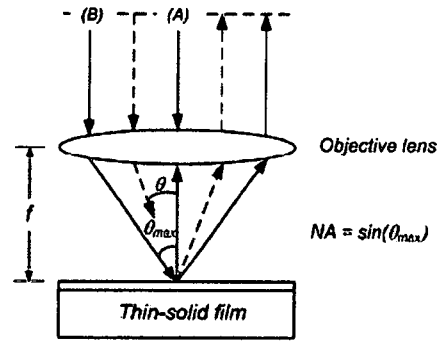
### NEW SOLUTIONS TO NEW CHALLENGES IN ELLIPSOMETRY

Ellipsometry is a nondestructive optical technique that is widely used for the characterization of thin films and interfaces. In the semiconductor industry, ellipsometry is used to simultaneously measure thin films' thickness and refractive index among many other parameters<sup>18-23</sup>. The rise of micro- and nano-structured microelectronic materials and devices, and their ever decreasing feature size, has prompted researchers to develop new ellipsometric capabilities in order to meet the challenges of fast and accurate characterization of these materials and devices. The applications of traditional ellipsometers with non-focused beams are limited due to their poor spatial resolution limitations arising from the large beam footprint on the surface under examination. This type of ellipsometers cannot be used to resolve small features that may be present on the surface. Improving the lateral resolution and the signal-to-noise ratio (SNR) of ellipsometric techniques remains of great interests to the community<sup>24-28</sup>.

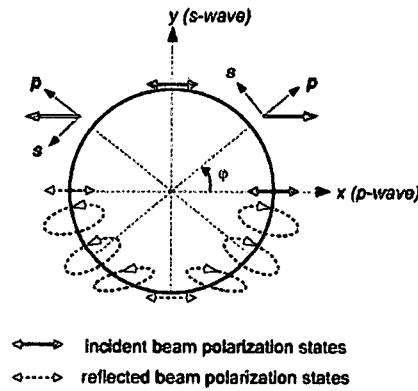
Spatially-resolved ellipsometers with the insertion of a focusing lens in the illumination arm and an imaging lens in the analyzer arm of a conventional ellipsometer have been developed in order to focus the beam and probe only a small area of a sample<sup>25, 28</sup>. Early spatially-resolved ellipsometer designs used the traditional oblique illumination configuration. In this type of configuration, the spatial resolution is significantly constrained due to the slant angle between the focused beam and the sample,

which limits the practically usable numerical aperture (NA) for the focusing and collection lenses. Moreover, the use of an objective lens introduces multiple angles of incidence in the ellipsometric signal and reduces the sensitivity of the ellipsometer. To remedy the issues related to oblique illumination, a normal illumination configuration, with a single high NA objective lens focusing the beam and collecting the reflected beam for further polarization analysis, has been adopted<sup>29, 30</sup>. The polarization signal of the reflected beam is collected in the back focal plane of the objective lens where specific angles of incidence can be selected. In this approach, the fields in the back and front focal planes are related through a Fourier transform. Each incident angle onto the sample can be mapped to a specific spatial location in the back focal plane. The spatial resolution of this type ellipsometers is improved<sup>31, 32</sup>, but the ellipsometric sensitivity and the SNR of the measurements are still limited by the pixel size of the detector. A small pixel size is preferred for high ellipsometric sensitivity. However, when the pixel size is too small the amount of signal collected by the pixel is reduced, thus leading to a low SNR.

A focused-beam ellipsometer using normal illumination configuration was recently developed by S. Ye et al.<sup>29</sup> The design principle of this ellipsometer is shown in Fig. 13(a) where the incident beam is focused on the sample by a lens and the reflected beam collected by the same lens. The beam is viewed as a collection of rays, and each incident ray carries a linear polarization. Each reflected ray carries a polarization, generally elliptical, as seen in Fig. 13(b), and is collected by the lens. All reflected rays travel to the back focal plane of the lens and are redirected towards the analyzer arm for polarization analysis.



(a)



(b)

Fig. 13: (a) ray picture of reflections in normal illumination configuration. (b) Polarizations of reflected rays in the back focal plane (reproduced from ref. 29).

Fig. 14 provides the coordinate system and the optical arrangement for calculating the signal at the detector, using Jones calculus. Assuming a randomly polarized light from a white light source, the incident field can be represented as

$$E_{in} = \begin{bmatrix} E_{ix} \\ E_{iy} \end{bmatrix}, \quad (62)$$

where  $E_{ix}$  and  $E_{iy}$  are the x- and y- component of the incoming beam's complex



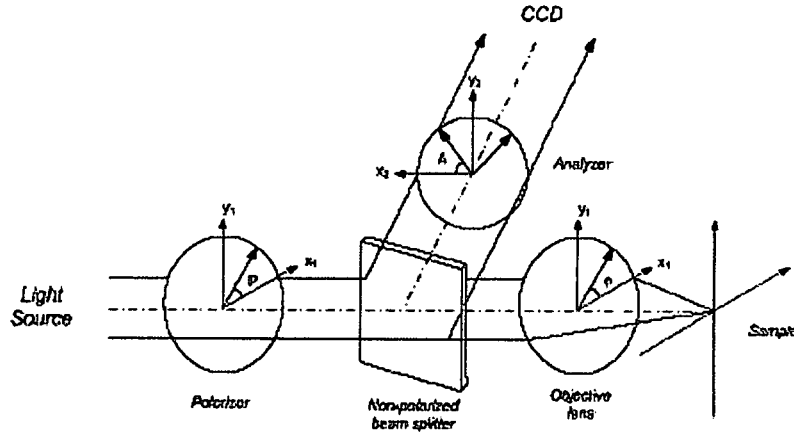


Fig. 14: Simplified diagram of the ellipsometer for signal derivation (reproduced from reference 29).

amplitude. The beam is linearly polarized using a linear polarizer whose Jones matrix representation is<sup>29</sup>

$$T_P = R(P) \begin{bmatrix} 1 & 0 \\ 0 & 0 \end{bmatrix} R(-P), \quad (63)$$

where  $P$  represents the angle between the polarizer's transmission axis and the laboratory's x-axis ( $x_1$ ), and  $R(P)$  represents the rotation matrix given by

$$R(P) = \begin{bmatrix} \cos(P) & \sin(P) \\ -\sin(P) & \cos(P) \end{bmatrix}. \quad (64)$$

Each incident ray in the pupil plan has a different azimuthal position. The difference in azimuthal positions is represented by a rotation operation<sup>29</sup>

$$R[-(\varphi + \pi)] \mathbf{f}_M, \quad (65)$$

where the argument  $\varphi + \pi$  is the azimuth of a reflected ray given an incident ray located at  $\varphi$ , and the matrix

$$T_M = \begin{pmatrix} 0 & 1 \\ 1 & 0 \end{pmatrix}, \quad (66)$$

represents the symmetric projection of a ray's polarization upon reflection. The reflection on the sample, assuming an isotropic sample, is represented by<sup>29</sup>

$$S(\theta) = \begin{pmatrix} R_p(\theta) & 0 \\ 0 & R_s(\theta) \end{pmatrix}, \quad (67)$$

where,  $R_s(\theta)$  and  $R_p(\theta)$  are the s- and p- reflection coefficients on the sample for an angle of incidence  $\theta$ . Finally, the reflected ray reaches the analyzer represented by

$$T_A = R(-A) \begin{bmatrix} 1 & 0 \\ 0 & 0 \end{bmatrix} R(A), \quad (68)$$

where  $A$  is the angle between the analyzer's transmission axis and the x-axis ( $x_2$ ) of the laboratory coordinate system.

After the analyzer, the electric field vector of a ray located at an azimuthal position  $\varphi$  in the exit pupil plane of the lens, and having an incident angle  $\theta$  is<sup>29</sup>

$$E_{out}(\varphi, \theta) = \begin{bmatrix} E_{0x} \\ E_{0y} \end{bmatrix} = T_A R[-(\varphi + \pi)] T_M S(\theta) R(\varphi) T_P E_{in}. \quad (69)$$

In Eq. (69), when  $P=A=0$ , then the polarizer and the analyzer transmission axes becomes parallel and the intensity at the detector can be obtained as follows<sup>29</sup>

$$\begin{aligned}
I(\varphi, \theta) &= |E_{out}(\varphi, \theta) * E_{out}^*(\varphi, \theta)| \\
&= \frac{1}{8} |E_{ix}|^2 |r_s|^2 (3 \tan^2 \Psi - 2 \tan \Psi \cos \Delta + 3) \\
&\quad \times \{1 + \alpha_2 \cos 2\varphi + \alpha_4 \cos 4\varphi\}.
\end{aligned} \tag{70}$$

The Fourier coefficients  $\alpha_2$  and  $\alpha_4$  are given by

$$\alpha_2 = \frac{4 \tan^2 \Psi - 4}{3 \tan^2 \Psi - 2 \tan \Psi \cos \Delta + 3}, \tag{71}$$

and

$$\alpha_4 = \frac{\tan^2 \Psi + 2 \tan \Psi \cos \Delta + 1}{3 \tan^2 \Psi - 2 \tan \Psi \cos \Delta + 3}, \tag{72}$$

respectively. The ellipsometric angles  $\Psi$  and  $\Delta$  are as defined in Eqs. (20) and (22).

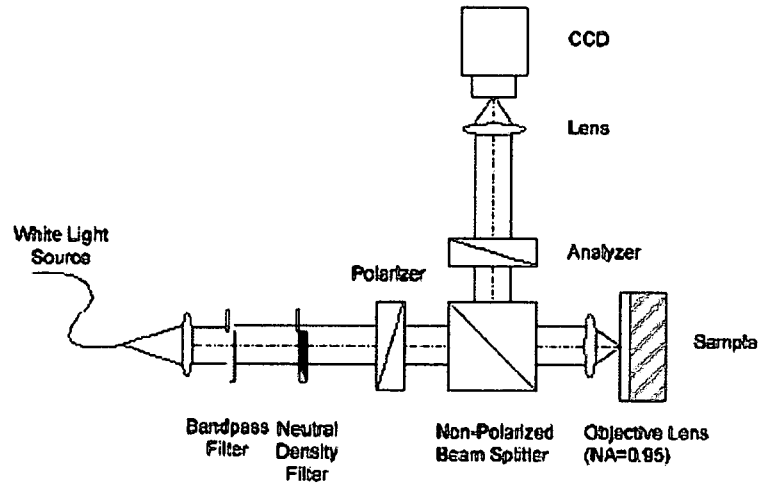


Fig. 15: Experimental setup of the ellipsometer  
(reproduced from ref. 29)

To obtain the total signal, Eq. (70) needs to be integrated over the pupil plane. From Eq. (70) it is clear that the signal is dependent on the azimuthal angle of a ray. This may result into a signal that is maximal at certain location in the pupil and minimal at others.

This nonuniformity of the signal over the pupil can result in a poor SNR. Also, without spatial filtering the back focal plane of the lens, the incident angle is not well defined and the instrument's sensitivity can be affected. The complete setup of the ellipsometer is shown in Fig. 15 where a bandpass filter is used for selection of a specific wavelength.

## **CHAPTER IV**

### **DESIGNING A HIGH SPATIAL RESOLUTION NULLING MICROELLIPSOMETER USING ROTATIONAL POLARIZATION SYMMETRY**

#### **A. Design Principles**

The issue of low lateral resolution in many ellipsometer designs was discussed at length in chapter 3. Focused beam ellipsometer designs with normal illumination configuration have been developed and have better lateral resolution. Despite the improvement in lateral resolution, low SNR is still a problem. The inhomogeneous distribution of the reflected beam's polarization in the pupil plane results in a low SNR when the signal is integrated over the entire pupil plane. In addition, multiple angles of incidence introduced by objective lens affect the sensitivity of the instrument. In order to improve the SNR while still maintaining a high ellipsometric sensitivity and high spatial resolution, a microellipsometer design utilizing rotational symmetry has been developed and demonstrated<sup>33</sup>. A rotationally symmetric polarization signal is achieved using the combination of circularly polarized illumination, a polarization rotator, and a radial analyzer. An annular aperture is used to perform back focal plane spatial filtering by selecting the signal generated from a narrow cone of illumination angle for high ellipsometric sensitivity. The SNR is improved by collecting the ellipsometric signal within an entire annular region, instead of a single position, due to the polarization signal

symmetry. The combination of high NA focusing and back focal plane polarization analysis yields a high spatial resolution. In this work, a mechanical motor was used to drive the polarization rotator, causing vibrational noise and limiting the modulation frequency of the polarization signal.

The microellipsometer design described in this chapter is a continuation of the previous radially symmetric ellipsometer work. In the current design, the mechanically driven polarization rotator is replaced with an Electro-Optic (EO) polarization rotator. The use of this EO polarization rotator eliminates the vibrational noise and enables higher modulation frequency for the polarization signal. Furthermore, it makes it possible to implement a nulling detection scheme that was proposed in Ref. (33).

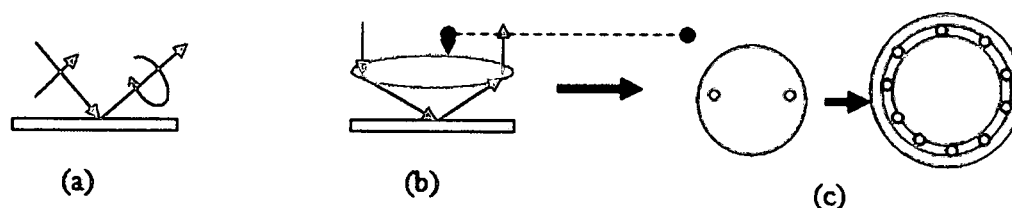


Fig. 16: (a) A conventional ellipsometer. (b) A single ray forms a single channel, equivalent to a conventional ellipsometer, by inserting a high NA lens in the path of the ray in (a). (c) Top view of the aperture plan showing a single channel, and multiple channels after replication.

A conventional ellipsometer using oblique illumination is shown in Fig. 16(a). A linearly polarized beam is incident on a sample and picks up an amount of amplitude and phase, upon reflection, and becomes elliptically polarized. If, instead of a beam, in Fig. 16(a) a ray was incident on the sample, inserting a high NA lens in the path of such a ray creates a normal illumination configuration shown in Fig. 16(b), and the ray becomes tightly focused into a small spot on the sample. This single ray (or channel) is

functionally equivalent to the conventional ellipsometer shown in Fig. 16(a). When the single channel is symmetrically replicated with respect to the optical axis of the lens, as shown in Fig. 16(c), multiple channels are generated, each one acting as a conventional ellipsometer. This polarization symmetry is not simply geometrical, but ellipsometric. Multiple channels, symmetrically arranged around the optical axis, form multiple channels, and each channel carries an *identically* polarized illumination.

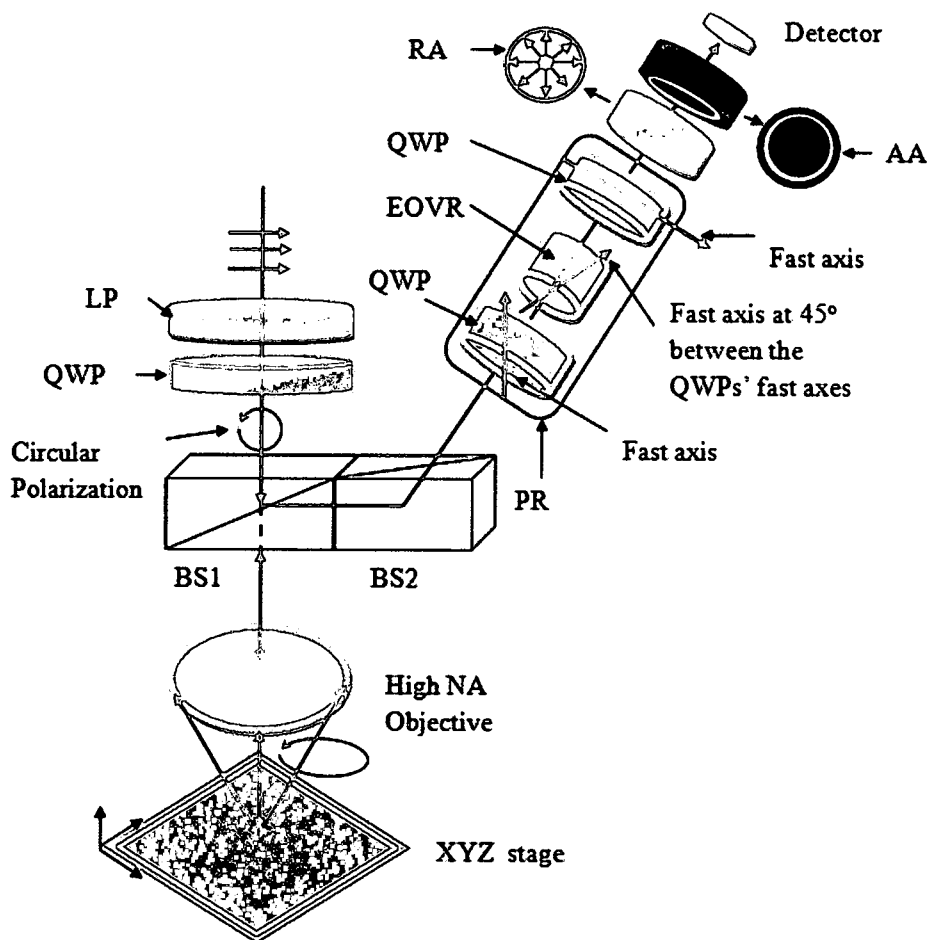


Figure 17: Conceptual diagram of radially symmetric microellipsometer design. BS1 and BS2 are two identical beam-splitters paired such that the s-polarization for the first beam-splitter (BS1) becomes the p-polarization for second beam-splitter (BS2) and vice-versa. PR: polarization rotator. EOVR: electro-optic variable retarder, RA: radial analyzer, AA: an annular aperture.

Fig. 17 shows a minimal ellipsometric configuration for the design concept of the microellipsometer discussed above. A linearly polarized beam is converted into a circularly polarized beam by properly aligning the linear polarizer (LP) and the quarter-wave plate. The angle between the polarizer and the QWP must be adjusted, taking into account the distortion caused by the first beam-splitter (BS1), such that the beam entering the objective lens is circularly polarized. At that point the polarization distortion caused by the imperfections in BS1 is compensated for. Symmetric channels of circularly polarized light illuminate the back focal plan of the objective, and each channel identically contributes to the total signal. This collaboration among individual channels significantly improves the overall signal-to-noise ratio of the system. The only difference among channels is a geometric phase due to the physical location of each channel in the objective's pupil. This phase is commonly known as Berry's phase<sup>34</sup> and does not affect the signal since the detector only responds to the signal power. A high N.A allows high angle illumination and focuses the circularly polarized beam down to a small spot on the sample, and collects the reflected light. The high angle illumination also gives a better ellipsometric signal level. The small spot size is the basis for spatial resolution improvement. The circular polarization incident on the sample picks up some amplitude and phase upon reflection, and generally becomes elliptically polarized. So far polarization symmetry is maintained. Two identical beam-splitters, BS1 and BS2, picked from the same coating run are used in this design for two purposes: beam steering and conservation of polarization symmetry. The first beam-splitter (BS1), just as most beam-splitters, has different responses to p- and s- polarizations. This difference in polarization responses causes a polarization distortion and ultimately destroys the polarization



symmetry. To remedy this polarization imbalance a second beam-splitter (BS2) that is identical to BS1 is inserted and positioned such that the s-polarization for the first beam-splitter becomes the p-polarization for the second beam-splitter and vice versa. This arrangement allows both s- and p- polarizations to be affected the same way and thus, the polarization symmetry is maintained as the beam is being directed towards the analyzer arm of the microellipsometer.

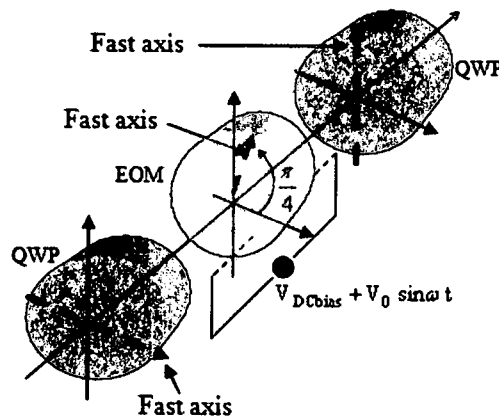


Figure 18: Diagram of the polarization rotator (PR).

The analyzer arm uses a pure polarization rotator (PR) consisting of two QWPs and an electro-optic variable retarder (EOVR) as shown in Fig. 18. The fast axes of the two QWPs are orthogonal and the fast axis of the EOVR is positioned at  $45^\circ$  between them. When configured as such, the transmission Jones matrix of the PR is a rotation matrix given by<sup>33</sup>

$$\begin{aligned}
T &= Q\left(\frac{\lambda}{4}\right)_{-\frac{\pi}{2}} P(\delta)_{\frac{\pi}{4}} Q\left(\frac{\lambda}{4}\right)_{\frac{\pi}{2}} \\
&= R\left(-\frac{\pi}{2}\right) \begin{pmatrix} 1 & 0 \\ 0 & -j \end{pmatrix} R\left(\frac{\pi}{2}\right) R\left(-\frac{\pi}{4}\right) \begin{pmatrix} 1 & 0 \\ 0 & \exp(-j\delta) \end{pmatrix} R\left(\frac{\pi}{4}\right) \begin{pmatrix} 1 & 0 \\ 0 & -j \end{pmatrix} \\
&= -j \exp\left(-j\frac{\delta}{2}\right) R\left(\frac{\delta}{2}\right),
\end{aligned} \tag{73}$$

where  $Q(\lambda/4)$  and  $P(\delta)$  are the Jones matrices of a QWP and the variable retarder, respectively. The subscripts  $(-\pi/2, \pi/4, \pi/2)$  indicate the orientation of the fast axes of the corresponding optical elements.  $R(\bullet)$  denotes the polarization rotation matrix for a given rotation angle. The retardation  $\delta$  depends on the voltage applied across the EO crystal and the illumination wavelength used according to

$$\delta = \frac{2\pi}{\lambda_0} n_0^3 r_{63} V, \tag{74}$$

where  $n_0$  and  $r_{63}$  are the ordinary refractive index and the electro-optic coefficient of the crystal, respectively. This device acts like a pure polarization rotator and the phase factor has no effect here since only the signal's power will be detected. It is important to note that this is a polarization rotation operation independent of the initial state of polarization and its orientation angle. The rotation angle is solely determined by the retardation generated by the EOVR which, in turn, depends on the applied voltage  $V$ .

For purpose of detection, the rotation angle produced by the dc voltage applied is modulated by a small angle produced by the high frequency ac voltage so that the total rotation angle (which is variable) at any time is the sum of the two contributions. The actual device used in this design can be modulated up to 1 MHz. This leads to higher

polarization rotation frequencies, a shorter integration time for lock-in detection, and faster scanning of samples. Most importantly, this device allows the implementation of the nulling technique in this design. The elliptical polarization generated by the circular polarization reflection on the sample enters the polarization rotator. The biasing action results in every ellipse of polarization in each channel to be locally rotated by the same amount proportionally to the applied voltage. As in the case of the PSRA ellipsometric arrangement described in chapter two, when these polarization ellipses are rotated such that one of their axes becomes parallel to the analyzer's transmission axis, a null of the first harmonic component will be observed in the detected signal.

#### **B. Mathematical Derivation of the Signal and the Nulling Detection Scheme**

The total signal on the detector can be derived using Jones calculus. The derivation is based on the geometric layout of the contributing channels in the pupil plane as shown in Fig. 19. In this diagram the illumination wave is a circularly polarized plane wave in the  $xOy$  coordinate system (this is the Laboratory coordinate system) and its Jones matrix is given by

$$E_{in} = \begin{pmatrix} 1 \\ j \end{pmatrix}. \quad (75)$$

Suppose a ray is entering the pupil at an azimuthal angle  $\varphi$ . This ray can be treated as a single channel. The coordinate system of this channel is  $x_iOy_i$  (this is the local coordinate system), as shown in Fig. 19. The two coordinate systems are chosen such that the two eigenvectors align with the s- and p- directions when the ray hits the sample. In the local coordinate system the incident polarization is given by

$$E_{loc} = R(\varphi)E_{in} = \begin{pmatrix} \cos \varphi & \sin \varphi \\ -\sin \varphi & \cos \varphi \end{pmatrix} \begin{pmatrix} 1 \\ j \end{pmatrix} = e^{j\varphi} \begin{pmatrix} 1 \\ j \end{pmatrix}. \quad (76)$$

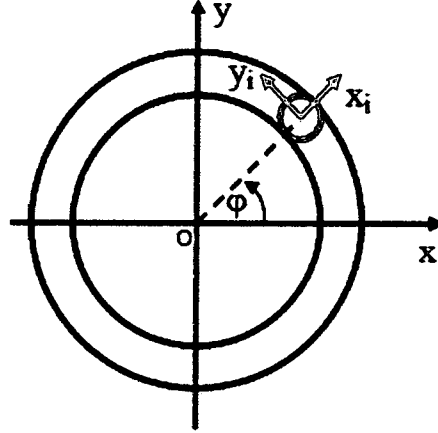


Figure 19: Coordinate system in the back focal plane of the objective.

Eq. (76) shows that each local channel sees an identical circularly polarized incident light except for a geometric phase. This phase, as explained earlier, does not affect the signal. After reflection on the sample, owing to the rotational symmetry, each channel carries an identical elliptical polarization signal except for the geometric phase. Suppose that in each local channel there is an ellipse of polarization with an ellipticity angle  $\epsilon$  and a major axis making an angle  $\theta_0$  with respect to the  $Ox_i$  axis. When the dc bias and the ac modulation voltages are applied across the modulator the ellipse of polarization in each channel is rotated by an angle

$$\Phi = \Phi_{bias} + \alpha_m \cos \omega t, \quad (77)$$

where  $\Phi_{bias}$  is the part of the rotation angle attributed to the dc bias voltage,  $\alpha_m$  is the amplitude of the modulation angle attributed to the ac voltage, and  $\omega$  is the modulation frequency. The general form of the signal is similar to that of a rotating analyzer ellipsometer.<sup>2</sup> In our case the general signal can be written as

$$P = K \left\{ 1 + \cos 2\varepsilon \cos[2(\Phi_{bias} + \alpha_m \cos \omega t + \theta_0)] \right\} \quad (78)$$

where  $K$  is a constant. Assuming a small angular modulation, i.e.  $\alpha_m \ll 1$  and using the Taylor's expansion, the cosine term in Eq. (78) can be expanded (see Appendix A) as

$$\begin{aligned} & \cos[2(\Phi_{bias} + \alpha_m \cos \omega t + \theta_0)] \\ & \cong \cos 2(\Phi_{bias} + \theta_0) (1 - \alpha_m^2 + \alpha_m^2 \cos 2\omega t) \\ & \quad - 2\alpha_m \sin 2(\Phi_{bias} + \theta_0) \cos \omega t. \end{aligned} \quad (79)$$

The substitution of Eq. (79) into Eq. (78) reveals three most relevant harmonic components in the general signal:

$$P(0) = K \left[ 1 + \cos 2\varepsilon (1 - \alpha_m^2) \cos 2(\Phi_{bias} + \theta_0) \right] \quad (80)$$

$$P(\omega) = 2K\alpha_m \cos 2\varepsilon \sin 2(\Phi_{bias} + \theta_0) \cos(\omega t + \pi), \quad (81)$$

$$P(2\omega) = K \cos 2\varepsilon \alpha_m^2 \cos 2(\Phi_{bias} + \theta_0) \cos(2\omega t + \pi). \quad (82)$$

Eqs. (80) – (82) are the dc, first, and second harmonics of the signal, and they are similar to the harmonic components of the Monin-Boutry ellipsometer's signal given by Eqs. (57) - (59). Signal components in Eqs. (80) – (82) depend on the ellipticity angle  $\varepsilon$ , the modulation amplitude  $\alpha_m$ , and the ellipse orientation angle  $\theta_0$ , among other

parameters. It can be deduced from equation (81) that when  $\Phi_{bias} = -\theta_0$  or  $\Phi_{bias} = -\theta_0 \pm \pi/2$  the first harmonic becomes *null*, i.e.  $P(\omega) = 0$ , hence, the nulling detection scheme. The ratio of the dc signal at two consecutive null positions, i.e.  $\Phi_{bias} = -\theta_0$  and  $\Phi_{bias} = -\theta_0 \pm \pi/2$ , gives  $\tan^2 \varepsilon$ . This means that by measuring two consecutive nulls one can determine both the elevation angle  $\theta_0$  and the ellipticity angle  $\varepsilon$ . Once the pair  $(\varepsilon, \theta_0)$  is known, the ellipsometric pair  $(\Psi, \Delta)$  can in turn be determined using the following formulas<sup>3</sup>

$$\cos(2\Psi) = -\cos(2\varepsilon)\cos(2\theta_0), \quad (83)$$

$$\tan(\Delta) = \frac{\tan(2\varepsilon)}{\sin(2\theta_0)}. \quad (84)$$

With  $\Psi$  and  $\Delta$  measured at one or more positions on the sample along with an optical model of the sample, a regression algorithm can then be applied to retrieve the thickness and refractive index of the sample.

Simulations of the dc and first harmonic of the signals were performed in order to have an idea on the signals behavior under different polarization scenarios. Eqs. (80) and (81) were used to generate the amplitude graphs in Figs. 20 and 21. Fig. 20 shows the dc signal amplitude as a function of the phase retardation induced by the bias voltage applied across the crystal in the EO modulator. Circular and quasi-circular polarizations result into a dc signal with a poor modulation depth while the linear and elliptical polarizations result into a dc signal with a good modulation depth. Figs. 21(a) - (d) show

the amplitude of the first harmonic signal under various dc biasing conditions, polarization orientation, ellipticity angles. In the simulation  $\Phi_b$  is the dc-voltage induced

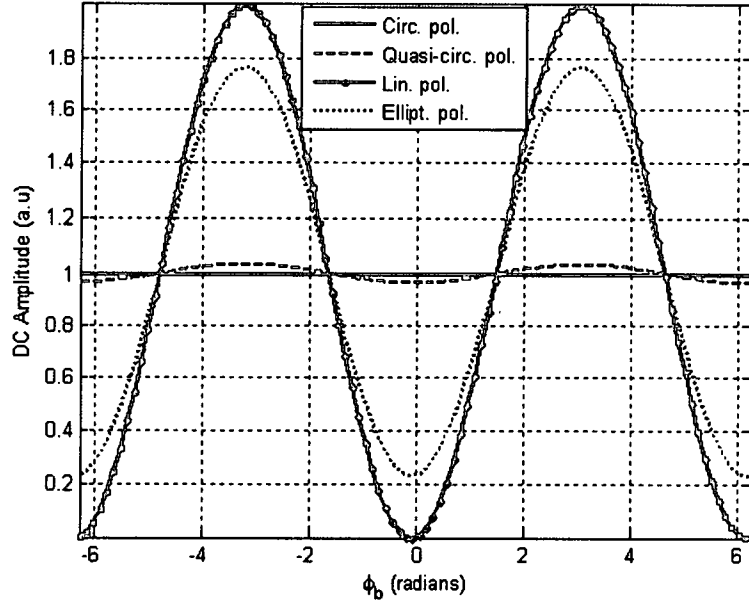


Fig. 20: Simulation of the dc signal amplitude vs. bias voltage-induced retardation phase under different polarizations.

retardation phase and, therefore, indirectly represents the dc voltage bias itself.  $\epsilon$  and  $\theta_o$  are the ellipticity angle and the angular orientation of the polarization ellipse, respectively. By adjusting these parameters, different behaviors of the signal were observed in the time domain. In general, the modulation depth in the signal was observed to be strongly dependent on the polarization. Of all the polarizations tested linear polarization produced the biggest modulation depth. In practice, the incident beam has to pick up enough amplitude and phase on reflection in order for the signal to have a good modulation depth.

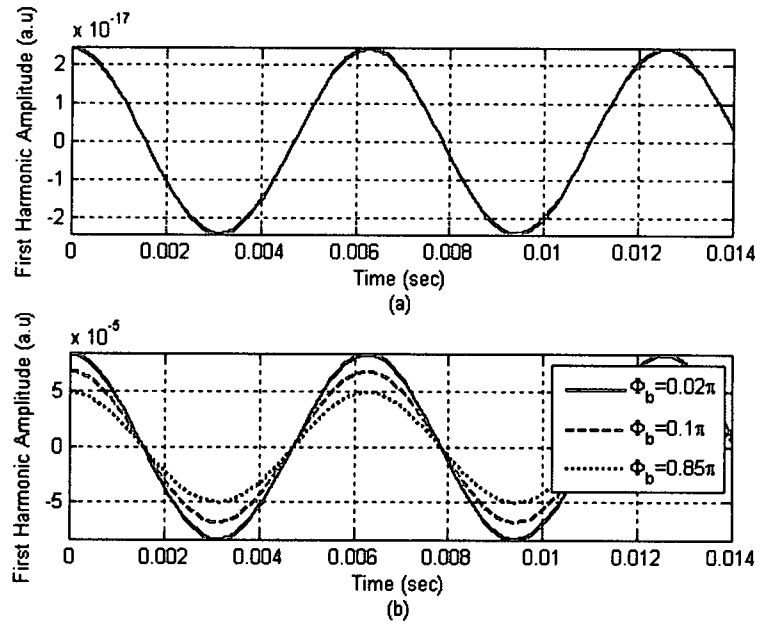


Fig. 21: First harmonic signal for (a) a circularly polarized beam, (b) a quasi-circularly polarized beam.

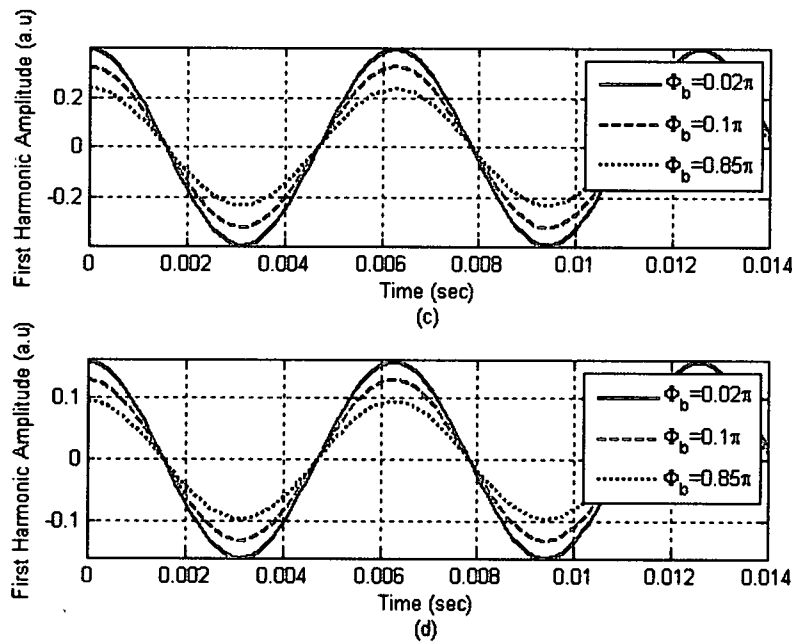


Fig. 21: First harmonic signal for (c) a linearly polarized beam, (d) an elliptically polarized beam.



Fig. 21(a) shows that the amplitude of the first harmonic signal is zero for circular polarization. In this case a zero or almost zero amplitude signal is expected due to zero modulation depth resulting from circularly polarized light ( $\epsilon = 45^\circ$ ). This means that if the sample does not induce a substantial phase in the reflected beam, the ellipsometric signal will have a poor modulation depth. For the case of quasi-circular polarization shown in figure 21(b) the signal's modulation depth is still almost zero, although bigger than that in Fig. 21(a). The modulation is improved when linear and elliptical polarizations are assumed as shown in figures 21(c) and (d).

### C. INSTRUMENTATION

The hardware schematic of the microellipsometer is shown in Fig. 22. The beam goes through the intermediary optical elements for spatial filtering and collimation, and ends up focused by the objective lens (Nikon LU Plan, 100x, NA=0.9) on the sample. The sample is placed on a computer-controlled XYZ translation stage (Newport controller, ESA-C) through a GPIB interface (IEEE 488.2). The reflected polarization is collected by the objective lens and redirected toward the analyzer arm by a beam-splitter pair, before entering the polarization rotator. The EOVR (modulator) (ConOptic 370 LA) in the polarization rotator is biased by a range of amplified (100X) voltages (-350 volts to 350 volts) supplied by a function generator (Agilent, 33220A) and amplified by a high voltage amplifier (Matsusada, AMS 1B30). A small ac voltage (20 mV, 1 KHz) is supplied by the same function generator for signal modulation. The beam leaving the polarization rotator goes through a radial analyzer (RA), and then through an annular aperture (AA) for spatial filtering of the central portion of the beam attributed to low angles of illumination. After spatial filtering the beam is focused on the photodetector

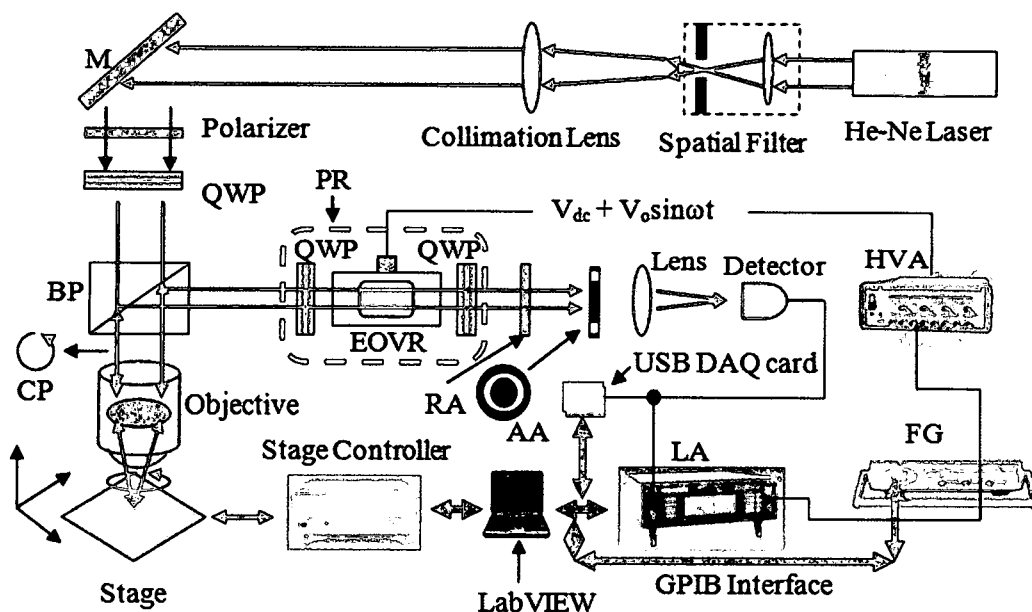


Fig. 22: Complete laboratory setup of the microellipsometer. The lock-in amplifier (LA) takes the signal and its reference in from the detector and a function generator (FG). The high voltage amplifier (HVA) amplifies (x100) the dc bias voltage supplied by the FG. BS is a beam-splitter pair formed by pairing two identical beam-splitters BS1 and BS2 (see Fig. 16) such that the s-polarization for the first beam-splitter (BS1) becomes the p-polarization for second beam-splitter (BS2) and vice-versa. M: mirror, USB DAQ: USB data acquisition card.

(Thorlabs, DET 210). The output of the detector is split into two parts. One part is sent to a lock-in amplifier (Signal Recovery 725) for the detection of the first harmonic signal. The other part of the detector's output is sent to a USB-connected data acquisition card (DAQ, USB-1288FS). The temporal signal acquired with the DAQ card is pre-processed via low-pass filtering to get rid of the high frequency noise, and Fourier transformed to retrieve the dc signal. A LabVIEW program via a GPIB interface controls the function generator, the translation stage, the lock-in amplifier, and the DAQ card.

Taking measurements with the microellipsometer consist of a repetitive sequential execution of specific tasks assigned to specific equipments in the microellipsometer. To

scan a sample the ellipsometer must sequentially execute the following tasks in the given order:

1. Move the sample to a spot (starting location on the sample). This is achieved by applying appropriate voltages to the stage controller's x- and y- axes' ports.
2. On that particular location, scan the entire dc bias range. This is the role of the function generator and the high voltage amplifier.
3. For every dc bias point in the bias voltage range, record the amplitudes of the first harmonic and dc components of the signal.
4. Analyze the data to locate at least two minima in the first harmonic component and find the two corresponding bias voltages. Using the first bias voltage and the rotation coefficient of the modulator,  $\theta_0$  and is determined. Also, the locations of the two minima in the first harmonic component can be mapped to the dc component to determine two corresponding voltages whose ratio yields the value of  $\varepsilon$  on the location of the sample being scanned.
5. Move the stage to the next spot on the sample and repeat steps 1 - 4.

The tasks in step 4 are performed internally by the software (LabVIEW) which also displays the results and store the data into files.

The ellipsometer's hardware components are controlled by LabVIEW's virtual instruments (VIs). A VI is a hardware driver (software) that provides hardware control access to the user. In our case the function generator, lock-in amplifier, DAQ card, and the stage controller had preexisting VIs available for use on National Instruments (NI) website. Our task was to integrate these VIs into a single VI with input control parameters and output displays on the front panel of the graphical user interface. The task

was achieved after several modifications. The software has three loops that handle the main tasks of the instruments. The two outer loops incrementally adjust the voltages on x- and y- control ports of the stage controller in order to translate the sample in the x- and y- directions for 2-D scanning tasks. The number of iterations assigned to these loops determines the number of spots that are scanned in x- and y- directions. The step distances of the translations as well as the number of iterations can be defined on the front panel of the graphical user interface. Once the two outer loops position the sample, the third loop, which is in charge of scanning the dc bias range, starts executing. The number of iterations assigned to the third loop determines the number of dc bias points and the step bias voltage in the bias voltage range. The third loop is also in charge of reading the amplitudes of the dc and first harmonic signals for every bias point. An algorithm developed to process the amplitude data is embedded within the third loop.

#### C1. Circular Polarization Generation

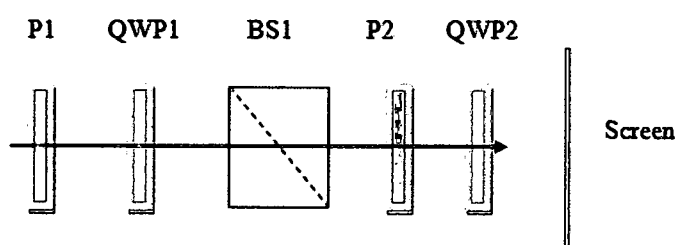


Fig. 23: Alignment diagram for circular polarization generation.

The beam coming out of the Helium-Neon (He-Ne) laser is linearly polarized. A Linear polarizer and a QWP are used to generate a circularly polarized beam necessary for the generation of the ellipsometric signal. The transmission axis of the polarizer and the fast axis of the QWP must be angularly separated by  $45^\circ$  in order to for the output beam to be

circularly polarized. As mentioned earlier, this alignment must be done with BS1 put in place in order to account for its polarization distortion effect. Fig. 23 shows the optical alignment diagram, and the alignment is done following these steps:

1. The first polarizer (P1) and the second polarizer (P2) are inserted and one of them is rotated until a null is obtained. At this point P1 and P2 transmission axes are orthogonal.
2. The first quarter-wave plate (QWP1) is inserted and rotated until a null is seen on the screen. At this point the fast axis of this plate is parallel to the transmission axis of one of the polarizer. From the null position QWP1 is rotated by 45 degrees clockwise or counter-clockwise.
3. The second quarter-wave plate (QWP2) is inserted and rotated until a null is seen on the screen. At this point the light coming out of the beam splitter is quasi-circular due to a small ellipticity that the beam splitter introduces. QWP1 can then be adjusted to compensate for this ellipticity until the light that comes out of the beam splitter is almost perfectly circularly polarized. At that point there will be zero or almost zero intensity on the screen because P2 and QWP2 form a circular polarizer that cancels out the circular polarization coming out of the beam splitter. After calibration P2 and QWP2 are removed.

## **C2. Polarization Rotator Alignment and Calibration**

The calibration of the polarization rotator was performed in order to find its rotation coefficient. But, before calibration, the polarization rotator alignment shown in Fig. 24 was done using the following steps:

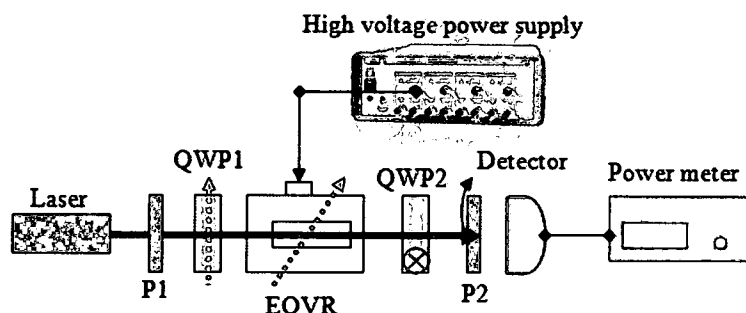


Fig. 24: Polarization rotator alignment and calibration diagram.

1. Insert P1 and P2 and rotate either one of them so that their fast axes are orthogonal (a null must be detected).
2. Place QWP1 between P1 and P2, but close to P1 and rotate QWP1 until a null is detected. At this point the fast axis of QW1 is parallel to the fast axis of either P1 or P2.
3. Place QWP2 after P1, but close to P2, and rotated QWP2 until a null is detected. At this point the fast axes of the two QWPs are orthogonal. This can be verified by checking that the position markers of the fast axes on both QWP1 and QWP2 are  $90^\circ$  apart.
4. Place the modulator (EOVR) between the two QWP1 and QWP2, and apply a voltage, e.g. 50 volts, to it. The modulator must then be rotated in either directional until a null is detected. At this point the modulator's fast axis is parallel to the fast axis of one of the QWPs.
5. To place the modulator's fast axis at  $45^\circ$  with respect to each of the QWPs fast axis, both QWPs must be simultaneously rotated by  $45^\circ$  in the same direction. This step completes the alignment of the polarization rotator. The two QWPs and

the EO modulator, now, form a single device that functions as a polarization rotator.

The polarization rotator is calibrated by applying a certain range of dc voltages across the modulator, and for each applied voltage the linear analyzer (P2) is rotated until a null is detected. The angle at which the null occurs is then recorded. For this work a range of dc bias voltages going from -700 volts to +700 volts was used. The resulting calibration curve was obtained and is shown in Fig. 25. The equation of line is

$$\theta = 0.248V + 121.42, \quad (85)$$

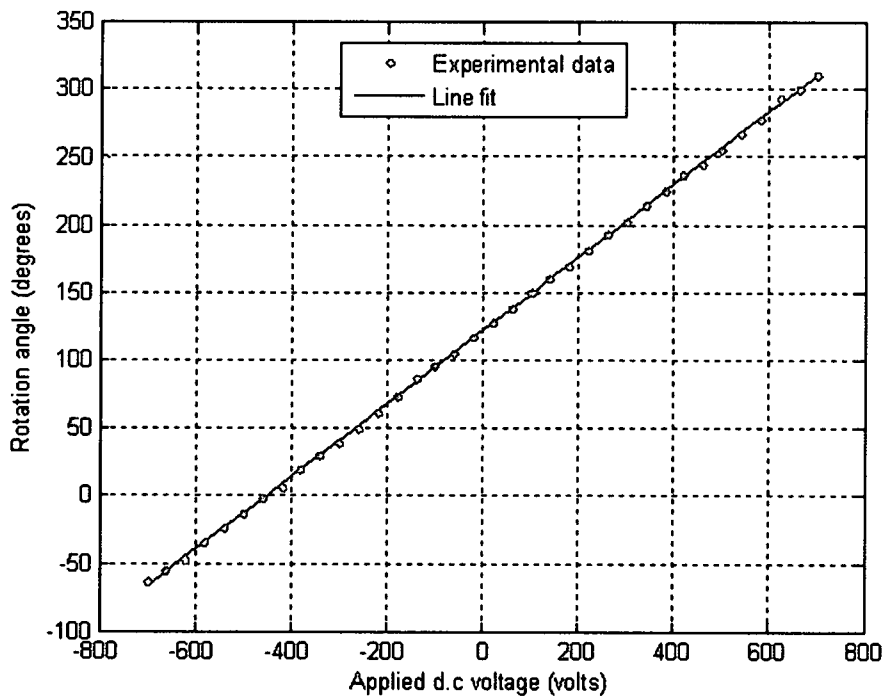


Fig. 25: Polarization rotator calibration curve for a bias range of  $\pm 700$  volts. The rotation coefficient of the polarization rotator was found to be  $0.248^\circ/\text{volt}$ .

where  $\theta$  is the rotation angle resulting from a voltage  $V$  applied across the modulator. The rotation coefficient determined from the equation is 0.248 degree/volt. This value can vary significantly depending on how good the system alignment is. Therefore, the alignment should be carefully done if one is to expect an accurate calibration. Note that the fitting line does not go through the (0,0) coordinate, meaning that there is a small residual birefringence due to the crystal.

#### **D. Signal Testing**

After the polarization rotator was calibrated and the system was aligned, the microellipsometer signal was tested using a flat dielectric mirror in lieu of a sample. The signal was tested to confirm presence of a second harmonic component. Fig. 26 shows a 1 KHz ac modulation voltage signal (top) and the 2 KHz detected second harmonic signal (bottom). First, the first harmonic signal (not shown in Fig. 26) was detected, and then

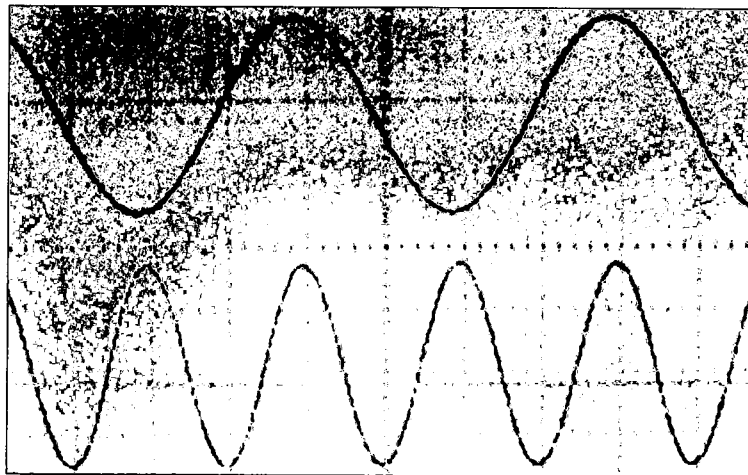


Fig. 26: (top) ac modulation voltage signal (1 KHz), (bottom) detected second harmonic signal (2 KHz) under linear polarization illumination.



the dc bias voltage on the modulator was manually gradually changed until the second harmonic was obtained. Since the incident beam is linearly polarized, the second harmonic shows a good modulation depth although the mirror is not a source of a substantial amount of ellipticity.

When a sample does not induce a significant amount of phase in the reflected beam, the first harmonic, in general, will have a small modulation depth when circular polarization is used for illumination. In this case the second harmonic will have an even smaller modulation depth. The signal was tested using a 100 nm  $\text{SiO}_2$  thin film deposited on a silicon substrate with sputtering machine (Denton Vacuum Explorer 14). Fig. 27 shows the detected first and second harmonic signals under circular polarization illumination. The first harmonic has a good modulation depth because the  $\text{SiO}_2$  film is

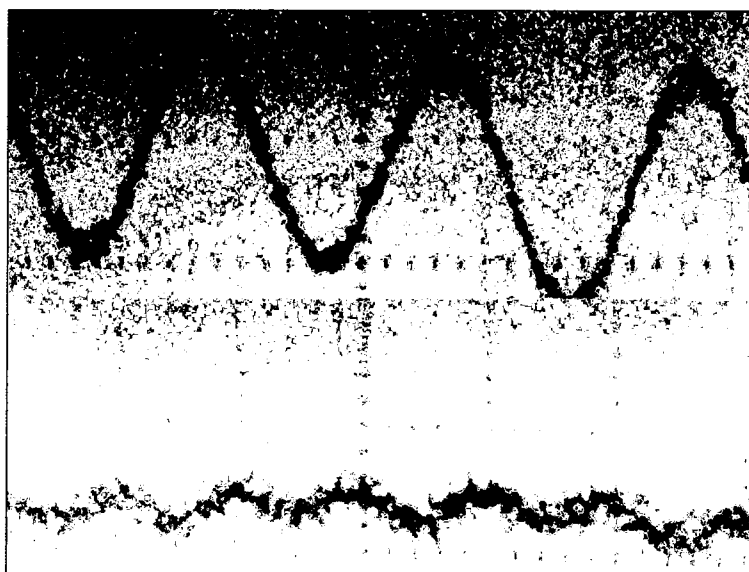


Fig. 27: Detected first harmonic (1 KHz, top) and second harmonic (2 KHz, bottom) signals under circular polarization illumination.

thick enough to induce a significant amount of phase in the reflected beam. The second harmonic signal has a small modulation depth as expected under circular polarization illumination. The signals shown in Fig. 27 were captured with a radial polarizer.

In both Figs. 26 and 27, the second harmonic signal is detected when the first harmonic has been nulled. When a dc bias voltage range, e.g.  $\pm 700$  V, is scanned the amplitude of the first harmonic signal varies between minima and maxima, with the minima (ideally zero amplitude) corresponding to the nulling points, i.e. second harmonic appearances. But, to measure the two ellipsometric angles ( $\psi, \Delta$ ) only two null positions are needed. For testing purpose, a  $\text{SiO}_2$  thin film deposited, by sputtering (Denton Vacuum Explorer 14), on a silicon substrate was used under circular polarization illumination.

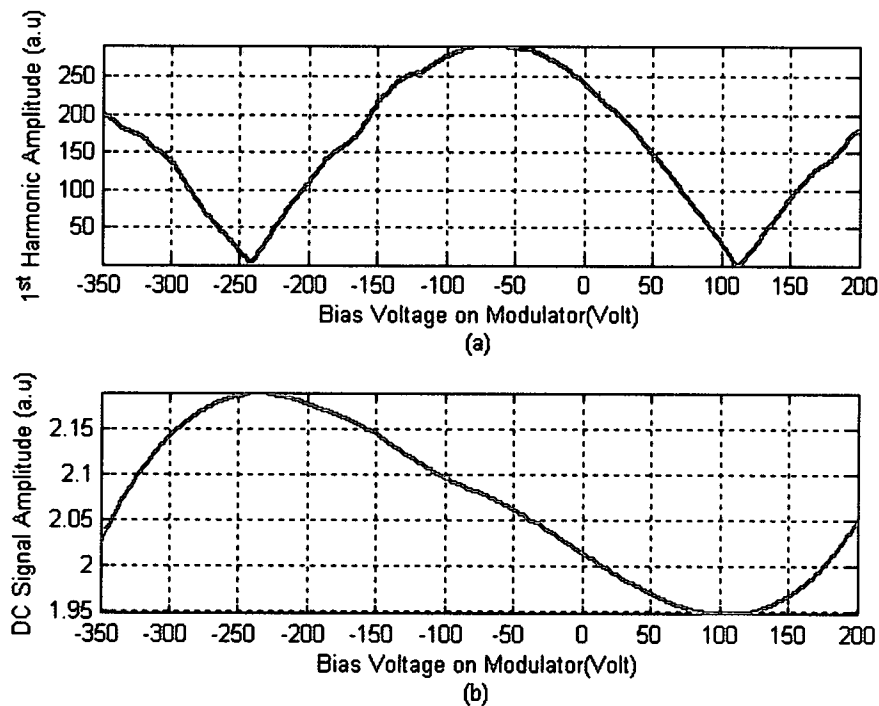


Fig. 28: First harmonic signal (a) and dc signal (b) vs. dc bias voltage. Two null points in the first harmonic can be clearly identified.

Fig. 28 shows the amplitudes of the first harmonic signal (a) and dc signal (b) as a function of dc bias voltage (-350 V to 200 V), using a step voltage of 2 volts. Given the polarization rotator coefficient ( $0.248^\circ/\text{V}$ ), the two null locations in the first harmonic signal are separated by 362 volts, corresponding to an angular separation of  $89.8^\circ$ . This value is very close to the ideal value of  $90^\circ$  predicted by Eq. (81). Note that the minimum-maximum amplitude contrast is bigger for the first harmonic signal than it is for the dc signal.

## CHAPTER V

### EXPERIMENTAL MEASUREMENTS

#### A. Results

Before taking any measurement, a SiO<sub>2</sub> thin film deposited on a silicon substrate via sputtering (Denton Vacuum Explorer 14), is scanned to check for the validity of the signal. For such a uniformly thick sample, the spatial trajectories of the two minima are expected to be mostly linear and horizontal, except for some noise or vibration related variations. Moreover, the separation between the two minima must remain constant. When a sample is not uniformly thick the trajectories are not linear and horizontal everywhere, but the separation between the two minima must always be constant. Figs. 29(a) and 29(b) show a typical scan describing the spatial evolution of the minima, and the repeatability test measurement, respectively. The sample thickness is 100 nm, and the scans were taken using a 0.1  $\mu\text{m}$  step scanning distance. The stability of the signal was qualified and quantified using the RMS error associated with the variation in the location of the minima. The RMS errors in Fig. 29(a) and 29(b) are calculated to be 6.1 volts or 1.5° and 6.67 volts or 1.65°, respectively. The level of error is tolerable and therefore the signal is valid.

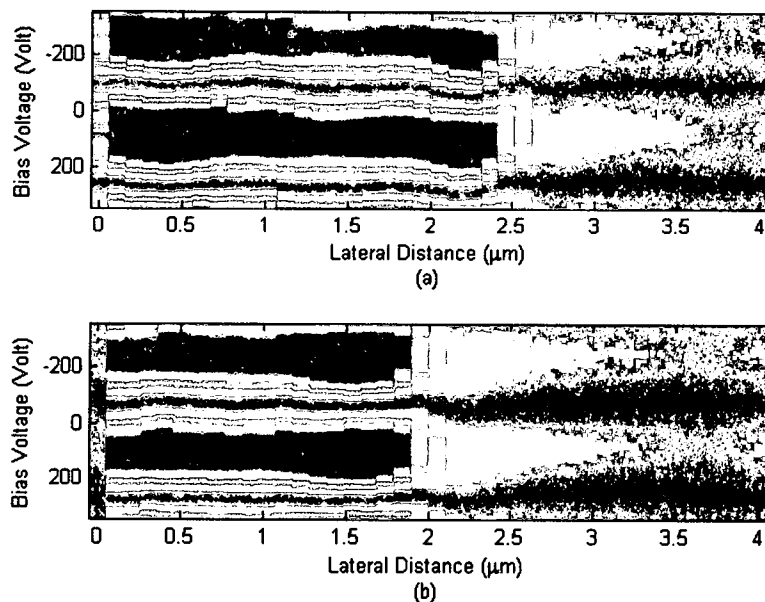


Fig. 29: (a) Spatial evolution of minima in the first harmonic signal for testing signal stability and validity before any measurements are taken. (b) Repeatability test.

The first set of measurements consists of five  $\text{SiO}_2/\text{Si}$  samples of different thicknesses. The  $\text{SiO}_2$  thin films were deposited on silicon substrates via sputtering (Denton Vacuum Explorer 14), and characterized using a spectroscopic ellipsometer (Angstrom PHE 102) in the 300 nm - 900 nm wavelength spectrum. Table 1 shows the measured thicknesses and refractive indices for the 633 nm wavelength. Fig. 30 shows an exemplar of the results of fitting the optical model to the experimental measurements of (a)  $\Psi$  and (b)  $\Delta$  for the 51.17 nm sample in the 300 nm – 900 nm spectrum. Fig. 30(c) is the calculated refractive index for the same spectrum.

	Thickness (nm)	Refractive index
Sample 1	28.9	1.56 (MSE = 0.01)
Sample 2	43.83	1.52 (MSE = 0.01)
Sample 3	49.55	1.502 (MSE = 0.01)
Sample 4	51.17	1.508 (MSE = 0.01)
Sample 5	73.78	1.49 (MSE = 0.04)

Table 1: Thicknesses and refractive indices (at  $\lambda=6333$  nm) of five  $\text{SiO}_2/\text{Si}$  samples measured with a spectroscopic ellipsometer (Angstrom PHE 102).

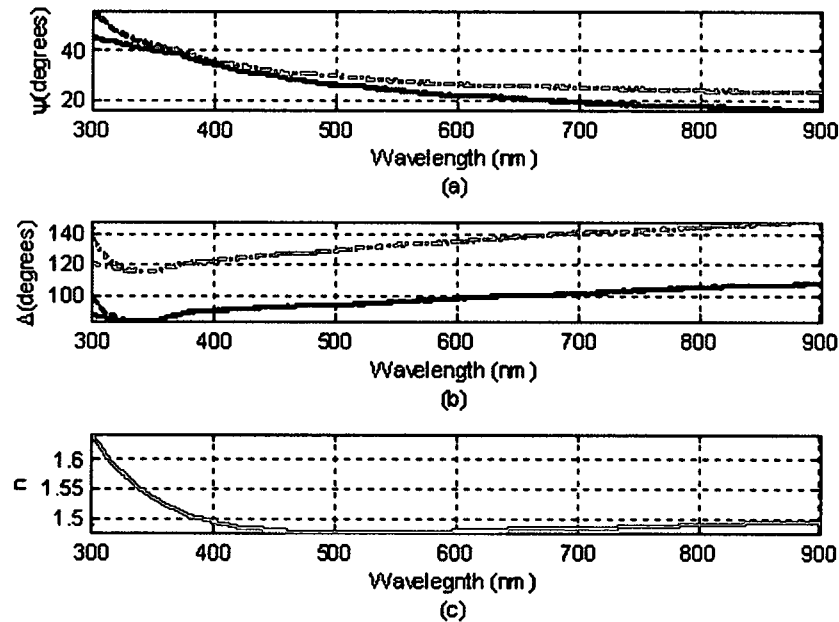


Fig. 30: Fitting results for (a)  $\Psi$  and (b)  $\Delta$ . The dotted-blue and the dot-dash red lines are results associated with  $60^\circ$  incident angle, and the dashed and solid black lines are results associated with the  $70^\circ$  angle of incidence. Fig. 30(c) is the calculated refractive index for the  $60^\circ$  incident angle.

The five samples were then measured with our microellipsometer and the first harmonic signal was obtained for each sample. Since the dc signal was not available for lack of a better dc signal detection system, the ellipsometric angle  $\epsilon$  could not be measured, and consequently, the pair  $(\Psi, \Delta)$  could not be determined. Instead, the bias dc (rotation) voltage corresponding to the first minimum of the first harmonic signal was measured, for each sample, and an optical model was constructed and fit to the measured rotation voltage. The measured thicknesses given in Table 1 were used as starting guesses in the Levenberg-Marquardt regression algorithm. The refractive index and the thickness were used as fitting variables of the optical model in the regression algorithm. Since the model was fit to rotation voltage data, the merit function in Eq. (36) was changed accordingly. The average angle of incidence was calculated (see Appendix B) using the annular aperture size and found to be  $58.5^\circ$ . Fig. 31 shows the result of the fitting procedure. This result shows that our system is sensitive enough to detect small changes in thickness (see data points 2, 3, and 4) within an acceptable margin of error. The fitting errors are attributed on the most part to the experimental measurement errors. For rotation voltages corresponding to the first minima of the first harmonic signal, an average experimental error of 5.4 volts, corresponding to an angular rotation of  $1.34^\circ$ , for all samples was calculated and used in the fitting model. For smaller thicknesses fitting errors can get bigger due to the fact that a small change in thickness can result in a wide change in the value of  $\Psi$  (see Fig. 5) or rotation voltage in this case. Fig. 32 show the refractive indices of the five samples as obtained from the spectroscopic ellipsometer measurements and the microellipsometer measurements. The refractive index is ideally expected to remain constant as the thickness of the film varies. But, with thickness

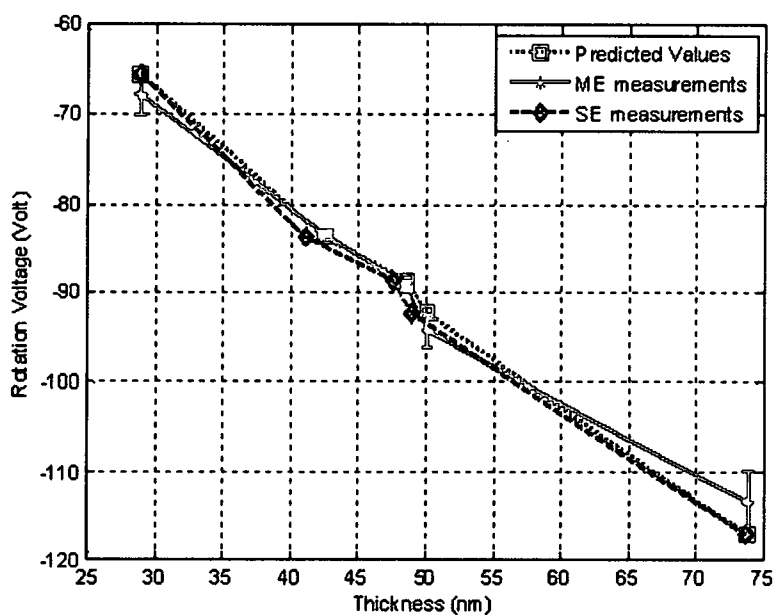


Fig. 31: Fitting result: experimental and analytical rotation voltages for 5  $\text{SiO}_2/\text{Si}$  samples. SE: measurements taken by the spectroscopic ellipsometer (Angstrom, PHE 102), ME: measurements taken by the microellipsometer.

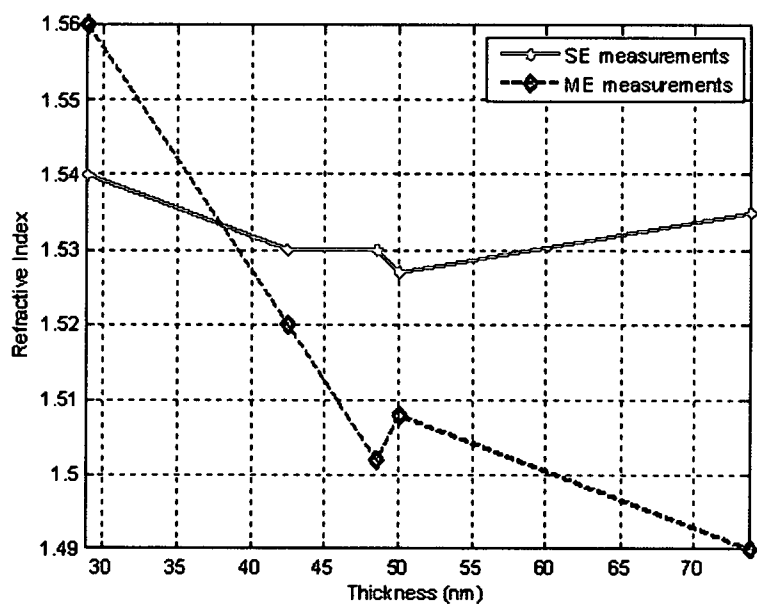


Fig. 32: Refractive indices measurements of  $\text{SiO}_2$  samples. SE: measurements taken by the spectroscopic ellipsometer (Angstrom, PHE 102), ME: measurements taken by the microellipsometer.



change there are variations of refractive index in both spectroscopic ellipsometer and microellipsometer measurements in Fig. 32. These variations are more pronounced in the spectroscopic ellipsometer measurements than they are in the microellipsometer measurements. In both cases, the variations are the result from experimental errors, but the values of the refractive index are close to the values quoted in scientific literatures for the 633 nm wavelength.

The tests conducted so far are for individual samples each with a uniform thickness. To be able to test the surface profiling capability of the microellipsometer, a micro prism from a grating sample was scanned and the rotation voltage corresponding to the first minima of the first harmonic signal were measured. The sample is a 1-D surface relief blazed grating, made of photoresist (Microchem S1813) and fabricated on a silicon substrate by photolithography. Each period of the blazed grating is a micro prism. By the time of this experiment the sample was not characterized a priori to determine its thickness profile and index of refraction. But, it has been characterized recently with an atomic force microscope (AFM) (PSIA XE-100) and the period of the grating, as shown in Fig. 33, was determined to be 20  $\mu\text{m}$  long. As in the previous experiments, the dc signal detection system was not operational yet, therefore, the experimental data consist of the rotation voltage for each scanned location along the micro prism ramp. The optical model was constructed and fitted to the measured rotation voltages. In the fitting process, several thickness (slope) profiles were generated and used in our analytical model in order to obtain an initial guess of the thickness profile. The thickness profile with the smallest MSE error was then used for data fitting, with the optical model being fitted to each measured rotation voltage point individually, in order to optimize the thickness

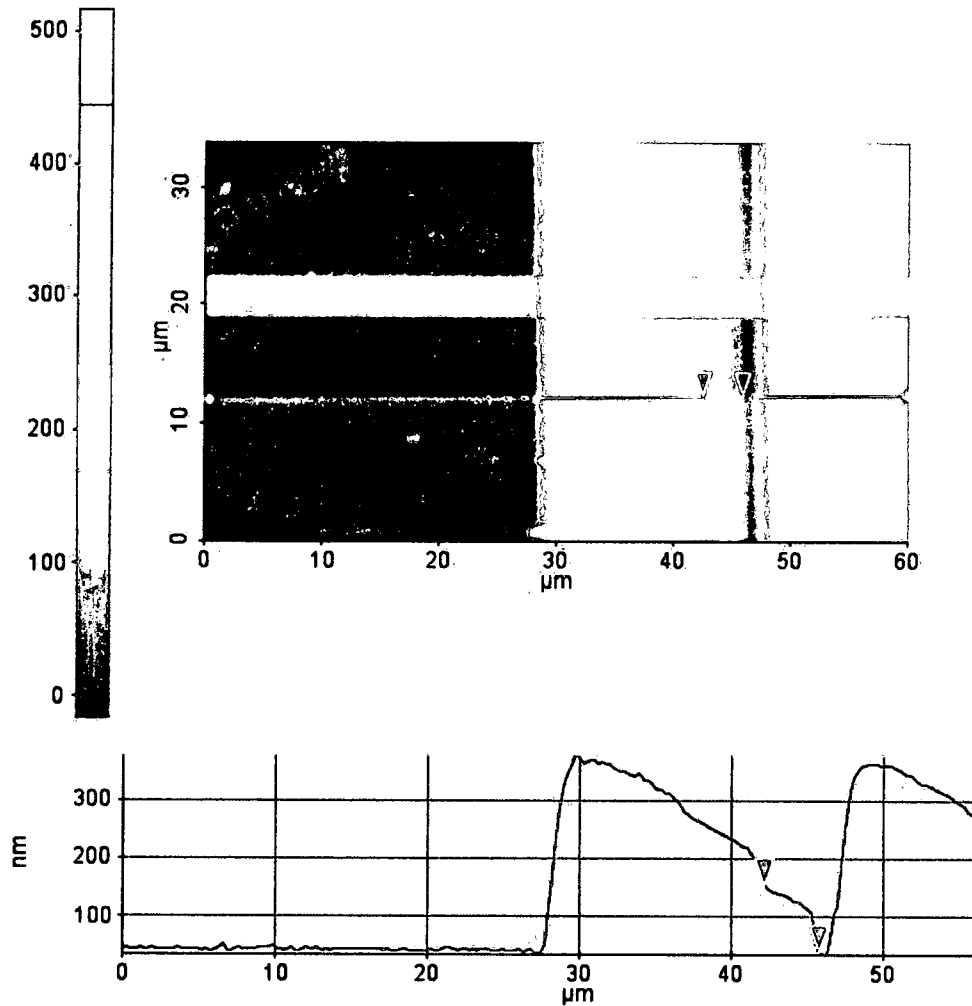


Fig 33: AFM scan of micro prisms that form the grating sample.  
A line scan of the micro prism profile is shown at the bottom.

profile. Both the thickness and index of refraction were used as fitting variables in the optical model. Two sets of measurements were taken: red dots and blue crosses in Fig. 34(a). The two sets of data in Fig. 34(a) are close together; this shows that the instrument is capable of taking repeatable measurements. The analytical model closely fits the experimental data, except at the locations of the two sharp discontinuities. The two discontinuities are due to phase wrapping on locations where the accumulated phase is  $2n\pi$ , (with  $n = 1, 2, 3$ , etc). The fitting errors are a combination of measurements errors due the loss of collimation in the beam and the high sensitivity of the optical model to

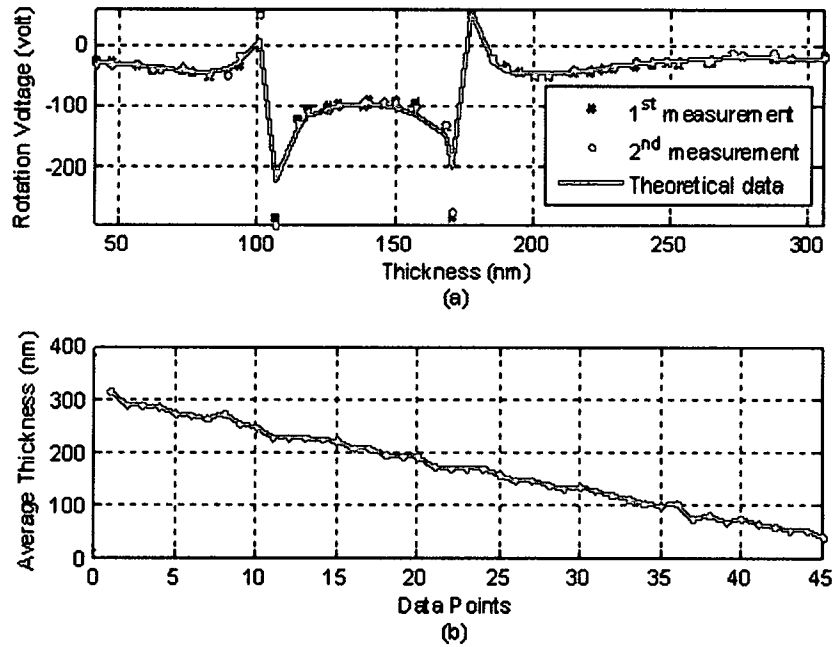


Fig. 34: Rotation voltage fitting result (a), with the second measurement as repeatability test. The corresponding thickness profile is shown in (b).

less precise parameters such as angle of incidence, polarization compensation in the high NA objective, etc. The collimation of the beam was checked at the beginning and the end of each scan, and it was found that there was loss of collimation toward the end of the scans due to the instability of the translation stage z-axis. The loss of collimation results into a defocused polarization signal and a shift in the locations of the rotation voltages. The corresponding thickness profile is shown in Fig. 34(b). It can be seen that, in general, the thickness profile is continuously varying showing the ability of the microellipsometer to detect continuous change in thickness. However, Fig. 33 shows that the profile is not continuously linear. There are sections of the profile that have different slopes. The microellipsometer could not detect these changes in the slope because the optical model, based on rotation voltage, is not as sensitive as a model based on more sensitive

parameters such as  $\Psi$  and  $\Delta$  which can be obtained only when both the first harmonic and dc signals are available. The refractive index was calculated and found to be 1.496.

After interfacing a DAQ card to the computer for dc signal detection, the grating sample shown in Fig. 33 was used again to scan the micro prism. The measurements consist of two 13  $\mu\text{m}$  long scans across a micro prism, using a lateral scanning step distance of 100 nm and a step bias voltage of 2 volts. Figs. 35 (a) and 35(b) show the amplitudes of the dc and first harmonic signals vs. bias voltage and lateral distance, resulting from the first 13  $\mu\text{m}$  long scans. The amplitude data sets from the two scans were first converted in terms of  $(\Psi, \Delta)$  and an optical model was constructed. Using the fitting strategy described earlier, several thickness profiles with different slopes were

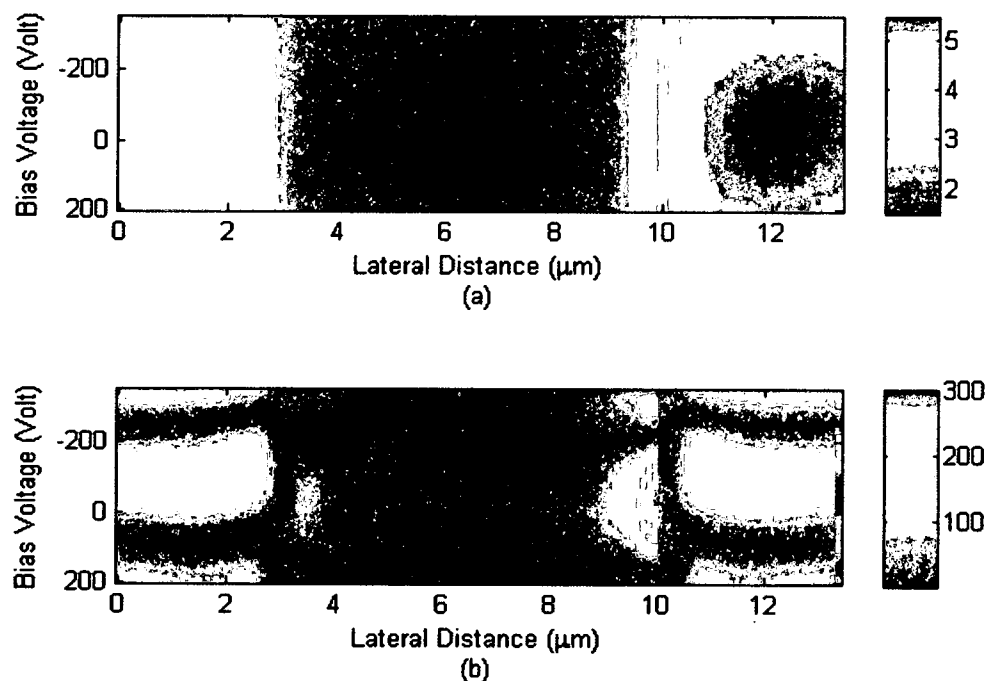


Fig. 35: dc (a) and first harmonic (b) signals resulting from the first of the two 13  $\mu\text{m}$  long scans of the micro prism.

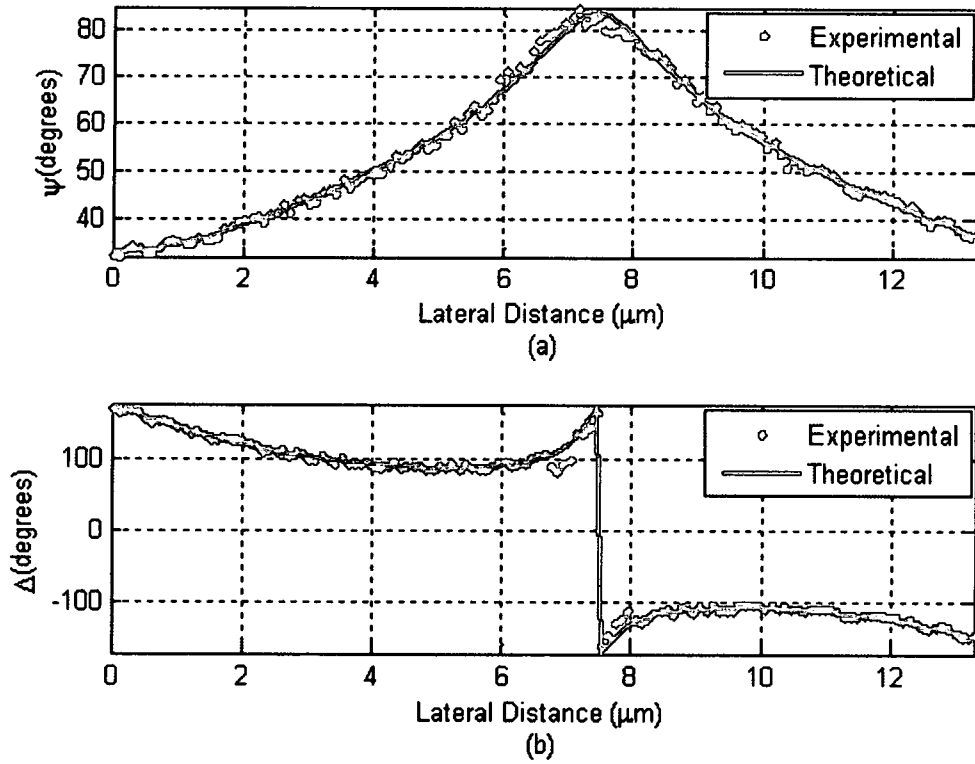


Fig. 36: Fitting of micro prism experimental data to micro prism optical model:  $\Psi$  (a) and  $\Delta$  (b).

generated and used as guesses in the model. The profile with the smallest MSE error was kept and each of the thickness data points was then individually fitted to the experimental data in order to optimize the thickness profile. Figs. 36(a) and 36(b) show the results of fitting the optical model to the measured  $\Psi$  and  $\Delta$ , respectively. There is good close agreement between the experimentally measured data and the theoretical predictions. Fig. 36(b) shows a discontinuity in the middle which, as explained earlier, is due to phase wrapping at a location where the accumulated phase is equal to  $2n\pi$ , with  $n=1, 2, 3$ , etc. In the optical model, both the thickness and the refractive index were fitting variables. Fig. 37 shows two profile measurements, corresponding to the first and second line scans, respectively. The second line scan (dashed curve) is used as a test to check for measurements repeatability. Both profile measurements are found to be in good

agreement with the AFM result. The refractive index of the micro prism was calculated and found to be 1.479. This value is slightly smaller than the one calculated earlier in the absence of the dc signal.

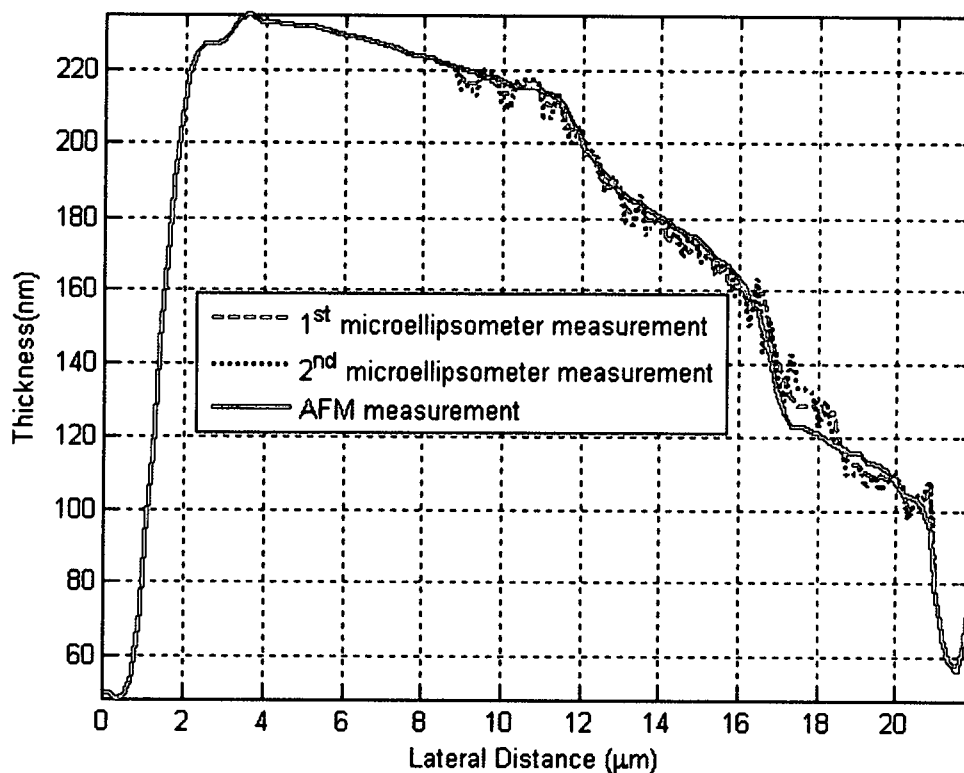


Fig. 37: Microellipsometer thickness profile measurements (dashed red and dotted black) compared to the AFM profile measurement. The second microellipsometer measurement was performed to check the repeatability of the measurements.

## B. Remarks

The characterization of the SiO<sub>2</sub> and the grating samples show that our microellipsometer is capable of taking repeatable and accurate measurements of a sample, with an acceptable associated amount of error.

In this work we only performed 1-D scanning of a surface relief pattern. This is due to the fact that currently the ellipsometric signal and the mechanical system are stable only within a limited window of time after which the system gradually slips out of focus. Because the depth of focus is very small, the polarization signal becomes greatly distorted and the spot size increases due to defocus. The mechanical stability of the translation stage also requires longer dwelling time and increased integration time for signal detection. Including an auto-focus mechanism in the system would greatly improve the stability of the signal and shorten the scanning time. In addition, the hardware control software could be optimized to speed up the data collection and processing as well. With these improvements, high spatial resolution 2D profiling of patterned surfaces with large scanning range could be achieved.

## CHAPTER VI

### CHARACTERIZATION OF ISOLATED SUBWAVELENGTH LINE STRUCTURES USING POLARIZATION AND PHASE SIGNATURES

#### A. Introduction

Polarization effects in subwavelength structures have attracted considerable research interest due to their potential application in optical metrology. Most specifically, polarizations effects have been used in the localization of sharp edges<sup>35,36</sup>, polarization-based imaging<sup>37-42</sup>, detection of isolated subwavelength line features<sup>43,44</sup>, etc. It is well known that sub-wavelength structures can modify the polarization of the probing light. When polarized light interacts with sub-wavelength structures, the main effect of interest is electric fields coupling which is responsible for different responses to the TE and TM polarizations.<sup>45-50</sup> In optical metrology, this effect can be used as a sensitive criteria in the measurement of sub-wavelength structures. This chapter consists of numerical calculations of responses to TE and TM polarizations incident on surfaces with isolated ridges whose side walls are either vertical or oblique. The optical model of the simulation consists of a linearly polarized Gaussian beam, with uniform intensity, focused on an isolated ridge using a high numerical aperture objective lens. The idea is that, at a specific wavelength, an isolated structured illuminated by the linearly polarized focused beam will generally yield a polarization signature that is specific to its width or its wall angle. This polarization signature can be sensitive enough to be used to distinguish one



line from the other with less ambiguity. Where an ambiguity exists two wavelengths can be used to resolve the degeneracy.

The focusing effect of a high numerical aperture objective lens and the interaction of the focused beam with an isolated sub-wavelength ridge are qualitatively discussed in terms of focused beam rigorous coupled wave analysis (FB-RCWA).<sup>51</sup> Using a previously developed MATLAB-based FB-RCWA code, the intensity and phase profiles are calculated, using different widths and wall angles of an isolated ridge, and compared.

## B. Focal Fields

When a linearly polarized beam is focused, the resulting focus field has components in the  $x$ -,  $y$ -, and  $z$ - axes as shown in Fig. 38. Assuming the incident field is polarized in the  $x$ -direction, there will be two induced polarizations: one along the  $y$ -axis and the other along the  $z$ -axis. Generally, the focus field polarized in the same direction as the incident field (in this case, the focus field in the  $x$ - direction) has the largest amplitude. The computation can be done following the mathematical presentations in the classical paper by Richards and Wolf.<sup>51,52</sup>

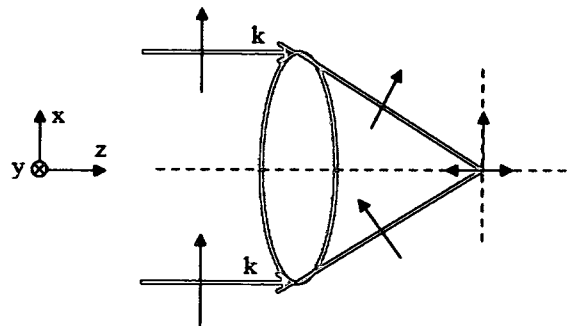


Fig. 38: Focusing of a linearly polarized beam.

The field components of the point-spread function (PSF) follow from the Debye integral for an integral field, linearly polarized in the x-direction, in the form<sup>51,52</sup>

$$\vec{E}(r, z) = E_0 \exp\left(\frac{iu}{4 \sin \vartheta_0 / 2}\right) \cdot \begin{pmatrix} -i(I_0 + I_2 \cos 2\varphi) \\ -iI_2 \sin 2\varphi \\ -2I_1 \cos \varphi \end{pmatrix}, \quad (86)$$

where  $\varphi$  is the angle of the azimuth and  $\vartheta_0$  is the angle of the full numerical aperture.

The following three auxiliary functions are used in the above expression:

$$I_0(r, z) = \int_0^{\vartheta_0} \sqrt{\cos \vartheta} \sin \vartheta (1 + \cos \vartheta) J_0(kr \sin \vartheta) \exp(ikz \cos \vartheta) d\vartheta, \quad (87)$$

$$I_1(r, z) = \int_0^{\vartheta_0} \sqrt{\cos \vartheta} \sin^2 \vartheta J_1(kr \sin \vartheta) \exp(ikz \cos \vartheta) d\vartheta, \quad (88)$$

$$I_2(r, z) = \int_0^{\vartheta_0} \sqrt{\cos \vartheta} \sin \vartheta (1 - \cos \vartheta) J_0(kr \sin \vartheta) \exp(ikz \cos \vartheta) d\vartheta, \quad (89)$$

where  $r = \sqrt{x^2 + y^2 + z^2}$ ,  $k = 2\pi / \lambda$ , and  $\lambda$  is the wavelength.

If the normalized coordinate  $u$  and  $v$  with

$$u = 4kz \sin^2 \frac{\vartheta_0}{2} = 2kz(1 - \cos \vartheta_0), v = kr \sin \vartheta_0, \quad (90)$$

are used, the integrals  $I_0, I_1$ , and  $I_2$  can be written in the scaled form

$$I_0(u, v) = \int_0^{\vartheta_0} \sqrt{\cos \vartheta} \sin \vartheta (1 + \cos \vartheta) J_0\left(\frac{v \sin \vartheta}{\sin \vartheta_0}\right) \exp\left(\frac{iu \sin^2 \vartheta / 2}{2 \sin^2 \vartheta_0 / 2}\right) d\vartheta, \quad (91)$$

$$I_1(u, v) = \int_0^{\vartheta_0} \sqrt{\cos \vartheta} \sin^2 \vartheta J_1\left(\frac{v \sin \vartheta}{\sin \vartheta_0}\right) \exp\left(\frac{iu \sin^2 \vartheta / 2}{2 \sin^2 \vartheta_0 / 2}\right) d\vartheta, \quad (92)$$

$$I_2(u, v) = \int_0^{\vartheta_0} \sqrt{\cos \vartheta} \sin \vartheta (1 - \cos \vartheta) J_2 \left( \frac{v \sin \vartheta}{\sin \vartheta_0} \right) \exp \left( \frac{i u \sin^2 \vartheta / 2}{2 \sin^2 \vartheta_0 / 2} \right) d\vartheta. \quad (93)$$

Fig. 39 (a)-(d) shows the computed intensity distributions of the components of the focal field using the equations above, for a 0.95 numerical aperture, and a wavelength of 633 nm. The dependence on the azimuthal angle  $\varphi$  generates the remarkable intensity pattern for the azimuthal and the axial field components. The intensities are normalized with respect to the total intensity (Fig. 39(d)), and the lateral distances are wavelength-normalized.

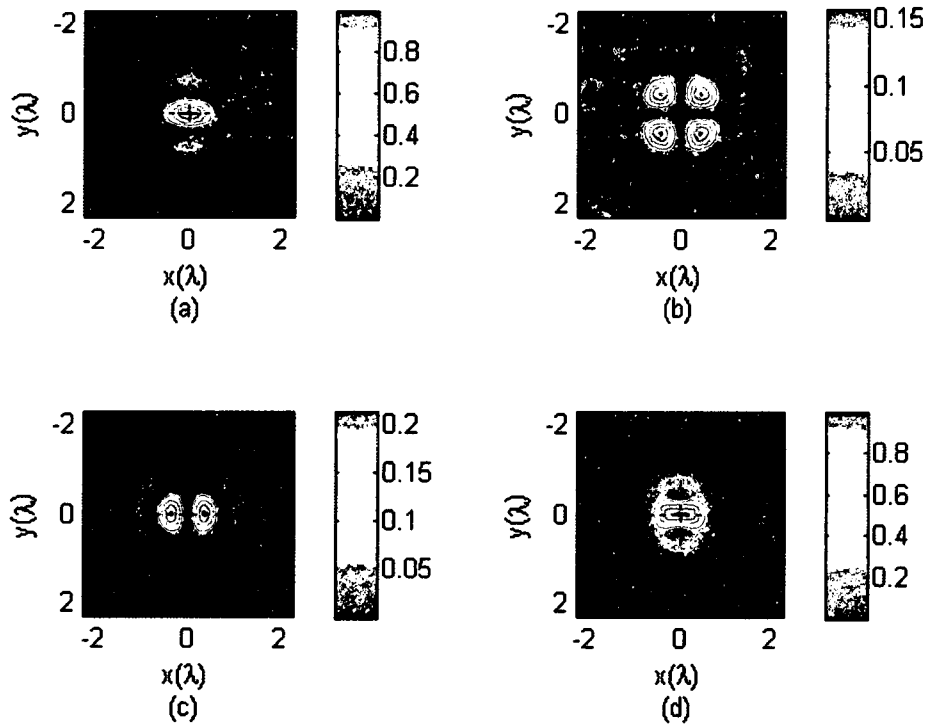


Fig. 39: Intensity distributions of field components in the focal plane: x-component (a), y-component (b), z-component (c), total intensity (d).

### C. Reflected Fields in Conical Diffraction Mounting

The problem of calculating the reflected electromagnetic field from an isolated sub-wavelength structure illuminated by a polarized focused beam, lends itself well to the conical diffraction problem. Using a binary grating in conical diffraction mounting, one can simulate an isolated line (rectangular structure) by choosing a period and a duty cycle such that the width of a ridge is a fraction of the illumination wavelength and the distance between two ridges is several wavelengths apart, say ten wavelengths.

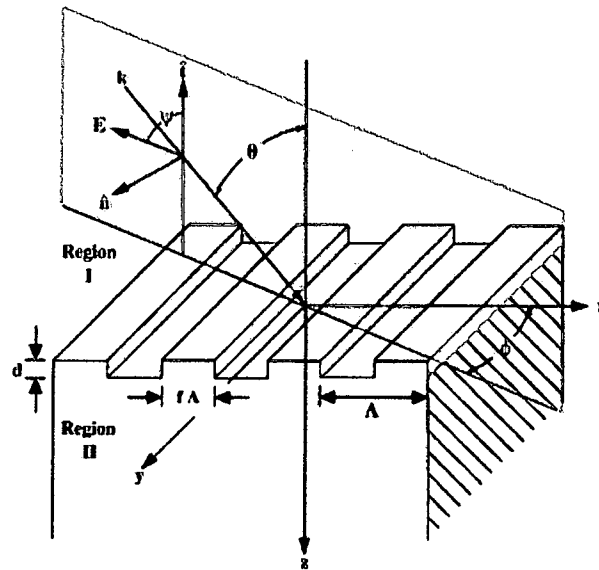


Fig. 40: Geometry for the conical diffraction mounting (figure from ref. 53).

Fig. 40 shows the conical diffraction mounting used to calculate the reflected field in the back focal plane of the objective lens. Region I in Fig. 40 is defined as the half space zone extending from  $z = 0$  to  $z = -\infty$ , with  $z = 0$  coinciding with the top of the ridges of grating. Region II is defined as the half space zone extending from  $z = 0$  to  $z = +\infty$ . The calculation of the reflected fields will be divided in two major parts. The first part, which

concerns region II, will consist of calculating the reflection coefficients of the diffracted fields using an RCWA algorithm proposed by Moharan et al.<sup>53</sup> The details for this part of the calculation are presented in ref. (16) and will not be discussed here. The second part of the calculation, which will be discussed in detail below, consists of using coordinate rotation operators to simulate the function of the objective lens as an operator that operates on both the incident and the diffracted fields.<sup>54-58</sup> This part of the calculation takes place in region I where the incident field is also defined.

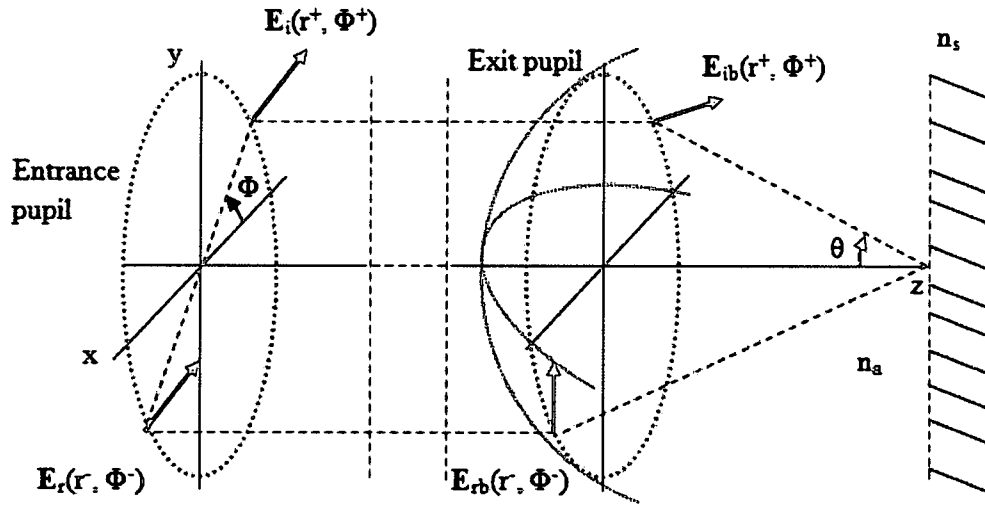


Fig. 41: Schematic of a high NA objective lens as an aplanatic system consisting of an entrance and an exit pupil. The vectors of the incident and reflected electric fields are shown.

For modeling purposes, a high numerical aperture objective lens focusing an incident field on an ideally flat sample can be represented by an aplanatic system consisting of an entrance pupil and an exit pupil, as shown in Fig. 41. In the entrance pupil a vectorial field  $E_i(r^+, \Phi^+)$ , whose position in the pupil is defined using polar coordinates, undergoes the bending effect of the lens and becomes  $E_t(r, \Phi)$ . After reflection, a field  $E_{rb}(r^+, \Phi^+)$  is obtained and undergoes the bending effect of the lens in the opposite direction and

becomes  $E_r(r, \Phi)$  in the back focal plane. The reflected field is easy to calculate since the reflection coefficients can be obtained using the well-known Fresnel Formulas. Assume that the incident field at any local position in the entrance pupil is a ray; due to Snell's law, it is easy to predict the location of a reflected ray in the exit pupil and find the total reflected field.

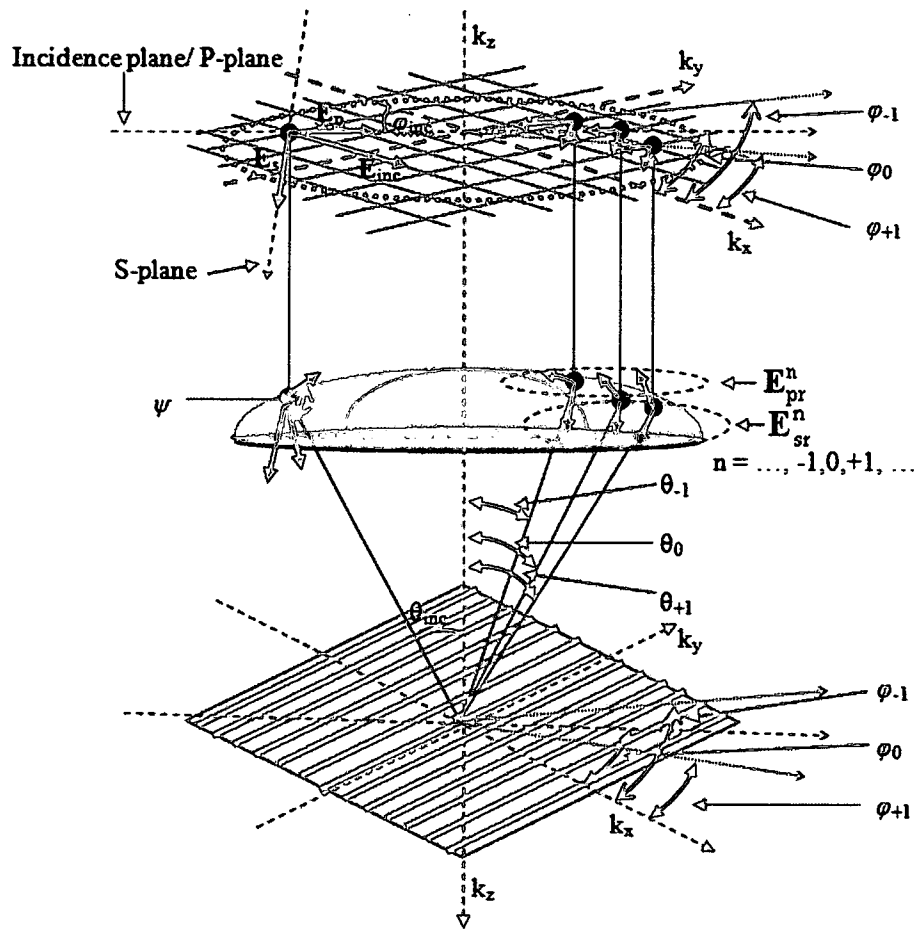


Fig. 42: k-space grid model used in the calculation of the diffracted fields in the exit pupil plane

If the sample in Fig. 41 is a grating, say a binary grating with a period equal or less than the wavelength, then, multiple diffraction orders results for each incident ray. In this case, the total reflected field results from a coherent summation of individual reflected

fields pertaining to individual diffraction orders. The summation of these fields on the  $k$ -space grid is not an easy task due to the fact that the diffracted orders associated with an incident ray do not lie in the plane of incidence, except for the 0<sup>th</sup> order. Considered together, the diffraction orders lie on the surfaces of concentric cones, hence conical diffraction.

To be able to calculate the amplitude and polarization of diffracted fields, the entrance pupil is transformed into a 2D  $k$ -space (see Fig. 42) following the method used in ref. (58). Each pair  $(k_x, k_y)$  on the grid represents the location of an incident plane wave. Assume that the entrance pupil is uniformly illuminated with plane monochromatic waves polarized in the  $x$ -direction as shown in Fig. 42. The amplitude of the incident field at each grid point  $(k_x, k_y)$  in the entrance pupil is given as

$$E^+ = (E_x^+, E_y^+, E_z^+ = 0). \quad (94)$$

The “+,-” signs indicate forward (incident) and backward (diffracted) travelling waves, respectively. It's convenient to express Eq. (94) in cylindrical coordinate system as

$$E^+ = (E_r^+, E_\varphi^+, E_z^+ = 0), \quad (95)$$

in order to take advantage of circular symmetry in the problem. The expression of the incident field in cylindrical coordinates is represented by the following rotation operation

$$\begin{bmatrix} E_r^+ \\ E_\varphi^+ \end{bmatrix} = \begin{bmatrix} \cos \varphi & \sin \varphi \\ -\sin \varphi & \cos \varphi \end{bmatrix} \begin{bmatrix} E_x^+ \\ E_y^+ \end{bmatrix}. \quad (96)$$

In this case the  $r$ -axis and  $\varphi$ -axis define the  $p$ -plane and  $s$ -plane, respectively. Therefore the field components in (96) are also the  $s$ - and  $p$ - polarizations of the incident field.

Before interacting with the sample, the s- and p- polarizations undergo the bending effect of the lens represented by  $\sqrt{k_z^+ / k}$ , where  $k = 2\pi / \lambda$  is the propagation vector of an incident plane wave and  $\lambda$  is the wavelength in the vacuum. The lens operator  $\sqrt{k_z^+ / k}$  also fulfills the sine condition and the requirement for energy conservation. Since the  $(k_x, k_y)$  is defined in advance, the incident and azimuthal angles  $\theta$  and  $\varphi$  are calculated as follows

$$\theta = \sin^{-1}(k_r / k), \quad \varphi = \tan^{-1}(k_r / k_x), \quad (97)$$

where  $k_r = \sqrt{k_x^2 + k_y^2}$ . Using  $\theta$ ,  $k_z^+ = k \cos \theta$ . The total operation for obtaining the incident s- and p- polarizations is given by

$$\begin{bmatrix} E_p^+ \\ E_s^+ \end{bmatrix} = \sqrt{\frac{k_z^+}{k}} \begin{bmatrix} \cos \varphi & \sin \varphi \\ -\sin \varphi & \cos \varphi \end{bmatrix} \begin{bmatrix} E_x^+ \\ E_y^+ \end{bmatrix}. \quad (98)$$

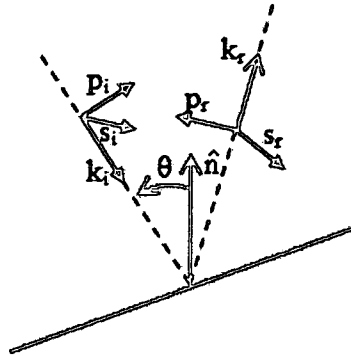


Fig. 43: Mirror symmetry between incident and reflected p-polarizations in the plane of incidence.

Now, we need to obtain the reflected s- and p-polarization after reflection on the sample. This is achieved by multiplying the incoming s- and p- polarization by the s- and p- reflection coefficients of the sample as follows,



$$\begin{bmatrix} E_{pn}^- \\ E_{sn}^- \end{bmatrix} = \sqrt{\frac{k}{k_{zn}^-}} \begin{bmatrix} -r_p & 0 \\ 0 & r_s \end{bmatrix} \begin{bmatrix} E_p^+ \\ E_s^+ \end{bmatrix}. \quad (99)$$

**Note:**

- The reflection matrix assumes no cross-polarization terms (isotropic sample).
- The minus sign in front of the  $r_p$  term guaranties mirror symmetry between the p-polarization in the incident wave and the p-polarization in the diffracted wave (see Fig. 43).
- 'n' indicates a particular reflection order of the grating which has a particular reflection angle  $\theta_n$ . This means that  $k_{zn}^- / k = \cos \theta_n$  where  $\theta_n = \cos^{-1}(k_r^n / k)$  and  $k_r^n = \sqrt{(k_x + n\Delta k_x)^2 + k_y^2}$ ; assuming the grating vector is in the  $k_x$  direction.

Assuming the ambient medium is vacuum, any diffraction order whose diffraction angle  $\theta_d$  is less or equal to  $\sin^{-1}(NA)$ , where  $NA$  is the numerical aperture of the focusing lens, is bent in the exit pupil and propagates backward. Diffracted orders whose diffraction angles do not meet the above condition are evanescent and do not contribute to the total diffracted field. The bending operation of a diffracted order is represented by  $\sqrt{k / k_{zn}^-}$ , noting that  $|k_{zn}^-| = |k_z^+|$ . Using Eq. (99), the x- and y- field amplitudes of the diffracted order are calculated as

$$\begin{bmatrix} E_{xn}^- \\ E_{yn}^- \end{bmatrix} = \sqrt{k / k_{zn}^-} \begin{bmatrix} \cos \varphi_n & -\sin \varphi_n \\ \sin \varphi_n & \cos \varphi_n \end{bmatrix} \begin{bmatrix} E_{pn}^- \\ E_{sn}^- \end{bmatrix}, \quad (100)$$

where  $\varphi_n = \tan^{-1}(k_r^n / k_x) + \pi$ .

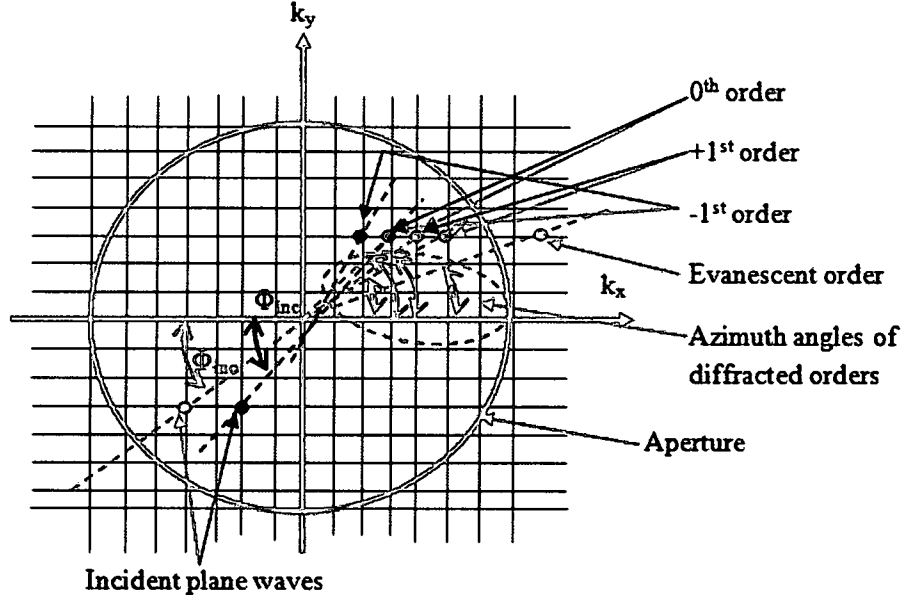


Fig. 44: Coherent addition of diffracted fields on the grid.

The condition for coherently summing the field amplitudes of two or more diffracted orders is if their wave vector components  $k_x^n = k_x + n\Delta k_x$  and  $k_y^n = k_y$  are the same, i.e. if their  $(k_x^n, k_y^n)$  map to the same coordinate point  $(k_x, k_y)$  on the grid as shown in Fig. 44.

The square grid must be generated with a step size  $\Delta k_x = 2\pi / \Lambda$  or its multiples, where  $\Lambda$  is the grating's period. This guaranties that all diffracted orders that lie inside the cone defined by the numerical aperture will fall on a coordinate point on the grid. When all the partial fields have been mapped to the grid, the intensities in the pupil are, finally, calculated for the x- and y- total field amplitudes.

#### D. Numerical Simulation Results

The first simulation consists of focusing a collimated x-polarized beam on a SiO<sub>2</sub>/Si grating. The grating parameters are as follows:

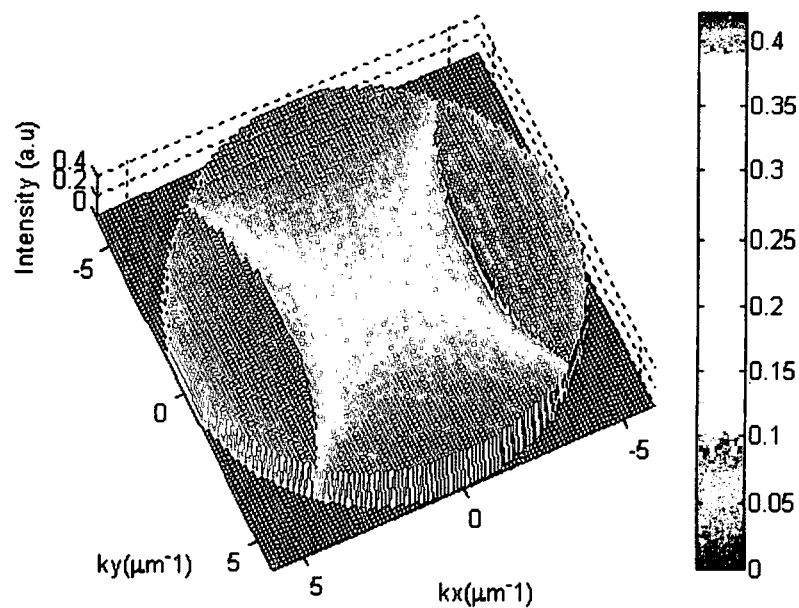
- Grating vector along the x-axis,
- Thickness: 250 nm,
- Period:  $\Lambda = \lambda/\sin(\text{NA})$ . This condition assures that only the 0<sup>th</sup> and the two 1<sup>st</sup> orders of diffraction will contribute to the total reflected field and the corresponding intensity distributions. The rest of the diffraction orders will be evanescent.
- Duty cycle: 0.5. The duty cycle is defined with respect to the grating's ridge width.

Other parameters are:

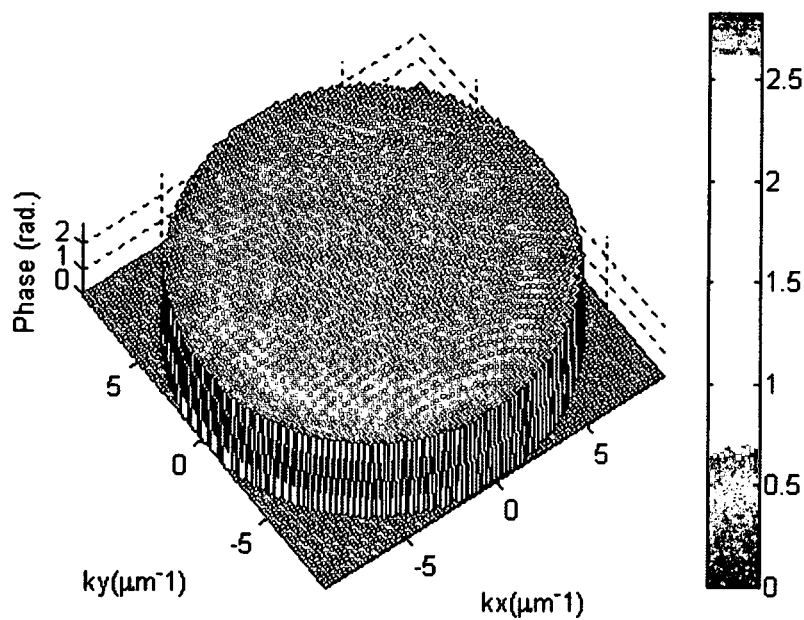
- Grid: 100 x 100 grid,
- Numerical aperture: 0.9,
- Wavelength:  $\lambda = 633$  nm.

Fig. 45 shows the intensity distribution (a) and the phase (b) calculated from the x-component of the reflected field's amplitude. The characteristic baseball pattern in the intensity is expected from the fact that the period of the grating was chosen so as to allow only the 0<sup>th</sup> and the two 1<sup>st</sup> (-1 and +1) orders to contribute to the total reflected field.<sup>55</sup> The phase is radially and circularly symmetric, and decreases toward the center. The intensity distribution in (c) and the phase in (d) were calculated from the y- component of the reflected field's amplitude. The maximum intensity in the y- component is about 1/60<sup>th</sup> the maximum intensity in the x- component. The y- component phase is not

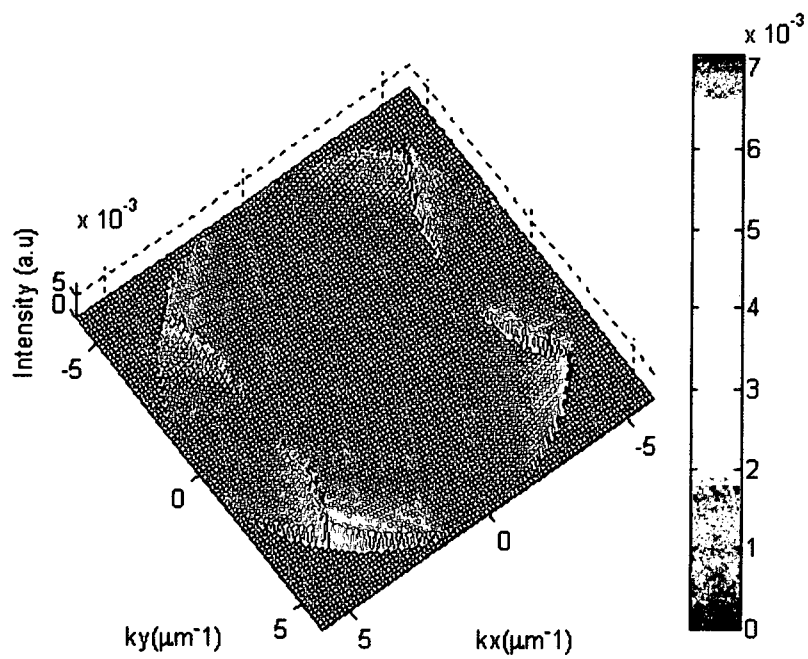
circularly symmetric, but is positive in the 2<sup>nd</sup> and 4<sup>th</sup> quadrants, and negative in the 1<sup>st</sup> and 3<sup>rd</sup> quadrants.



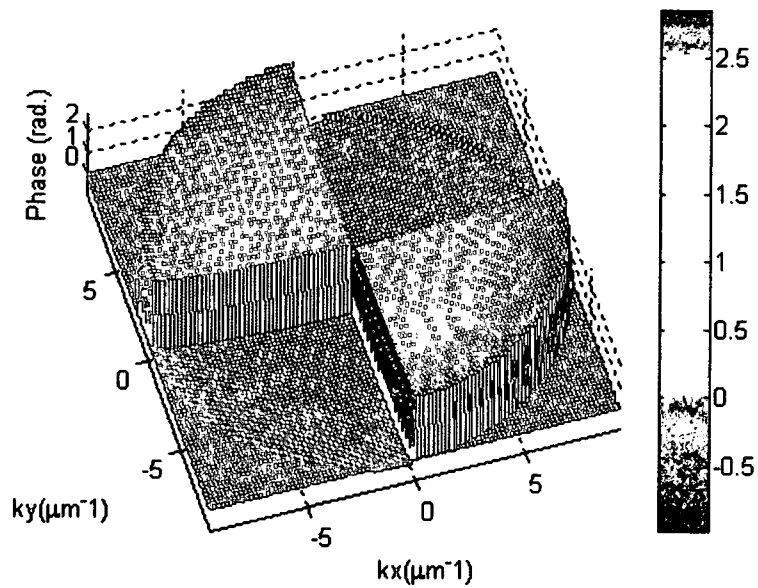
(a)



(b)



(c)



(d)

Fig. 45: Pupil plane intensity distributions (a) and (c), and phases (b) and (d) from reflected x- and y- field amplitudes, respectively.

The result in Fig. 45 shows that the computer code we developed based on the  $k$ -space grid method works correctly. We would like to study the change in intensity and phase caused by the change in width of a subwavelength line. The line is assumed to have vertical sidewalls as shown in Fig. 46. The grating's medium is again SiO<sub>2</sub> on silicon, and the thickness is 100 nm. The period is 15 wavelengths ( $15 \times .633 \text{ } \mu\text{m} = 9.49 \text{ } \mu\text{m}$ ) which is long enough to simulate an isolated line. Subwavelength linewidths, for 633 nm illumination wavelength, are chosen by using smaller duty cycles, i.e. duty cycles smaller than 0.0667 ( $= 0.633 \text{ } \mu\text{m} / 9.49 \text{ } \mu\text{m}$ ).

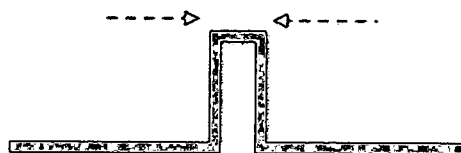
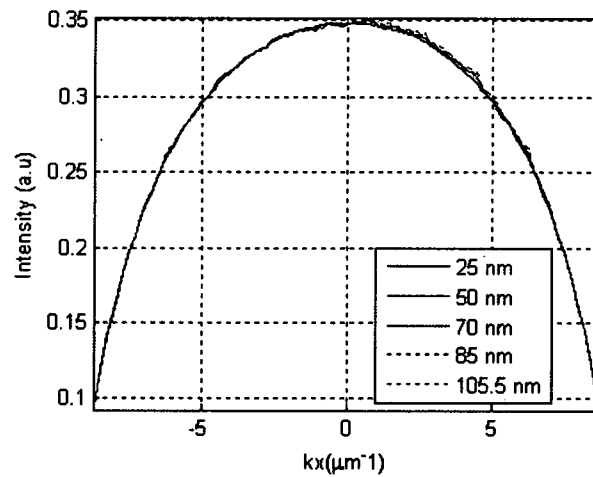


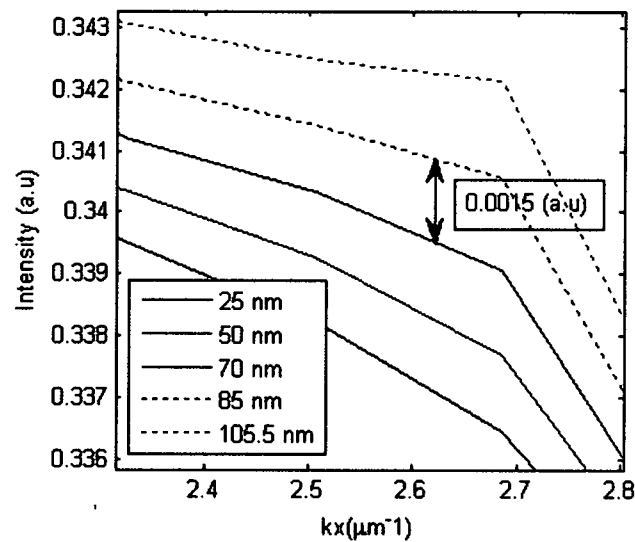
Fig. 46: An isolated ridge with vertical sidewalls.

Figs. 47(a) and 47(c) show the intensities and phases calculated for five subwavelength lines. For comparison purpose, the intensities and phases are shown along the  $x$ -axis (grating vector direction) through  $k_y = 0 \text{ } \mu\text{m}^{-1}$  in the pupil plane. From Fig. 47 (a) one can see that the  $x$ -component intensities are bunched together. Fig. 47(b) shows a zoomed view showing a 0.0015 (a.u) intensity separation between the 25 nm and the 70 nm lines. This separation is too small to be reliably detected, in addition to the inherent noise associated with intensity fluctuations. The corresponding phases shown in Fig. 47(c) are not distinguishable by eyesight, but the zoomed view in Fig. 47 (d) shows, for example, that the 50 nm and 70 nm lines are separated by 0.172 degree phase. With a phase detection resolution limit of 0.001 degree on most modern phase detection instruments, a 0.172-degree phase separation can be reliably detected. Fig. 47 (e) shows the  $y$ -

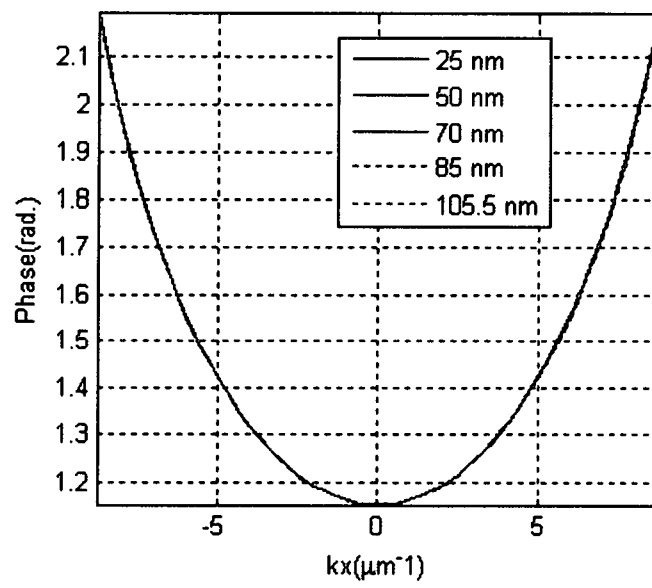
component phase of the diffracted field for different widths of the isolated subwavelength line. Fig. 47(f) shows that the phase difference between the 50 nm and 70 nm is equal to 6.6 degrees, and big enough to be reliably detected. Note that the y-component phase, although associated with a less dominant field component, is generally more sensitive to thickness changes compared to the x-component phase.



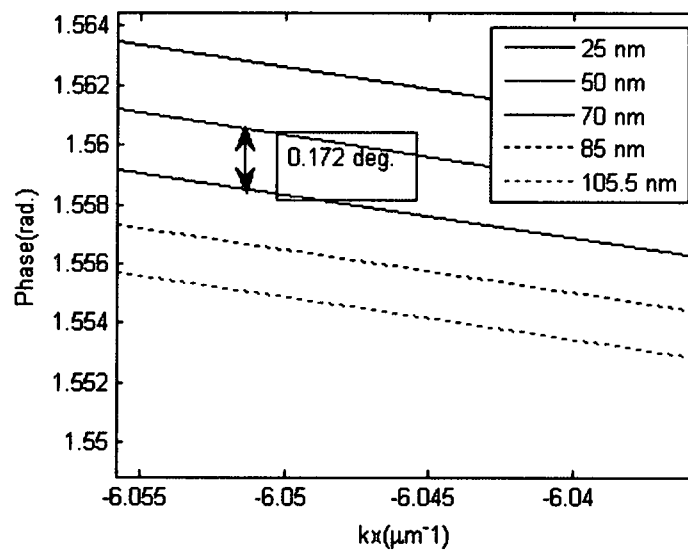
(a)



(b)

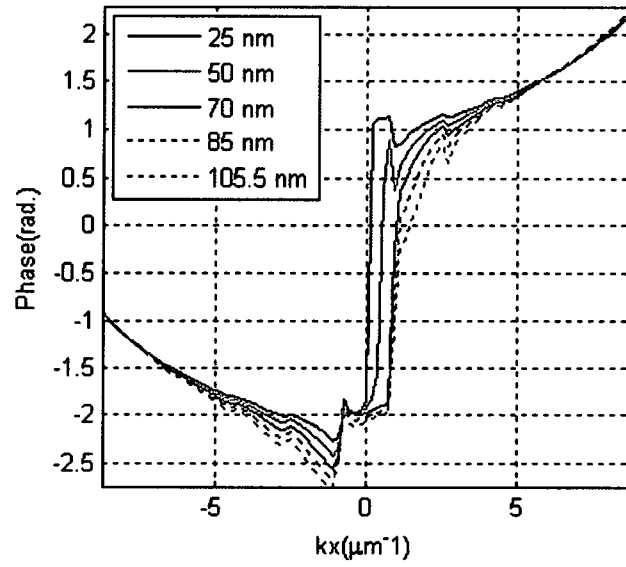


(c)

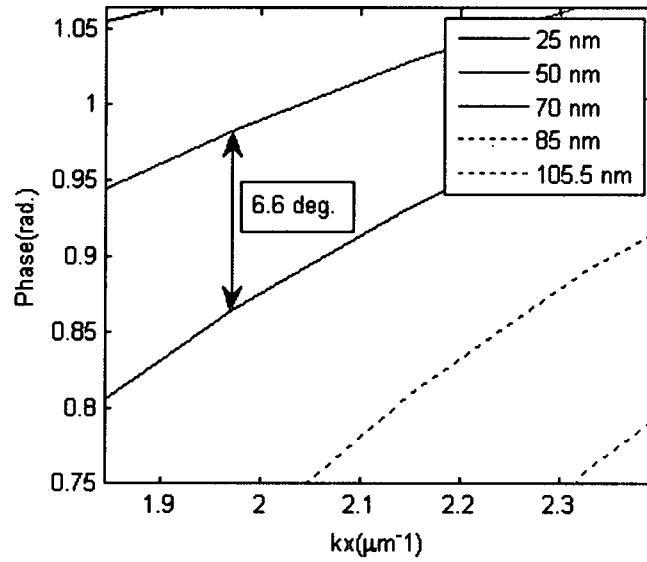


(d)





(e)



(f)

Fig. 47: Diffracted field's x- component intensities ((a) and (b)) and phases ((c) and (d)). (b) and (d) are zoomed views showing the separation of curves in (a) and (c), respectively. (e) is the phase of the diffracted field's y-component and (f) is the zoomed view of (e).

The next set of results consists of intensities and phases along the line  $k_y = 0 \mu\text{m}^{-1}$  in the pupil plane. All the parameters used in the straight side walls case above are kept the same here, except for the side wall angle. For these results, the side wall angle of the isolated subwavelength line was varied from  $-80^\circ$  to  $+60^\circ$ . For calculation purpose, it is assumed that a negative side wall angle corresponds to the shape (undercut) shown in Fig. 48(a) and a positive side wall angle corresponds to the shape shown in Fig. 48(b).

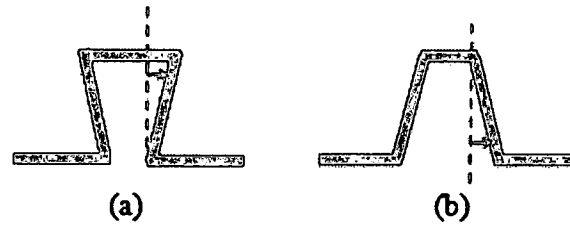
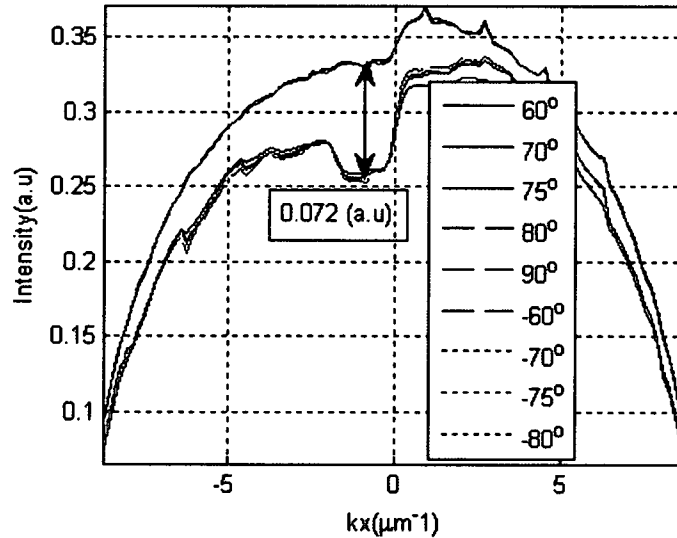
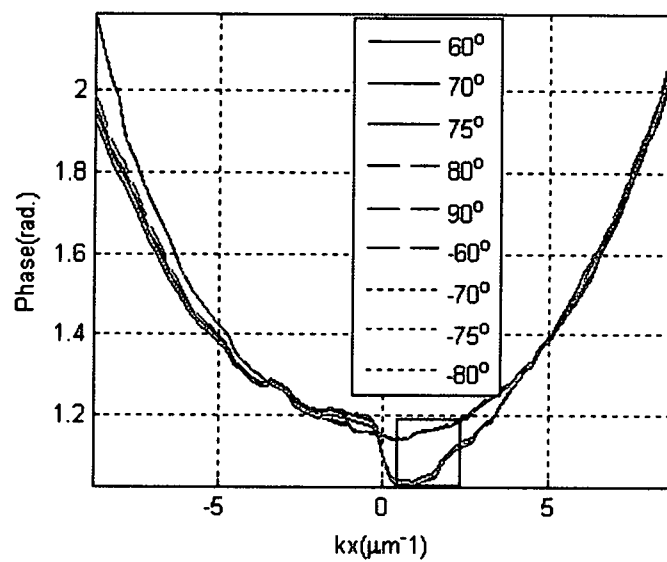


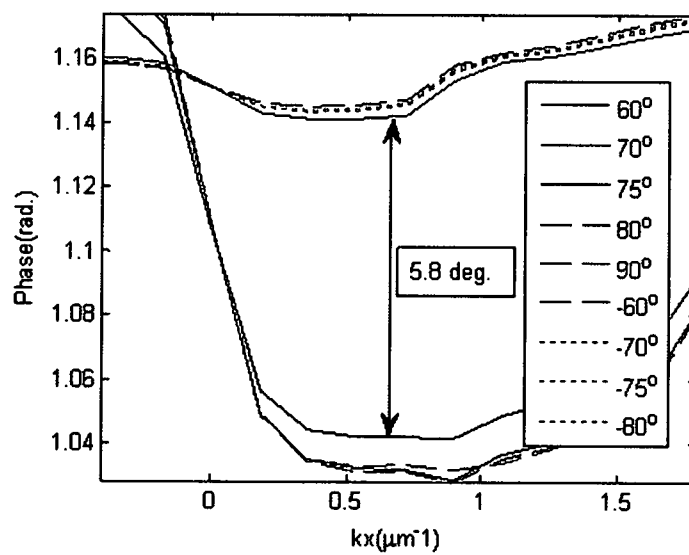
Fig. 48: An isolated subwavelength line with negative (a) and positive (b) side wall angles.



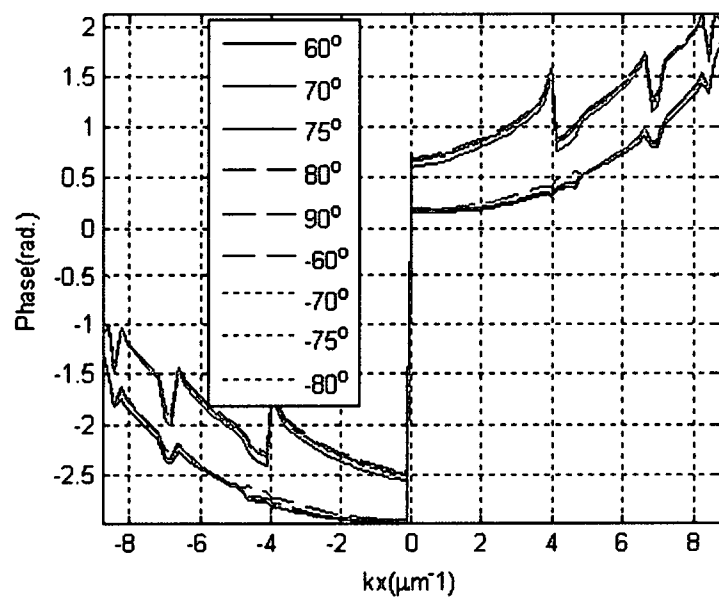
(a)



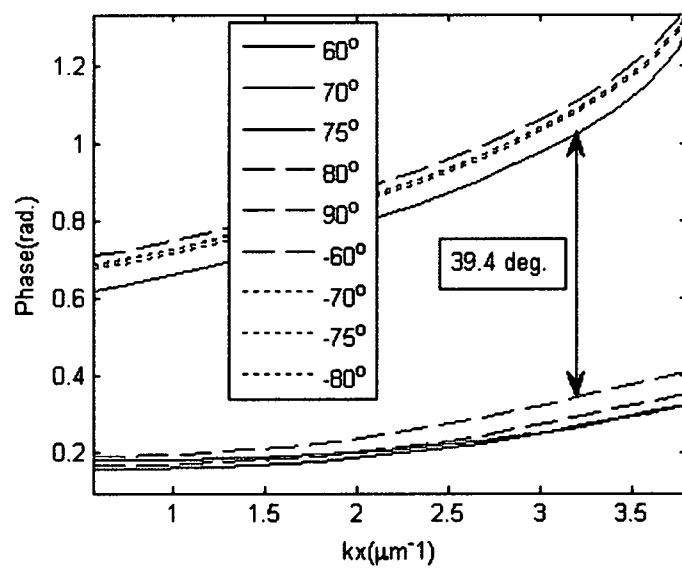
(b)



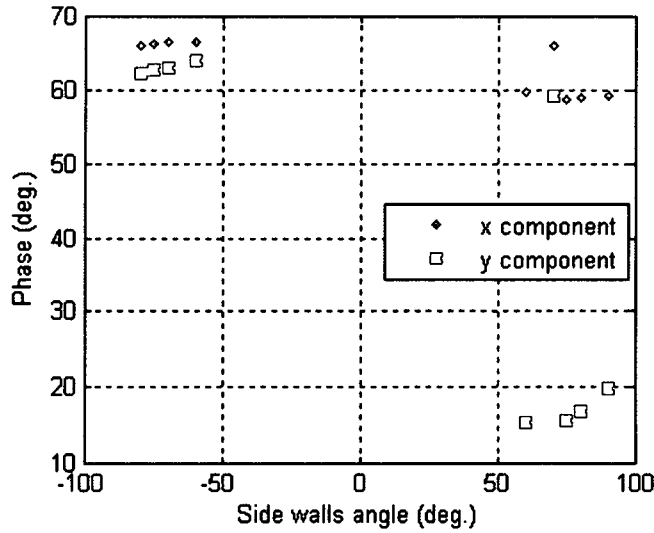
(c)



(d)



(e)



(f)

Fig. 49: x-component's intensities (a) and phases (b) for and isolated line with varying side wall angles. Fig. 49(c) shows a zoomed view of Fig. 49(b). Figs. 49(d) and 49(e) show the y-component's phases and the zoomed view, respectively. Fig. 49(f) shows a side-by-side comparison of phase change with respect to the side wall angle at the  $(k_x=3.2 \mu\text{m}^{-1}, k_y=0 \mu\text{m}^{-1})$  location in the pupil plane.

Figs. 49(a) and 49(c) show the intensities and phases of the x-component of the diffracted field calculated for 9 positions of an isolated subwavelength line's side walls angle. The intensities and phases are shown along the x-axis going through  $k_y = 0 \mu\text{m}^{-1}$  in the pupil plane. There is a growing separation of intensities and phases at the center. Except for the  $70^\circ$  slope intensity curve that is separated from other positive slope intensity and phase curves, Figs. 49(a), 49(b), and 49(c) show that all intensities and phases associated with the positive slopes are separated from those that are associated with the negative slopes. Fig. 49(c) shows that the two groups of curves are separated by minimum phase of 5.8 degrees at  $(k_x = 0.62 \mu\text{m}^{-1}, k_y = 0 \mu\text{m}^{-1})$ . This phase difference can be reliably measured and can be used to discriminate between positive- slope and negative-slope side walls of an isolated subwavelength line structure. For the y-component of the field, again except

for the  $70^\circ$  curve, all phase curves associated with positive side wall angles are generally well separated from those associated with negative side wall angles all the way along the x-axis, as shown in Fig. 49(d). At ( $k_x = 3.24 \mu\text{m}^{-1}$ ,  $k_y = 0 \mu\text{m}^{-1}$ ) the phase separation between the two groups of curves, as shown in Fig. 49(e) is calculated to be  $39.4^\circ$ , almost 7 times bigger in order of magnitude than the largest phase separation calculated earlier using the x-component field. Fig. 49(f) is a side-by-side comparison of the x- and y-phases with respect to the side wall angles. Table 2 shows the phase differences resulting from changing the angular position of sidewalls. It is seen that, for both x- and y- field component, a 5-degree change in sidewalls angle can produce a phase difference that is large enough to be reliably measured.

Side Wall Angles	Phase Difference - x-components	Phase Difference - y-components
$-80^\circ$ and $-75^\circ$	$0.15^\circ$	$0.4^\circ$
$-75^\circ$ and $-70^\circ$	$0.2^\circ$	$0.3^\circ$
$-70^\circ$ and $-60^\circ$	$0.2^\circ$	$1.1^\circ$
$-60^\circ$ and $90^\circ$	$7.3^\circ$	$44.2^\circ$
$90^\circ$ and $80^\circ$	$0.2^\circ$	$2.9^\circ$
$80^\circ$ and $75^\circ$	$0.4^\circ$	$1.4^\circ$
$75^\circ$ and $70^\circ$	$7.2^\circ$	$43.7^\circ$
$70^\circ$ and $60^\circ$	$6.1^\circ$	$43.8^\circ$

Table 2: Phase differences between consecutive phase curves shown in Figs. 49(b) and 49(d), corresponding to both x- and y- field components.

As mentioned above, the phases associated with the x- and y- components of the field show a degree of sensitivity to change in thickness and sidewall angle, compared to the field intensities. Once an appropriate phase calibration scheme is developed, our microellipsometer can be calibrated to exploit this phase sensitive for the characterization of isolated subwavelength line structures.

## CHAPTER VII

### CONCLUSIONS

The design and implementation of a high spatial resolution nulling microellipsometer based on the concept of circular polarization symmetry has been presented. At its core, the design uses the fact that a circularly polarized beam is composed of circularly symmetric rays, with respect to the optical axis. Each ray resides in an azimuthal plan in the local coordinate system and can be regarded as a channel. Each channel identically contributes to the signal by illuminating the sample with a circular polarized light, and carrying back an elliptically polarized light upon reflection on the sample. An objective lens with a NA of 0.9 is used in order to achieve high angle illumination of the sample and tight focusing of the beam to a  $0.46\text{-}\mu\text{m}$  spot size, at the wavelength of 633 nm. The small spot size allows the probing of only a small area of the sample, thus yielding highly spatially resolved microellipsometric measurements. The collaboration of all channels in the signal and the use of an annular aperture for selecting only high angle channels significantly improve the overall SNR of the microellipsometer.

A set of five samples of  $\text{SiO}_2$  thin films, deposited on Si substrates by sputtering, were measured by the microellipsometer to determine their thicknesses and indices of refraction. As compared in Figs. 31 and 32 the microellipsometer and spectroscopic



ellipsometer results are close. Although the point-to-point variation in refractive index is bigger, in Fig. 32, in the spectroscopic ellipsometer measurements than it is in the microellipsometer measurements, the values are comparable to the values presented in reference (2).

To test the thickness profiling ability of the microellipsometer, a S1813 photoresist micro prism fabricated on a silicon substrate was measured. The first set of measurements was taken and the properties of the sample were calculated based on rotation voltage data due to the unavailability of the dc signal. The thickness profile in Fig. 34(b) shows that the microellipsometer is capable of measuring a continuous change in thickness. The second set of measurements was taken after a DAQ card was added to the instrumentation in order to collect the dc signal. This made it possible to obtain the data in terms of ellipsometric angles ( $\Psi, \Delta$ ). The thickness profiles obtained from the ( $\Psi, \Delta$ ) data and compared to the AFM-measured thickness profile are shown in Fig. 37. They show that the microellipsometer is capable of taking both accurate and repeatable measurements.

In this work I only performed 1-D scanning of a surface relief pattern. This is due to the fact that currently the ellipsometric signal and the mechanical system are stable only within a limited window of time after which the system gradually slips out of focus. Because the depth of focus is very small, the polarization signal becomes greatly distorted and the spot size increases due to defocus. The mechanical stability of the translation stage also requires longer dwelling time and increased integration time for signal detection. Including an auto-focus mechanism in the system would greatly improve the stability of the signal and shorten the scanning time. In addition, the hardware control

software could be optimized to speed up the data collection and processing as well. With these improvements, high spatial resolution 2D profiling of patterned surfaces with large scanning range could be achieved.

Polarization symmetry is key to the performance of this instrument therefore the alignment of optical elements is very crucial. For example, the radial analyzer and the annular aperture are two separate optical elements that are difficult to alignment. Slight misalignment of these two elements can easily break the symmetry of the polarization and degrade the signal. In the future these two pieces may be designed as a single piece that acts both as a radial analyzer and an annular aperture, in order to simplify the alignment.

The rigorous coupled-wave analysis (RCWA) has been used to carry out the simulation of a diffracting isolated subwavelength line structure. Under high numerical aperture focusing conditions the intensities and phases of the of the diffracted fields are expected to change with varying line width or side walls angle. The results have shown that generally the field intensities are less sensitive to changes in line width and side walls angle than the phases, and that the phase associated with the y-component field is generally more sensitive than the phase associated with the x-component of the field. With a phase calibration scheme in place, the functionality of our microellipsometer can potentially be extended by exploiting the sensitivity of the x-component and y-component phases in order to measure the width and side walls angle of an isolated subwavelength line structure.

## APPENDIX

The general form of the ellipsometric signal is

$$P = K[1 + \cos 2\varepsilon \cos 2(\phi_b + \alpha_m \cos \omega t + \theta_o)] \}. \quad (A1)$$

The term  $\cos(\phi_b + \alpha_m \cos \omega t + \theta_o)$  can be expanded as a Taylor series in order to obtain the signal's harmonic components.

Given a function  $f(x)$ , its Taylor expansion around the point  $x = 0$  is

$$f(x) = f(0) + f'(0)\frac{x}{1!} + f''(0)\frac{x^2}{2!} + \dots + f^{n-1}(0)\frac{x^{n-1}}{(n-1)!} + f^n(0)\frac{x^n}{n!}. \quad (A2)$$

For the ellipsometric signal we will retain only the three first terms of the expansion, and the expansion will be carried out around  $\alpha_m \cos \omega t = 0$ .

Let

$$\begin{aligned} T &= \cos 2(\phi_b + \alpha_m \cos \omega t + \theta_o) \\ &= \cos 2(\phi_b + \theta_o) \cos(2\alpha_m \cos \omega t) - \sin 2(\phi_b + \theta_o) \sin(2\alpha_m \cos \omega t). \end{aligned} \quad (A3)$$

The first term of the expansion is

$$T_1 = T(0) = \cos 2(\phi_b + \theta_o). \quad (A4)$$

The first derivative of Eq. (A3) is

$$T' = -2 \cos 2(\phi_b + \theta_o) \sin(2\alpha_m \cos \omega t) - 2 \sin 2(\phi_b + \theta_o) \cos(2\alpha_m \cos \omega t), \quad (\text{A5})$$

and its value around zero is

$$T'(0) = -2 \sin 2(\phi_b + \theta_o). \quad (\text{A6})$$

The second term is

$$T_2 = -2 \sin 2(\phi_b + \theta_o) \frac{(\alpha_m \cos \omega t)}{1!} = -2\alpha_m \sin 2(\phi_b + \theta_o) \cos \omega t. \quad (\text{A7})$$

The second derivative of Eq. (A3) is

$$T'' = -4 \cos 2(\phi_b + \theta_o) \cos(2\alpha_m \cos \omega t) + 4 \sin 2(\phi_b + \theta_o) \sin(2\alpha_m \cos \omega t), \quad (\text{A8})$$

and its value around zero is

$$T''(0) = -4 \cos 2(\phi_b + \theta_o). \quad (\text{A9})$$

Using the second derivative the third term of the expansion is

$$\begin{aligned} T_3 &= -4 \cos 2(\phi_b + \theta_o) \frac{(\alpha_m \cos \omega t)^2}{2!} = -2\alpha_m^2 \cos 2(\phi_b + \theta_o) \cos^2 \omega t \\ &= -2\alpha_m^2 \cos 2(\phi_b + \theta_o) \frac{(1 + \cos 2\omega t)}{2} = -\alpha_m^2 \cos 2(\phi_b + \theta_o) (1 + \cos 2\omega t). \end{aligned} \quad (\text{A10})$$

Summing all three expansions terms yields,

$$\begin{aligned} T &= \cos(\phi_b + \alpha_m \cos \omega t + \theta_o) \cong \cos 2(\phi_b + \theta_o) - 2\alpha_m \sin 2(\phi_b + \theta_o) \cos \omega t \\ &\quad - \alpha_m^2 \cos 2(\phi_b + \theta_o) (1 + \cos 2\omega t). \end{aligned} \quad (\text{A11})$$

Substituting Eq. (A11) into Eq. (A1) yields,

$$P = K \{1 + \cos 2\varepsilon [\cos 2(\phi_b + \theta_o) - 2\alpha_m \sin 2(\phi_b + \theta_o) \cos \omega t - \alpha_m^2 \cos 2(\phi_b + \theta_o)(1 + \cos 2\omega t)]\}. \quad (\text{A12})$$

Regrouping the terms in Eq. (A12) by order of frequency yields the following harmonic components of the ellipsometric signal:

$$P(0) = K[1 + \cos 2\varepsilon(1 - \alpha_m^2) \cos 2(\phi_b + \theta_o)], \quad (\text{A13})$$

$$\begin{aligned} P(\omega) &= -2K\alpha_m \cos 2\varepsilon \sin 2(\phi_b + \theta_o) \cos \omega t \\ &= 2K\alpha_m \cos 2\varepsilon \sin 2(\phi_b + \theta_o) \cos(\omega t + \pi), \end{aligned} \quad (\text{A14})$$

$$\begin{aligned} P(2\omega) &= -K\alpha_m^2 \cos 2\varepsilon \cos 2(\phi_b + \theta_o) \cos 2\omega t \\ &= K\alpha_m^2 \cos 2\varepsilon \cos 2(\phi_b + \theta_o) \cos(2\omega t + \pi). \end{aligned} \quad (\text{A15})$$

## BIBLIOGRAPHY

1. Wolf and Born, *Principles of Optics: Electromagnetic Theory of Propagation, Interference, and Diffraction of Light*, 6<sup>th</sup> ed. (Pergamon, 1980). Chapter 1.
2. H. G. Tompkins, *A User's Guide to Ellipsometry*. (Academic Press, 1993) Chapters 3.
3. J. Humlicek, "Polarized Light and Ellipsometry" in *Handbook of Ellipsometry*. Thomas Harland and Eugene A. Irene, eds. (Springer, 2005). Chapter 1.
4. D. Goldstein, *Polarized Light*, 2<sup>nd</sup> ed. (Marcel Dekker, Inc., 2003). Chapter 3.
5. R.M.A. Azzam and N.M. Bashara, *Ellipsometry and Polarized Light*. North Holland, Amsterdam. Chapter 1 (1977).
6. G. E. Jellison Jr., "Data Analysis in Spectroscopic Ellipsometry" in *Handbook of Ellipsometry*. Thomas Harland and Eugene A. Irene, eds. (Springer, 2005). Chapter 3.
7. W. H. Press, B. P. Flannery, S. A. Teukolsky, and W. T. Vetterling, "Modeling of Data," in *Numerical Recipes in C: The Art of of Scientific Computing* (Cambridge University Press, New York, 1988), pp. 517 – 564.
8. G. Cormier and R. Bourdeau, "Genetic algorithm for ellipsometric data inversion," *J. Opt. Soc. Am. A* **17**, pp. 129 – 134 (2000).

9. T. Easwarakhanthan, C. Michel, and S. Ravelet, "Numerical method for ellipsometric determination of optical constants and thickness of thin films with microcomputers," *Surf. Sci.* **197**, 339 – 345 (1988).
10. F. K. Urban, "Ellipsometry algorithm for absorbing films," *Appl. Opt.* **32**, 2339 – 2344 (1993).
11. J. P. Drolet, S. C. Russev, M. I. Boyanov, and R. Leblanc, "Polynomial inversion of the single transparent layer problem in ellipsometry," *J. Opt. Soc. Am. A* **11**, 3284 – 3291 (1994).
12. S. Bosch, F. Monzonis, and E. Masetti, "Ellipsometric methods for absorbing layers: a modified downhill simplex algorithm," *Thin. Solid Films* **289**, 54 – 58 (1996).
13. D. E. Goldberg, *Genetic algorithms in search, optimization, and machine learning* (Addison-Wesley, Reading, Mass., 1989).
14. Ref. (2), chapter 1.
15. S. C. Russev and T. Arguirov, "Rotating analyzer – fixed analyzer ellipsometer based on null type ellipsometer", *Rev. Sci. Instrum.* **70**, pp. 3077 - 3082 (1999).
16. J. Monin and G. A. Boutry, " Conception, Realisation, et Fonctionnement d'un Nouvel Ellipsometre," *Nouv. Rev. Optique* **4**, pp. 159 – 169 (1973).
17. H. G. Tompkins and W. A. McGahan, *Spectroscopic Ellipsometry and Reflectometry: A User's Guide* (Wiley, New York, 1999).

18. D. Pristinski, V. Kozlovskaya, and S. A. Sukhishvili, "Determination of film thickness and refractive index in one measurement of phase-modulated ellipsometry," *J. Opt. Soc. A*, **23**, 2639 – 2644 (2006).
19. A. Mendoza-Galván, K. Järrendahl, H. Arwin, Y. Huang, L. Chen, and K. Chen, "Spectroscopic ellipsometry analysis of silicon nanotips obtained by electron cyclotron resonance plasma etching," *Appl. Opt.* **48**, 4996 – 5004 (2009).
20. G. Georges, L. Arnaud, L. Siozade, N. Le Neindre, F. Chazallet, M. Zerrad, C. Deumié, and C. Amra, "From angle-resolved ellipsometry of light scattering to imaging in random media," *Appl. Opt.*, **47**, 257 – 265 (2008).
21. Y. A. Zaghloul and A. R. M. Zaghloul, "Single-angle-of-incidence ellipsometry," *Appl. Opt.*, **47**, 4579 – 4588 (2008).
22. T. E. Jenkins, "Multiple-angle-of-incidence ellipsometry," *J. Phys. D: Appl. Phys.*, **32**, R45 – R56 (1999).
23. P. Chindaudom and K. Vedam, *Optical Characterization of Real Films and Surfaces*, K. Vedam, ed. (Academic, 1994), pp. 91.
24. F. Linke and R. Merkle, "Quantitative ellipsometry microscopy at the silicon-air interface," *Rev. Sci. Instrum.* **76**, 063701-01 – 063701-10 (2005).
25. M. Erman and J. B. Theeten, "Spatially resolved ellipsometry," *J. Appl. Phys.* **60**, 859 – 873 (1986).
26. A. Liu, P. C. Wagner, Jr., and J. L. Plawsky, "Image scanning ellipsometry for measuring nonuniform film thickness profiles," *Appl. Opt.* **33**, 1223 – 1229 (1994).
27. J. M. Leng, J. Chen, J. Fanton, M. Senko, K. Ritz, and J. Opsal, "Characterization of titanium nitride (TiN) films on various substrate using spectrophotometry, beam



- profile reflectometry, beam profile ellipsometry and spectroscopic beam profile ellipsometry,” *Thin Solid Films* **313** – **314**, 308 – 313 (1998).
28. K. Rabinovich, G. Toker, and A. Brunfeld, “Fast scanning ellipsometer for real-time inspection and characterization of surfaces,” *OSA/OIC* (2001).
  29. S. Ye, Y. K. Kwak, S. H. Cho, Y. J. Cho, and W. Chegal, “Development of a focused-beam ellipsometer based on a new principle,” in *Frontiers of Characterization and Metrology for Nanoelectronics*, D. G. Seiler, A. C. Diebold, R. McDonald, C. M. Gamer, D. Herr, R. P. Khosla, and E. M. Secula, ed. (AIP, 2007), pp. 69 – 73.
  30. C. W. See, M. G. Somekh, and R. D. Holmes, “Scanning optical microellipsometry for pure surface profiling,” *Appl. Opt.* **35**, 6663 – 6668 (1998).
  31. W. Singer, M. Totzeck, H. Gross, “Vector Diffraction,” in *Handbook of Optical Systems*, Vol. 2, H. Gross, ed. (Wiley-VHC, 2005), chapter 27.
  32. T. W. Ng, A. Tay, Y. Wang, “Spot focus size effect in spectroscopic ellipsometry of thin films,” *Opt. Comm.* **282**, 172 – 176 (2009).
  33. Q. Zhan and J. R. Leger, “Microellipsometer with radial symmetry,” *Appl. Opt.* **41**, pp. 4630 – 4637, (2000).
  34. Q. Zhan and J. R. Leger, “Interferometric measurement of Berry’s phase in space-variant polarization manipulations,” *Opt. Comm.* **213**, 241 – 245 (2002).
  35. M. Totzeck, H. Jacobsen, and H. J. Tiziani, “Edge localization of sub-wavelength structures using polarization interferometry and extreme-value criteria,” *Appl. Opt.* **39**, 6295 – 6305 (2000).

36. M. Totzeck, H. Jacobsen, and H. J. Tiziani, "Usage of polarization for high-accuracy micro-metrology sensors," preprint: *SPIE* 3897, 1999.
37. M. Totzeck and H. J. Tiziani, "Interference-microscopy of sub-wavelength structures: A rigorous computation method and measurements," *Opt. Comm.* **136**, 61 – 74 (1997).
38. M. Totzeck, "Numerical simulation of high numerical aperture quantitative polarization microscopy and corresponding near-fields," *Optik* **112**, 399 – 406 (2001).
39. W. Urbanczyk, "Optical imaging in polarized light," *Optik* **63**, 25 – 35 (1982).
40. W. Urbanczyk, "Optical imaging systems changing the state of light polarization," *Optik* **66**, 301 – 309 (1984).
41. R. A. Chipman, "Polarization analysis of optical systems," *Opt Eng* **28**, 90 – 98 (1989).
42. S. Stallinga, "Axial birefringence in high numerical aperture optical systems and the light distribution close to focus," *J. Opt. Soc. Am. A* **18**, 2846 – 2858 (2001).
43. Q. Zhan and J. R. Leger, "Measuring unresolved surface features using imaging ellipsometric polarization signatures," OSA/DOMO (2002).
44. Q. Zhan and J. R. Leger, "High-resolution imaging ellipsometer," *Appl. Opt.* **41**, 4443 – 4450 (2002).
45. Wei-Chih Liu, M. W. Kowarz, "Vector diffraction from subwavelength optical disk structures: two dimensional modeling of near-field profiles, far-field intensities, and detector signal for a DVD", *Appl. Opt.* **38**, pp. 3787-3797, (1999).
46. R. Petit et al.: *Electromagnetic Theory of Gratings*, ed. R. Petit (Springer-Verlag, 1980).

47. X. Wang, J. Mason, M. Latta, T. Strand, D. Marx and D. Psaltis, "Measuring and modeling optical diffraction from subwavelength features", *J. Opt. Soc. Am. A*, **18**, pp. 565 - 572, (2001).
48. B. K. Minhas, S. A. Coulombe, S. S. H. Naqvi and J. R. McNeil, "Ellipsometric scatterometry for the metrology of sub-0.1- $\mu\text{m}$ -linewidth structures", *Appl. Opt.* **37**, pp. 5112 - 5115, (1998).
49. S.Y. Chou, Wenyong Deng, "Subwavelength amorphous silicon transmission gratings and applications in polarizers and waveplates," *Appl. Phys. Lett.* **67**, pp. 742 - 744, (1995).
50. G. P. Nordin, P. C. Deguzman, "Broadband form birefringent quarter-wave plate for the mid-infrared wavelength region", *Optics Express* **5**, pp. 163 - 168, (1999).
51. E. Wolf, "Electromagnetic diffraction in optical systems: I. An integral representation of the image field," *Proc. R. Soc. London Ser. A*, **253**, 349 – 357 (1959).
52. B. Richards, and E. Wolf, "Electromagnetic diffraction in optical systems: Structure of the image field in an aplanatic system," *R. Soc. London Ser. A*, **253**, 358 – 379 (1959).
53. M. G. Moharan, E. B. Grann, D. A. Pommet, and T. K. Gaylor, "Formulation for stable and efficient implementation of the rigorous coupled-wave analysis of binary gratings," *J. Opt. Soc. AM. A*, **12**, 1068 – 1076 (1995).
54. F. Zijp, J. M. A. Van Den Eerenbeemd, P. Urbach, and C. A. Verschuren, "Effects of polarization on wave front measurements and manufacturing of solid immersion lenses for near-field optical recording," *Jpn. J. Appl. Phys.*, **45**, 1341- 1347, (2006).

55. K. Otaki, H. Osawa, H. Ooki, and J. Saito, "Polarization effect on signal from optical ROM using solid immersion lens," *Jpn. J. Appl. Phys.*, **39**, 698- 706, (2000).
56. L. Liu, Z. Shi, and S. He, "Analysis of the polarization-dependent diffraction from a metallic grating by use of a three-dimensional combined vectorial method," *J. Opt. Soc. Am. A*, **21**, 1545 – 1552 (2004).
57. I. Ichimura, S. Hayashi, and G. S. Kino, "High-density optical recording using a solid immersion lens," *Appl. Opt.*, **36**, 4339 – 4348 (1997).
58. M. Totzeck, "Numerical simulation of high-NA quantitative polarization microscopy and corresponding near-field," *Optik*, **112**, 399 – 406 (2001).

R 70 20 35 75)